INVESTIGATION OF CRACK ARREST FRACTURE TOUGHNESS OF LABORATORY-MANUFACTURED POLYCRYSTALLINE ICE

by

Derek West Alcorn

A thesis submitted in partial fulfillment
of the requirements for the degree

of

Master of Science

in

Civil Engineering

MONTANA STATE UNIVERSITY
Bozeman, Montana

April 2021

©COPYRIGHT

by

Derek West Alcorn

2021

All Rights Reserved

DEDICATION

I dedicate this thesis to my parents, Beth and Wright and my big sister, Berit.

ACKNOWLEDGEMENTS

I would like acknowledge my advisors, Dr. Christopher Borstad and Dr. Ed Adams. Chris initially piqued my interest about this project and was willing to take on a graduate student with no background in snow or ice. Despite challenges with his health during my time in graduate school, he was consistently available when I needed to bounce ideas off of someone. Ed was able to pick up right where Chris left off and provided necessary feedback for each version of my thesis. He diligently read countless drafts to make sure this work would be complete on a tight schedule. I would also like to acknowledge the remainder of my committee, Dr. Kirsten Matteson and Dr. Kevin Hammonds. Kirsten and I first met via Zoom and she immediately had suggestions for me to try and work through some of the issues I was having with the lab work. Kevin provided much of the lab setup needed to actually start making the samples and his guidance there was crucial to my success. I would also like to acknowledge my unofficial 'cohort' of mechanical engineering students who quickly adopted me into their group, Charlotte, Jonmichael, Brandt, Ariel and Ryan. Somehow we all managed to stay sane with numerous game and trivia nights.

I would like to thank my partner, Chloe. She encouraged me to begin grad school in Montana (while living in New York) and supported me through each stage in the process. Having just finished her Ph.D. in 2020, her feedback and advice have helped me submit my first abstract, present at a conference and complete this thesis. Her love, friendship, and encouragement have been invaluable. Finally, I would like to thank my parents, Beth and Wright, and my sister, Berit for always supporting me during each chapter of my life.

TABLE OF CONTENTS

1. INTRODUCTION 1

2. THEORY 5

2.1 Modeling 5
2.1.1 Early models 5
2.1.2 Higher Order Models 11
2.1.3 Diagnostic vs Prognostic Modeling 11
2.1.4 Blatter-Pattyn Model 11
2.1.5 SICOPOLIS Model 12
2.1.6 Elmer Ice Sheet Model 13
2.1.7 Parallel Ice Sheet Model 13
2.1.8 Glimmer-Community Ice Sheet Model 14
2.1.9 Ice Sheet System Model 14
2.1.10 Damage Mechanics and Calving Laws 15
2.2 Fracture Mechanics 16
2.2.1 Linear Elastic Fracture Mechanics 16
2.2.2 Fracture Energy 17
2.2.3 Stress Intensity Factor 19
2.2.3.1 Fracture Modes 21
2.2.4 Fracture Toughness Testing 23
2.2.4.1 Plane Strain Assumption 23
2.2.4.2 Short-Rod Plane-Strain Fracture Toughness 24
2.2.5 Fracture Behavior 26
2.3 Strengthening Mechanisms 28
2.3.1 Grain Boundary Strengthening 29
2.3.2 Strain Hardening 30
2.3.3 Precipitation Hardening 31

3. METHODS 32

3.1 Sample Creation 32
3.2 Freezing Process 34
3.3 Sample Properties 36
3.4 Sample Preparation 39
3.5 Fracture Testing 41
3.6 Troubleshooting 44
3.6.1 Ice Quality 44
3.6.1.1 Deaeration Time 45
3.6.1.2 Mold Vacuum Time 45

TABLE OF CONTENTS – CONTINUED

3.6.1.3 Freezing Time and Temperature 46
3.6.1.4 Chevron Geometry of 90 mm Diameter Samples 47

4. RESULTS AND DISCUSSION 49

4.1 Stable and Quasi-Stable Crack Growth 51
4.1.1 Fracture Behavior 53
4.2 Comparison of Laboratory-Manufactured Ice to Meteoric Ice 55
4.2.1 Strengthening Mechanisms 57
4.2.1.1 Grain Boundary Strengthening 57
4.2.1.2 Chemical Impurities 58
4.2.1.3 Elastic Anisotropy 58
4.2.1.4 Strain Hardening 59
4.3 Crack Initiation and Crack Arrest Fracture Toughness 60
4.3.1 Dependence on Temperature and Density 63
4.3.1.1 Temperature 63
4.3.1.2 Density 63
4.4 Critical Stress Intensity Loading Rate 65
4.5 Strain Energy Density 66
4.6 Chevron Geometry 66
4.7 Sources of Error 69
4.7.1 Critical Stress Intensity Loading Rate 69
4.7.2 Ice Porosity 70
4.7.3 Test Alignment 70
4.7.4 Chevron Sharpness 70
4.8 Proposed Improvements and Applications for Future Work 71
4.8.1 Sample Creation 71
4.8.2 Test Types 72

5. CONCLUSIONS 73

REFERENCES CITED 75

APPENDICES 81

APPENDIX A : DRAWINGS FOR SAW AND TEST FIXTURES 82
APPENDIX B : INSTRUCTIONS FOR SAMPLE CREATION AND MTS ENVIRONMENTAL CHAMBER 107
B.1 Sample Creation Setup 108
B.2 Procedure for Sample Creation 108

TABLE OF CONTENTS – CONTINUED

B.3 Refilling the De-aerator 112
B.4 Operating the MTS Load Frame and Environmental Chamber 113

LIST OF TABLES

Table Page

2.1 Comparison of the approximations/parameters used by each ice sheet model. 15

3.1 Comparison of the minimum, maximum and average grain size provided by each grain size measurement method. Overall, the Lehto script calculates a larger average grain size than the average grain size calculated by the ASTM E 112-10 intercept method [3, 42, 43]. 38

3.2 Pearson's Correlation Analysis for 50 mm diameter samples..... 46

3.3 Pearson's Correlation Analysis for 90 mm diameter samples..... 46

4.1 All calculated parameters for each sample, blanks in this table represent samples that did not exhibit stable or quasi-stable crack growth and thus do not have a K_{1d} or K_{1a}. All sample numbers with a * indicate the modified chevron geometry and have been excluded from portions of the analysis..... 49

4.3 CMOD and stiffness (Slope) data for each sample that exhibited stable or quasi-stable crack growth behavior. Blanks in this table represent samples that only had one increment of crack growth prior to catastrophic failure. 54

4.4 K_{1c}, K_{1d} and K_{1a} with standard deviations for 50 and 90 mm samples at -10°C and -20°C. For samples that showed two increments of crack growth, the higher load was used when calculating K_{1d} and K_{1a}..... 58

4.5 Crack Arrest Toughness, K_{1a}, as a percentage of K_{1c} for 50 and 90 mm samples that displayed either quasi-stable or stable crack growth behavior and Coefficient of Variation for these data..... 62

4.6 Crack Initiation Toughness, K_{1d}, as a percentage of K_{1c} for 50 and 90 mm samples that displayed either quasi-stable or stable crack growth behavior and Coefficient of Variation for these data..... 62

LIST OF FIGURES

Figure Page

2.1 The top image shows a model of a rigid, perfectly plastic material as assumed by Nye, while the bottom image shows glacier flow using Glen's Flow Law where the bottom of glacier has a lower velocity than the top of the glacier [26, 55]. 7

2.2 Relationship between applied shear stress and strain rate for Glen's Law (quasi-viscous creep of ice), Newtonian fluid, and a perfectly plastic solid. Figure recreated from Nye, 1951 [55]. 9

2.3 Statics simplification used for the Shallow Ice Approximation (SIA) of a slab on a slope. 10

2.4 The generalized 'anatomy' of an ice sheet. 10

2.5 The blue line shows the crack tip stress solution from Westergaard's 1939 paper while the red line shows Irwin's 1957 approximation of the crack tip stress solution [35]. Distance from the crack tip (x or r in each equation) is shown on the x-axis and stress on the y-axis. The closer the observer is to the crack tip, the higher the stress, shown by the asymptotic behavior. 20

2.6 The three different modes of fracture in LEFM, shown with the geometry of a short-rod plane strain fracture toughness test. The area highlighted in blue shows the chevron shape where the force is applied during testing. 21

2.7 Geometry of the ice samples, defined by ASTM E1304-97 [4]. The planar feature highlighted in blue shows the area removed during sample preparation. The triangular feature, not highlighted in blue, remains at the interior of the sample. The tip of the chevron is where the stress concentration develops when the sample is loaded in tension. 25

2.8 Front, top, side and perspective views of a 50 mm diameter short-rod fracture toughness specimen per ASTM E 1304-97 showing the load line, direction of applied load and the crack tip location. The chevron that is cut into the samples is a planar feature that ensures the starting location of the crack tip. 27

LIST OF FIGURES – CONTINUED

Figure Page

2.9 A look at a hypothetical microstructure of polycrystalline ice with oriented hexagonal grains. The three types of fracture behavior seen in both brittle and ductile fracture are shown as cleavage, intergranular and transgranular fracture..... 28

3.1 The setup used to create the ice samples. The water flows from the top tank into the white bucket and then into the mold. During the freezing process, water is flowing constantly. Once the water leaves the top of the mold, it flows into a buchner flask that is tucked behind the mold. The inside temperature of the refrigerator was set to 1.0°C..... 33

3.2 A simplified flow chart for the sample creation process. 34

3.3 Photo of both the 50 and 90 mm diameter samples in the Subzero Research Laboratory at MSU. The 50 mm diameter sample has been cut to the correct width while the 90 mm diameter sample has not been cut to width..... 35

3.4 A thin section imaged under cross-polarized light. The different colors represent different c-axis orientations in the ice sample..... 36

3.5 Image from the MATLAB image processing script to remove color from the thin section images and allow for grain boundary identification, shown on the left, this script was modified from Hammonds and Baker, 2016 and 2018 [32, 33]. Shown on the right is an image from the Lehto grain size measurement script [42, 43]..... 38

3.6 SolidWorks model of the sled designed and fabricated at MSU. The sled fit into a channel on the table of the band saw and kept all the cuts aligned during sample preparation. 40

3.7 Models of the fixture used to hold the ice sample while cutting the top notch and the ice sample after the top notch has been cut. The fixture used to cut the top notch slides back and forth on the sled in order to cut out the channel shown on the right. 40

LIST OF FIGURES – CONTINUED

Figure Page

3.8 SolidWorks model of the CMOD fixture designed and fabricated at MSU. The fixture fits onto the sled and slides back and forth to cut the notch used to locate the CMOD gauge during testing. This fixture is functionally the same as the one displayed in Figure 3.7, but only allows for 4 mm of side-to-side movement. 41

3.9 SolidWorks model of the chevron fixture, sled, sled insert and ice sample. The fixture used to cut the chevron is shown in orange, the sled is shown in gray, the sled insert is shown in green and the ice sample is shown in blue. 42

3.10 Picture and model of the test setup inside the environmental chamber 43

3.11 The left figure shows how the 50 mm and 90 mm samples have identical geometric relationships for the chevron. The right figure shows the adjusted chevron area relationship in order to keep the ratio of sample width to chevron area the same between sample sizes. Due to the circular cross section of the samples, the sample width:chevron area relationship is not consistent between the two sample sizes. 48

4.1 Load vs Displacement (CMOD) for 50 mm Sample 24. The 'sawtooth' behavior is indicative of crack initiation and arrest throughout the test. K_{1a} is calculated using Equation 2.20 at both A_0 and A_1 while K_{1d} is calculated using Equation 2.20 at both F_0 and F_1. This sample showed two increments of crack growth, so two values for K_{1d} and K_{1a} are calculated. K_{1c} is calculated using the load indicated by F_1. For this sample, the maximum load also occurred during a segment of crack growth and arrest, so K_{1d} and K_{1c} are both calculated using the point F_1. The curve does not start at (0,0) because a small pre-load was applied in order to hold the sample in place. 52

4.2 The fracture surfaces are highly reflective on both Sample 31 and 33, indicative of brittle, cleavage fracture. The brown streaks seen on each sample were left by the band saw blade when cutting the chevron into the samples. 55

LIST OF FIGURES – CONTINUED

Figure Page

4.3 Cleavage type fracture imaged under cross-polarized light. 56

4.4 Data from Figure 5 of Rist et al., 2002 is on the left, data presented in this study is shown on the right [62]. The linear regression shown on the left is also displayed on the right to better show the quantitative similarities. Rist et al., 2002 defined "stable" crack growth as multiple increments of quasi-stable crack growth [61]. Solid squares in this plot represent short-rod samples that fractured with "stable" crack growth defined by Rist et al., 2002 [62]. Open squares represent short-rod samples that fractured with a single increment of crack growth prior to failure. Both the X and open circles represent unstable crack growth in short-rod and three-point bend tests, respectively. All tests from Rist et al., 2002 were performed at -20°C. 57

4.5 Failure stress of laboratory-manufactured polycrystalline ice vs grain size$^{-1/2}$ for 50 and 90 mm diameter samples at -10°C and -20°C. 59

4.6 Load vs Displacement data with K_{1a} values for a subset of 50 mm and 90 mm diameter samples tested showing stable or quasi-stable crack growth behavior. Units for K_{1c} and K_{1a} are kPa $\sqrt{m}$. This subset was chosen as the two samples in each plot are representative of the different behavior seen during testing. On the top plot, for 50 mm samples, the orange line shows one increment of crack growth (quasi-stable) while the blue line shows two increments of crack growth (stable) prior to catastrophic failure. On the bottom plot, both the black and blue lines show one increment of crack growth behavior (quasi-stable). 61

4.7 Relationship between test temperature and the critical stress intensity factor. There is an increase in K_{1c} as the test temperature drops, consistent with other studies but not displayed here [61, 62, 64]. 64

LIST OF FIGURES – CONTINUED

Figure Page

4.8 Critical stress intensity factor for laboratory-manufactured polycrystalline ice samples vs density for each sample. The linear regression shows a weak relationship between density and K_{1c}. 65

4.9 Distribution of the critical stress intensity loading rate, $\dot{K}_1^*$ for each sample. Each bin is 0.022 kPa $m^{1/2}s^{-1}$ wide. None of the 90 mm samples meet the minimum critical crack tip growth rate defined by Schulson and Duval [64]..... 67

4.10 Equation 2.6 predicts a linear relationship between Strain Energy Density (U^*) and σ_f^2 [30]. A distinct relationship between U^* and σ_f^2 with the data presented in this study is seen here. 68

A.1 SolidWorks drawing of the sled used to locate the 50 mm sample fixtures on the band saw table. 83

A.2 SolidWorks drawing of the sled insert used to locate cuts made to prepare the 50 mm samples..... 84

A.3 SolidWorks drawing of the fixture used to cut the top notch in the 50 mm samples..... 85

A.4 SolidWorks drawing of the fixture used to cut the notch to locate the CMOD in the 50 mm samples..... 86

A.5 SolidWorks drawing of the fixture used to cut the chevron in the 50 mm samples..... 87

A.6 SolidWorks drawing of the wedge plate that attaches to Drawings A.7 and A.8 to make up the test fixture used to break the 50 mm samples. 88

A.7 SolidWorks drawing of the cross plate that attaches to Drawings A.8 and A.6 to make up the test fixture used to break the 50 mm samples. 89

A.8 SolidWorks drawing of the adapter that attaches to Drawings A.6 and A.7 to make up the test fixture used to break the 50 mm samples. 90

LIST OF FIGURES – CONTINUED

Figure Page

A.9 SolidWorks drawing of the wedge assembly that attaches to the top crosshead of the MTS load frame to fracture the 50 mm samples. 91

A.10 SolidWorks drawing of the top plate that sits on top of the ice sample during fracture testing. 92

A.11 SolidWorks drawing of two of the top plates with bearings and shoulder screws. These two parts sit on top of the ice samples and engage with the components in Drawing A.9 to break the 50 mm samples. 93

A.12 SolidWorks drawing of Drawing A.9 engaging with Drawing A.11 used to fracture the 50 mm samples. 94

A.13 SolidWorks drawing of the sled used to locate the 90 mm sample fixtures on the band saw table. 95

A.14 SolidWorks drawing of the sled insert used to locate cuts made to prepare the 90 mm samples. 96

A.15 SolidWorks drawing of the fixture used to cut the top notch in the 90 mm samples. 97

A.16 SolidWorks drawing of the fixture used to cut the notch to locate the CMOD in the 90 mm samples. 98

A.17 SolidWorks drawing of the fixture used to cut the chevron in the 90 mm samples. 99

A.18 SolidWorks drawing of the wedge plate that attaches to Drawings A.19 and A.20 to make up the test fixture used to break the 90 mm samples. 100

A.19 SolidWorks drawing of the cross plate that attaches to Drawings A.18 and A.20 to make up the test fixture used to break the 90 mm samples. 101

A.20 SolidWorks drawing of the adapter that attaches to Drawings A.19 and A.18 to make up the test fixture used to break the 90 mm samples. 102

LIST OF FIGURES – CONTINUED

Figure Page

A.21 SolidWorks drawing of the wedge assembly that attaches to the top crosshead of the MTS load frame to fracture the 90 mm samples. 103

A.22 SolidWorks drawing of the top plate that sits on top of the ice sample during fracture testing. 104

A.23 SolidWorks drawing of two of the top plates with bearings and shoulder screws. These two parts sit on top of the ice samples and engage with the components in Drawing A.21 to break the 90 mm samples. 105

A.24 SolidWorks drawing of Drawing A.21 engaging with Drawing A.23 used to fracture the 90 mm samples. 106

B.1 A section view of the mold with both end caps and quick-connect fittings attached. 108

B.2 Full diagram for the setup used to make all polycrystalline ice samples. 109

B.3 Drawing of the Delrin end caps used for the sample creation process. 110

NOMENCLATURE

ϵ	Strain
σ	Stress, kPa
$\boldsymbol{\epsilon}$	Strain tensor
$\boldsymbol{\sigma}$	Stress tensor
$\dot{\epsilon}$	Strain rate, s^{-1}
$\dot{\sigma}$	Stress rate, kPa s^{-1}
η	Viscosity
ν	Poisson's Ratio
E	Modulus of Elasticity, GPa
E'	Modulus of Elasticity in Plane-Strain, GPa
Q	Activation energy
R	Universal Gas Constant
T	Temperature
n	Glen's flow law exponent
B	Ice softness constant
ρ	Density
p	Pressure
$\mathbf{v}$	Velocity vector in v direction
$\mathbf{u}$	Velocity vector in u direction
$\mathbf{g}$	Acceleration due to gravity
U	Strain energy, J
U'	Strain energy density
W	Work, J
F	Force, N
A	Area, m^2
L	Length, m
V	Volume, m^3
t	Material thickness
a	Crack length
a_1	Interatomic spacing
d	Grain diameter
k	Material Stiffness, N/mm
γ_s	Energy to break atomic bonds per unit surface area
E_{bond}	Energy to break atomic bonds
E_{total}	Total fracture energy
G_c	Griffith Critical Energy Release Rate, J m^2
σ_f	Failure stress, kPa
K	Stress Intensity Factor or Orowan Strengthening Coefficient, kPa $m^{1/2}$
K_c	Critical Stress Intensity Factor, kPa $m^{1/2}$

NOMENCLATURE – CONTINUED

K_{1c}	Critical Stress Intensity Factor for Mode 1 fracture, kPa $m^{1/2}$
K_{1a}	Crack arrest fracture toughness for Mode 1 fracture, kPa $m^{1/2}$
K_{1d}	Crack initiation fracture toughness for Mode 1 fracture, kPa $m^{1/2}$
$\dot{K}_1^*$	Critical stress intensity loading rate for K_1 fracture, kPa $m^{1/2}$ s^{-1}
Y^*	Dimensionless Stress Intensity Factor Coefficient
Y_m^*	Dimensionless Stress Intensity Factor Coeffcient in ASTM E 1304-97 = 36.25
W^*	Width of sample used to calculate K_{1c}, m
D	Diameter of sample used to calculate K_{1c}, m

ABSTRACT

Approximately 50% of ice mass loss from ice sheets is due to icebergs breaking off in a process called calving. Icebergs are created through the incremental growth of crevasses, which are large fractures in the ice. Crevasse propagation and iceberg calving predictions within ice sheet models conflict with direct observations of crevasse processes. Current ice sheet models assume that a crevasse will propagate until it reaches a depth where the stress intensity factor at the crack tip is less than that of crack initiation, however, this is likely an oversimplification as current models over estimate crevasse depth. A more robust model would also account for the crack arrest fracture toughness, a measure of how well a material can stop an already propagating crack. Here, we calculate crack arrest fracture toughness for samples of laboratory-manufactured polycrystalline ice. These samples were created using a radial freezing technique with a reproducible grain size distribution of 0.95 mm $\pm$ 0.28 mm analyzed by cross-polarized light. Specimens were notched and brought to failure via a short-rod fracture toughness test at controlled temperatures and a constant displacement rate in a commercial mechanical testing apparatus with an environmental chamber. The presented data agrees with short-rod fracture toughness data collected from ice cores at the Filchner-Ronne Ice Shelf in Antarctica, demonstrating quasi-stable crack growth behavior. Results show the crack arrest fracture toughness of laboratory-manufactured polycrystalline ice is approximately 25 - 50% of fracture toughness. Using the crack arrest fracture toughness determined in this study would further increase modeled crevasse depth, indicating more analysis is required. Future studies can incorporate these data to more accurately determine crevasse penetration depth and improve iceberg calving predictions within ice sheet models.

CHAPTER ONE

INTRODUCTION

Ice sheets are continental-scale bodies of ice that cover an entire landscape, formed by snow accumulation persistent from year to year that compresses until it becomes solid ice. Glaciers are bodies of ice that cover portions of a landscape, but are two to three orders of magnitude smaller than ice sheets [47]. Over time, ice sheets and glaciers deform under their own weight and slowly flow downhill. Glaciers and ice sheets play an important role in climate change and sea level rise on Earth as they tie up enormous amounts of fresh water in the form of ice, approximately 24,000,000 cubic kilometers of liquid water equivalent [25]. As the climate warms and the Earth transitions from a period of glacial maxima to glacial minima, bodies of ice start to melt and large chunks fracture and break off in a process known as calving. Calving events are the source of up to 50% of total ice mass loss in glaciers and ice sheets [6, 19]. Deep cracks caused by high localized stresses, called crevasses, form at the surface of the ice prior to calving. Crevasses grow incrementally over time until the crack propagates through the thickness of the glacier or ice sheet.

Crevasses are commonly observed features on glaciers that have a multifaceted impact on glacier mass balance. Crevasses are created under dynamic loading conditions with large stresses that fracture the ice transverse to the flow direction and propagate through quasi-stable crack growth [59]. At the surface of a glacier, crevasses develop into paths for meltwater to travel to the base of the glacier. Meltwater has the potential to weaken the ice, contribute to basal sliding and increase fracturing [21, 58, 63]. It has been shown that fractures propagate through the ice and cause intermittent calving of icebergs from glaciers and ice shelves [7].

In order to determine the fracture properties of the ice, crevasse tip stresses need to be known. In-situ measurements of crevasse tip stresses are difficult to obtain, so lab data are used to determine material properties of polycrystalline ice that are then used to infer crevasse properties. This study determined failure stress and plane-strain fracture toughness utilizing Linear Elastic Fracture Mechanics (LEFM) assumptions to provide insight into how crevasses grow and change within a glacier or ice sheet. Fracture toughness is the ability of a material containing a crack to resist fracture and these data can be used to better constrain calving laws used in ice sheet models. Under the umbrella of fracture mechanics, there are various material properties that govern fracture behavior such as critical stress intensity factor (K_{1c} or fracture toughness), crack initiation fracture toughness (K_{1d}) and crack arrest fracture toughness (K_{1a}). These three values are known as Stress Intensity Factors (SIF), identified by the letter K, and describe crack behavior at the onset and termination of a crack within a material. Stress intensity factors are useful when describing the stress state in a material around a crack tip.

Generally speaking, current glacier and ice sheet models only consider viscoelastic stresses within the ice and have limited crevasse propagation considerations [41]. While crevasses propagate in a matter of seconds, well within the elastic range for ice, ice sheet models describe ice sheet behavior on yearly/decadal timescales. As such, crevasse propagation is not typically considered in numerical models [41, 59]. By determining K_{1d} and K_{1a} for polycrystalline ice, elastic properties can be incorporated into large scale ice sheet models to better inform crevasse propagation estimations. The discrepancy in viscous and elastic strengths of ice needs resolving in order to increase model accuracy. Resolving this discrepancy requires coupling data with an object oriented finite element model that incorporates elastic damage mechanics, potential for future work.

Current ice sheet models utilize a continuum state variable, damage, to describe the effects of cracks on ice when determining the properties of individual fractures. Damage

mechanics describes the growth of small flaws that lead to the eventual failure of the material in question. Damage mechanics stems from Griffith's Theory of Fracture, published in 1920, where microcracks in a perfectly brittle material would eventually coalesce into catastrophic failure [30]. Borstad et al., 2012, 2013 were the first studies to apply damage mechanics to large-scale ice sheet models using remote sensing data and inverse methods [9, 11]. Previously, applications of damage mechanics in ice sheet models examined viscous deformation of ice, a slow process on timescales of years to decades. All large-scale ice sheet models already incorporate viscous deformation and thus damage mechanics models could be readily implemented [41]. While viscous deformation assumptions work well for long timescales when ice behaves as an elastic-plastic material, LEFM assumptions must be used on shorter timescales when ice behaves as a linear elastic material. Elastic damage mechanics models are capable of incorporating fracture energy, a measure of strain energy per unit area of the fracture surface.

Current large scale ice sheet models do not utilize fracture energy when calculating calving rates. Fracture energy ensures a model follows the correct LEFM assumptions governing fracture behavior at different scales, related to SIF at crack arrest [5]. Crack arrest fracture toughness is the ability of a material to stop a fast moving crack from propagating further into the material. Performing short-rod fracture experiments on polycrystalline ice with incremental crack growth yields the crack arrest fracture toughness.

The data presented herein shows that laboratory-manufactured polycrystalline ice will fracture with incremental crack growth in a short-rod plane strain fracture toughness test. While incremental crack growth is expected through this test method, it has not been observed in laboratory-manufactured polycrystalline ice prior to this work. Additionally, the data show laboratory-manufactured polycrystalline ice has a similar K_{1c} to that of glacial, or meteoric ice. The calculation of K_{1a} for polycrystalline ice had not been determined prior to this study. Shown here, the fracture mechanics of polycrystalline ice can be effectively

studied in the laboratory without incurring the costs associated with obtaining, shipping and storing large sections of meteoric ice cores.

The data collected in this investigation can be used to better inform large-scale ice sheet models that currently use K_{1c} to determine when a crevasse will stop propagating. K_{1c} describes material behavior such that a crack will not grow, not when the crack will stop. In other materials, K_{1a} is a unique fracture toughness value less than K_{1c} that characterizes crack arrest. By showing laboratory experiments producing stable and quasi-stable crack growth in the same manner that crevasses propagate, models can instead utilize K_{1a} to describe crevasse properties. Previous studies have defined "stable" crack growth as multiple increments of quasi-stable crack growth. Crack growth is considered to be quasi-stable when the material is able to arrest crack growth at least once during testing. Unstable crack growth occurs when the ice is not able to stop a crack from growing. Empirical findings from other materials suggest that the K_{1a} is between 30 - 80% of the K_{1c} [60, 70]. While using K_{1a} over K_{1c} will lead to deeper crevasse predictions, as K_{1a} is a percentage of the K_{1c}, this value is important to use for calving laws in numerical models to ensure the models are depicting material behavior accurately.

CHAPTER TWO

THEORY

2.1 Modeling

In an effort to understand glacial processes, humans began studying glaciers in the 19th century, however the first mathematical models of glaciers emerged in the 20th century [26, 39]. While early numerical models were developed to understand the equations governing glacier flow, current models try to predict the outcomes of different climate change scenarios. The first numerical models introduced concepts and techniques that are still used in current models, making simplifications to greatly reduce the computational complexity. As computational power has increased with technological innovation, so has the complexity of the glacier and ice sheet models. The current models take into account a large number of ice sheet characteristics such as stress balance, thermal balance, mass transport, iceberg calving, ice damage, sea level, and ice sheet hydrology, while the first models had a comparatively limited scope [41].

2.1.1 Early models

Prior to any numerical models, J.F. Nye [55] modeled the behavior of a large body of ice as a perfectly plastic solid using the Lévy-Mises equation of flow,

$$\frac{\dot{\epsilon_1}}{\sigma_1} = \frac{\dot{\epsilon_2}}{\sigma_2} = \frac{\dot{\epsilon_3}}{\sigma_3} \tag{2.1}$$

where $\dot{\epsilon}$ is strain rate, σ is stress and each subscript number denotes the direction the strain rate and stress are acting. The Lévy-Mises flow equation does not account for elastic strain and assumes plastic strain is the dominant deformation mechanism. Disregarding elastic strain results in a perfectly rigid model prior to yielding and perfectly plastic afterwards. A

rigid, perfectly plastic material can be idealized with a block sliding on a horizontal plane. In this idealized example, the example parameters are presented first and the model parameters are inside parentheses. Displacement (strain) of the block is zero if a force under a limit value (yield stress) is applied. In the conceptual model, force is dependent on the friction between the block and the plane. Once the limit value is reached, the block slides on the plane under a constant force. Upon the removal of the applied force, the block does not return to the initial position and the displacement (strain) is permanent. The top of Figure 2.1 shows the displacement of a slab on a horizontal surface where the deformed slab is translucent compared to the undeformed slab.

Nye also modeled ice as a Newtonian fluid; defining ice as a fluid with constant viscosity, regardless of shear rate, where shear rate is directly proportional to shear stress. A Newtonian fluid model is invalid for ice because the apparent viscosity of ice changes as the loading rate changes. Nye's assumption that ice is essentially a plastic solid is now known to be incorrect as the deformation behavior of ice does have an elastic component. Soon after Nye published his work, J.W. Glen published research still in use today to model creep in ice [26]. Glen represented the deformation as a quasi-viscous fluid in Glen's Flow law,

$$\epsilon_s = Be^{-Q/RT}\sigma^n \tag{2.2}$$

where Q as the activation energy, R is the universal gas constant, T is the absolute temperature, B is the ice softness constant and n is Glen's Flow Law exponent, typically given between 2 - 4, depending on the predominant deformation mechanism [27]. Glen's Flow Law follows an Arrhenius-type relationship, where temperature is dependent on the reaction rate. For Glen's Law, the reaction rate refers to the flow rate of the ice. In Equation 2.2 both B and n are dependent on the rheology and the temperature of the ice, where B is a flow predictor based on ice rheology. As glaciers and ice sheets flow, the crystal axes of

the grains of ice align. The aligned grains create anisotropic conditions where flow along the basal plane is enhanced. Figure 2.1 shows the difference between the Nye [55] and Glen [26] laws governing ice flow. Glen's Law is able to account for the driving stress for flow and the variation of velocity through the thickness of a glacier.

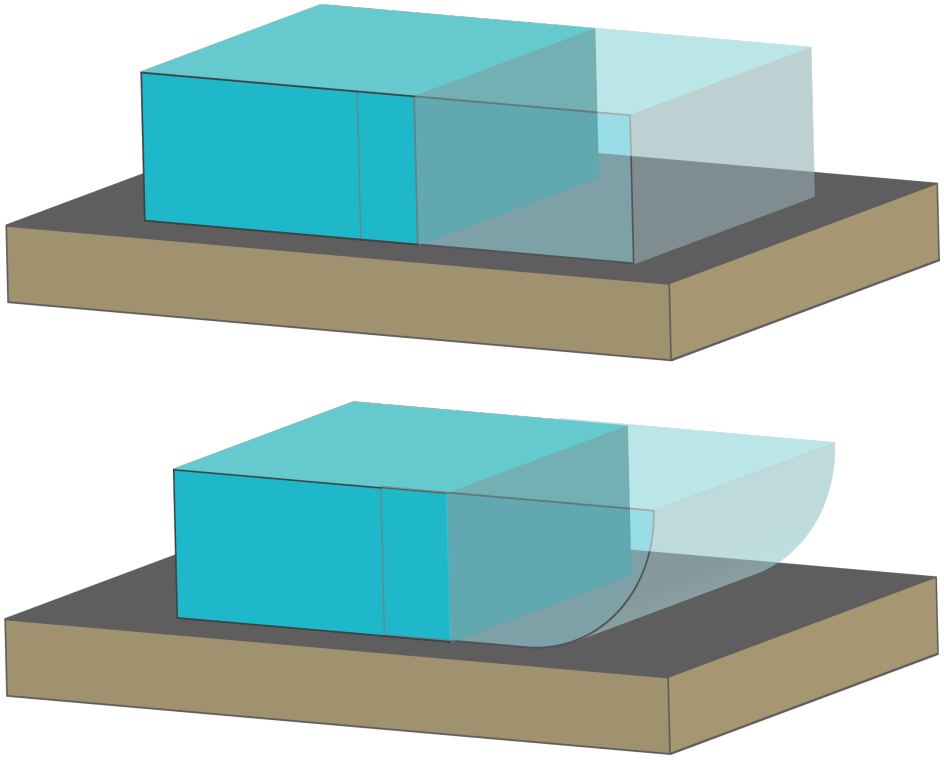


Figure 2.1: The top image shows a model of a rigid, perfectly plastic material as assumed by Nye, while the bottom image shows glacier flow using Glen's Flow Law where the bottom of glacier has a lower velocity than the top of the glacier [26, 55].

Glen's Law allows ice to be modeled as a Maxwell material, a conceptual model, with a spring and dashpot in series, where the spring represents the elastic portion of the material behavior and the dashpot represents the viscous deformation [49]. The spring and dashpot have equivalent total stress whereas the strain is a sum of the strain seen by each individual component of the model. Maxwell's model can demonstrate elastic and viscous deformations

over short and long temporal scales. Strain rate for the Maxwell model is defined by,

$$\dot{\epsilon} = \frac{\dot{\sigma}}{E} + \frac{\sigma}{\eta} \tag{2.3}$$

where $\dot{\sigma}$ is stress rate, E is the Elastic Modulus and η is the viscosity. Modeling ice deformation using the Maxwell simplification only takes into account deformation by creep, following similar behavior as creep in metals [26]. Figure 2.2 is a recreation of Figure 1 from J.F. Nye that shows ice deformation behavior assumed by three different models: 1) a Newtonian fluid with a constant viscosity (blue line); 2) a perfectly plastic material model as assumed by Nye (black line) and 3) Glen's Flow Law (red line) [26, 55]. Nye assumed that no deformation occurred at stress values below some threshold K and that shear stress did not rise appreciably above that value.

Mahaffy and Jenssen pioneered time-dependent modeling of ice sheets [37, 46]. Mahaffy and Jenssen's models utilized the concept that the horizontal boundaries of ice sheets are large compared to the thickness of the ice. By assuming the horizontal derivatives of stress, velocity and temperature are small when compared to the vertical derivatives of the same parameters, a simplification can be made, known as the Shallow-Ice Approximation (SIA) [34]. The SIA is only valid when the ice sheet or glacier is only covering land and breaks down near the edges of the body of ice. Additional assumptions made by the SIA related to the bed topography, lateral shearing, sliding mechanisms and basal melt helped ensure computational efficiency. The SIA relies on calculations of how ice flows downhill in response to the body force exerted on the mass, using formulas of a 'slab-on-a-slope' problem shown in Figure 2.3, where the only forces acting on the mass are from gravity with friction at the base opposing the motion [13].

Another 'simple' model, developed around the same time as the SIA is known as the Shallow Shelf Approximation (SSA). The SSA applies well to ice shelves, bodies of ice found

in Antarctica that are floating in the ocean but are connected to an ice stream grounded on land, shown in Figure 2.4. The SSA works best for the parts of the ice shelf that are far from the grounding line, where the ice transitions from grounded to floating, and the calving front at the terminus of the ice shelf. The SSA is also applicable to ice streams with flat bed topography and low bed strength.

The SSA is a 2D model which is vertically integrated, unlike the SIA. Utilizing the SSA in regions where velocity variations through the thickness of the glacier (at the grounding line), is difficult [18]. Both the SIA and SSA neglect the presence of temperate ice regions and only focus on polar ice using the finite-difference method as a finite element approach was not feasible over a large domain when these models were developed. The finite element method allows for finer detail in areas of interest where the element size can be easily controlled.

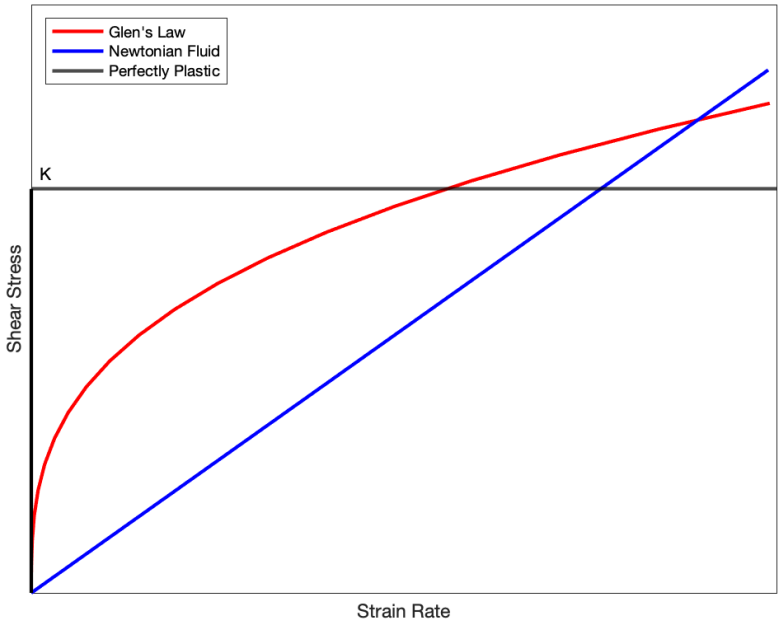


Figure 2.2: Relationship between applied shear stress and strain rate for Glen's Law (quasi-viscous creep of ice), Newtonian fluid, and a perfectly plastic solid. Figure recreated from Nye, 1951 [55].

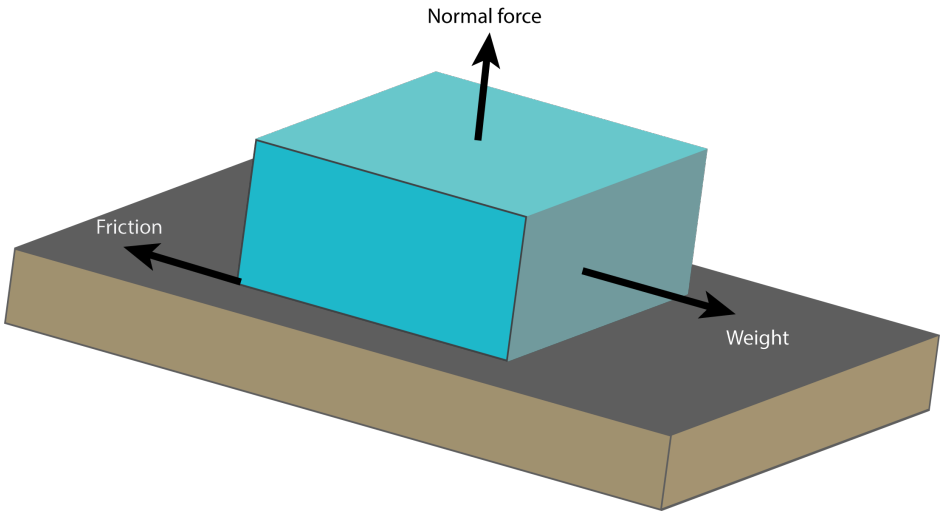


Figure 2.3: Statics simplification used for the Shallow Ice Approximation (SIA) of a slab on a slope.

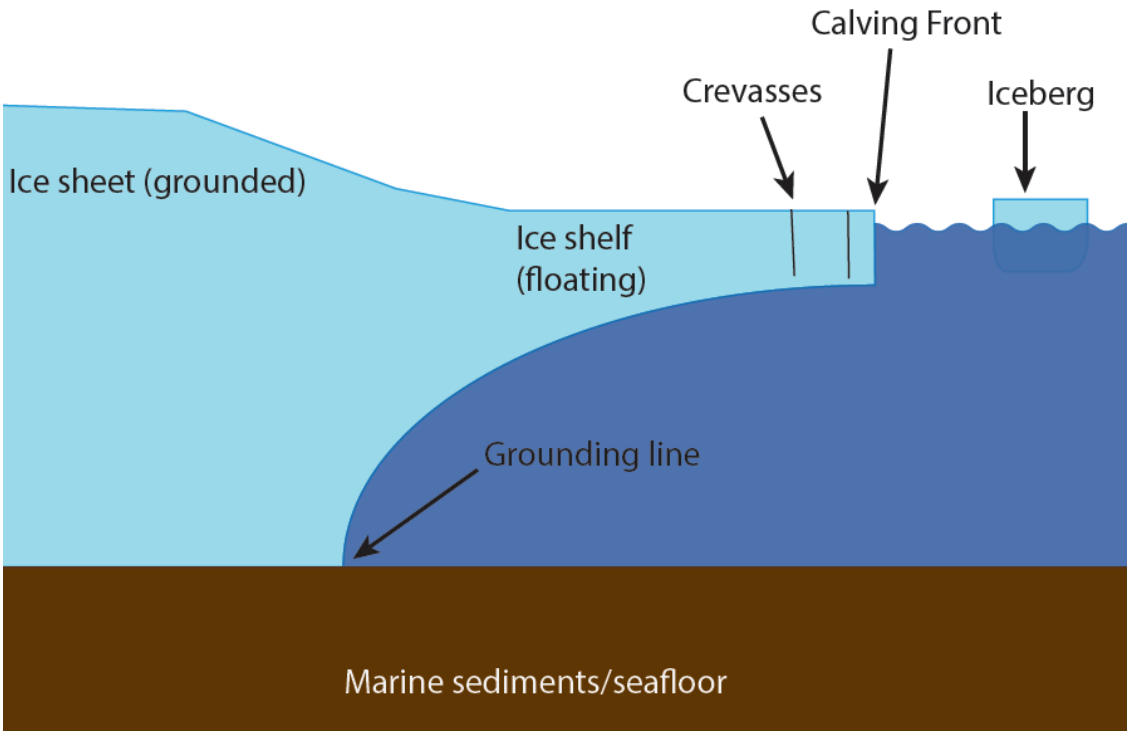


Figure 2.4: The generalized 'anatomy' of an ice sheet.

Most current models use finite element analysis as the computational power has greatly increased in recent years, allowing for more precise results in areas of interest such as the calving front and crevasse initiation near the tongue of the glacier. Additionally, the newer models account for depth-integrated viscosity and variations in ice temperature. Models that incorporate early assumptions with complex calculations are known as higher-order models.

2.1.2 Higher Order Models

Each higher order model was built with a great deal of complexity, as such, the details of each model are not covered here, just the main differences between models.

2.1.3 Diagnostic vs Prognostic Modeling

There are two distinct types of glacier models, prognostic (predictive) and diagnostic. Prognostic modeling attempts to predict the future behavior of glaciers and ice sheets to determine the impacts that additional melt will have on global climate and sea level. Prognostic modeling often involves reconstruction of past ice sheets in order to improve future predictions. Diagnostic modeling on the other hand is used to compare the accuracy of current models to observations of actual ice sheet movement. The diagnostic portion of the models provide details on how well the models are constrained and how well actual ice sheet behavior is followed. While the advancements since the 1950s improve both diagnostic and prognostic modeling, most of the work has gone into fine-tuning the diagnostic models in order to improve the accuracy of the prognostic models.

2.1.4 Blatter-Pattyn Model

In the last 25 years, many advancements have been made in modeling ice sheet dynamics and processes. In 1995, the Blatter-Pattyn model explored an efficient algorithm for calculating three-dimensional stress and velocity fields using the Navier-Stokes equations

[8]. The Stokes equations model incompressible flow, incorporating turbulence, Coriolis effect, gravity, deviatoric stress, acceleration and isotropic aspects of the fluid.

When applying Navier-Stokes to ice flow, acceleration and Coriolis forces are neglected, simplifying the equations to an equilibrium between the gravitational force exerted on the ice and the stress within the ice as,

$$\nabla \cdot \mathbf{u} = 0 \tag{2.4}$$

$$0 = -\nabla p + \nabla \cdot \boldsymbol{\tau} + \rho \mathbf{g} \tag{2.5}$$

where Equation 2.4 describes the impressibility of ice and Equation 2.5 provides the stress balance. In the above equations $\mathbf{u}$ is the velocity tensor, ρ is density, p is the pressure, $\boldsymbol{\tau}$ is deviatoric stress tensor and $\mathbf{g}$ is gravity.

The Blatter-Pattyn model utilizes additional simplifications by neglecting the horizontal gradients of the vertical velocities when compared to the vertical gradients of the horizontal velocities allowing the Blatter-Pattyn model to approximate a full Navier-Stokes model without the computational expense [8, 41]. All of the following models utilize a Navier-Stokes approach for the momentum balance of ice sheets and glaciers.

2.1.5 SICOPOLIS Model

Around the same time the Blatter-Pattyn model was developed, Ralf Greve created another three-dimensional model called Simulation Code for Polythermal Ice Sheets (SICOPOLIS) [29]. Earlier models, while three-dimensional, had very low spatial resolution due to the lack of computing power in comparison with modern computers. SICOPOLIS was developed using the finite difference method and while under constant improvement, the model was built with simple architecture. While SICOPOLIS does account for ice thickness, atmosphere temperature, water content, ice temperature and lithosphere response to ice load,

it still relies on Glen's Law to model ice rheology [28]. However, SICOPOLIS was the first to distinguish between cold ice and temperate ice. Cold ice has a constant temperature below the pressure melting point and was described by SICOPOLIS as an incompressible, viscous homogeneous fluid [28]. In SICOPOLIS, temperate ice is regarded as a two-component fluid that exists at the pressure melting point of ice and contains liquid water. By including temperate ice in SICOPOLIS, more accurate representations of cold ice sheets can be made as polar ice sheets typically have a thin layer of temperate ice that heavily influences ice deformation and flow.

2.1.6 Elmer Ice Sheet Model

Developed in Finland by the Finnish IT Center for Science in 2004, the Elmer Ice Sheet Model was the first to utilize the full three-dimensional Navier-Stokes equations. Full-Stokes (FS) models account for all nine of the stress tensor components and are useful where the simpler models break down, namely at the grounding line and at the horizontal extents of the ice sheets/glaciers. FS models are not necessary at the interior of the ice sheet given their high computational costs. The Elmer model was the first model to incorporate the SIA, SSA and FS models into the same simulation package.

2.1.7 Parallel Ice Sheet Model

Another higher-order model created after the Elmer model is called the Parallel Ice Sheet Model (PISM). The purpose of PISM is to accurately model fast ice streams at high-resolution in a time dependent, thermo-mechanically coupled model [13]. PISM applies SIA and SSA, also incorporating ice sheet geometry, ice stream locations, ice temperature and effective thickness of basal melt water to create a unified model [72]. Prior to PISM, models have not accounted for the basal melt lubricating the bed of the glacier and enhancing flow. PISM also incorporates Glen's Flow Law to model ice rheology and deformation.

2.1.8 Glimmer-Community Ice Sheet Model

Developed in 2009, the Glimmer-Community Ice Sheet Model (Glimmer-CISM or CISM) was the first model incorporated into a larger global climate model [44]. CISM is paired with the Community Earth System Model to attempt to predict global sea level rise. While all of the models previously discussed can perform predictive simulations, CISM was the first to be built with that purpose in mind. CISM also employs the SIA and FS modeling techniques discussed above using a combination of the finite element and finite difference methods. CISM does not have any calving laws built in nor does it consider ice shelves. Once the model calculates that the ice is floating, the ice thickness is set to zero [44]. While all of the models discussed thus far have the capability to perform both diagnostic and prognostic simulations, CISM was the only model created to better incorporate ice sheet behavior into a larger earth climate model.

2.1.9 Ice Sheet System Model

Finally, the most recently released ice sheet model is known as the Ice Sheet System Model (ISSM). The ISSM was developed in 2012 by the Jet Propulsion Laboratory and University of California, Irvine. Like SICOPOLIS and PISM, ISSM is a higher order model that takes advantage of the SIA and SSA when appropriate and applies a FS solution when modeling the grounding zone. The ISSM uses the finite element method with mesh refinement, parallel and iterative solvers as well as a specifically designed software architecture [41]. ISSM combines the full Stokes model, the Blatter-Pattyn model, the SSA and SIA assumptions to model ice sheets in both Greenland and Antarctica.

Table 2.1 shows a comparison of the different models discussed above and the different solution methods used.

Table 2.1: Comparison of the approximations/parameters used by each ice sheet model.

Models	**SIA**	**SSA**	**Glen's Law**	**Full Stokes**	**Finite Difference**	**Finite Element**
Blatter-Pattyn	X	-	X	X	-	X
SICOPOLIS	X	X	X	-	X	-
Elmer	X	X	X	X	-	X
PISM	X	X	X	-	-	X
CISM	X	-	X	X	X	X
ISSM	X	X	X	X	-	X

2.1.10 Damage Mechanics and Calving Laws

Since their respective releases, SICOPOLIS, Elmer, PISM and ISSM have all incorporated ice damage mechanics into their simulations. When each of model was released, none of them included complex calving laws or fracture mechanics to model the behavior of crevasse formation either on ice sheets or marine terminating glaciers. The first models to include calving laws modeled a crevasse that propagates to the depth where the stress intensity factor is equal to K_{1c} [69]. PISM later added a calving algorithm that is based on the along and across flow strain rate which correlates the calving rate and the first-order approximation of local ice flow spreading rate [22]. The PISM calving algorithm does not take into account the formation and propagation of crevasses, only large-scale behavior. LEFM and continuum damage mechanics (CDM) are currently the most common methods used to determine calving rates in ice sheet models.

A CDM method proposed by Borstad et al., 2016 describes both the formation and evolution of fractures in a fully viscous continuum damage model [10]. Continuum damage mechanics is applied to the standard momentum balance equations of creep deformation in

order to account for the rheological weakening caused by fractures [11]. In the Borstad models, damage is a state variable that accounts for the influence of the fractures on deformation visible at the surface of an ice shelf. An alternative method developed by Krug, combines LEFM and CDM, and matches observed crevasse evolution of a marine-terminating glacier in Greenland; incorporating damage occurring to the ice over long timescales, which enhances the viscous flow of ice [40]. Eventually, brittle fractures propagate down into the ice at much shorter timescales when LEFM dominates.

Despite all of the above-mentioned models using Glen's flow law for deformation as well as crevasse initiation and propagation, there are problems with the law. Glen's law is used to calculate threshold stresses for viscous ice deformation, which infers fracture initiation stresses are in the range of 100-400 kPa, but pure ice measured in laboratory fracture experiments are routinely $\sim$1 MPa [10]. Due to this discrepancy, it is necessary to utilize an additional approach to determine fracture properties of glacial ice, known as Linear Elastic Fracture Mechanics.

2.2 Fracture Mechanics

2.2.1 Linear Elastic Fracture Mechanics

Linear Elastic Fracture Mechanics, or LEFM, originally developed by A.A. Griffith in 1920, is a basic theory of fracture that applies to sharp cracks in elastic materials [20]. As described above, LEFM dominates during crevasse initiation and propagation. LEFM is applied when the material is assumed to be isotropic and linear elastic. Applying LEFM assumptions, the stress in the material can be calculated using the theory of linear elasticity [67]. The theory of linear elasticity states that if the stress on a material does not reach a certain threshold stress (yield stress), when the stress is removed, the material returns to its initial shape. If the material follows the theory of linear elasticity everywhere except an increasingly small area around the crack tip, LEFM behavior is assumed for the bulk

material [50, 67]. LEFM started with Griffith and the analysis of fracture energy, described in Section 2.2.2, but was later modified and improved by Irwin and Orowan [1, 30, 35].

2.2.2 Fracture Energy

LEFM is the basic theory of crack initiation and fracture first described by Griffith in 1920 and 1924 [50]. Griffith's 1920 paper covering an energy based analysis of material fracture provided the foundation for much of the subsequent fracture mechanics work [30]. Griffith's paper related the work necessary to break atomic bonds in a material to the strain energy released by the material during crack growth instead of focusing on the stresses at the crack tip. While Griffith's theory is only directly applicable to brittle materials, such as glass, the concepts have been applied to other materials as well [20]. Griffith used the fracture energy method to show,

$$U = \int \boldsymbol{\sigma} : d\boldsymbol{\epsilon}\, V \tag{2.6}$$

where U is the total strain energy of the body, $\boldsymbol{\sigma}$ is the stress tensor, $\boldsymbol{\epsilon}$ is the strain tensor and V is volume of the material. Finally, using the linear elastic relationship in one dimension, $\sigma = E\epsilon$, to simplify Equation 2.6 to,

$$U^* \;=\; \frac{1}{2} E\, \epsilon^2 \;=\; \frac{1}{2}\sigma\epsilon \;=\; \frac{\sigma^2}{2E} \tag{2.7}$$

where U^* is strain energy density, E is the Elastic Modulus and σ is stress. Griffith used the above formulation to determine the strain energy released during fracture. If a material is stressed, energy is built up within the body as strain energy,

$$U = \frac{\sigma^2}{2E}\, V \tag{2.8}$$

As the material fractures, all the built up energy is released and the accumulated strain energy in the material drops. In order to determine the energy balance associated with fracture, Griffith calculated the energy required to break atomic bonds within a given material,

$$E_{bond} = 2\,\gamma_s a\,t \tag{2.9}$$

where γ_s is the energy required to break atomic bonds per unit area of the crack, a is the crack length and t is material thickness. The factor of two in Equation 2.9 is required because two new surfaces are created when atomic bonds break during crack growth.

Griffith proposed that a material contained a given density of finely distributed cracks that produce a stress concentration when strained. When a cracks grows, there is an increase in surface area on either side of the crack. The crack growth requires energy to overcome the strength of atomic bonds holding the material together. Griffith defined the increase in surface energy accompanying the crack growth as the elastic strain energy, leading Griffith to conclude that a crack will propagate when the decrease in elastic strain energy is at least equal to the energy required to create the new crack surface [20, 30]. Griffith created an overall energy balance equation for a fracture event,

$$E_{\text{total}} = 2\,\gamma_s a\,t + \frac{\sigma^2}{2E}\,V - \frac{\sigma^2}{2E}\,t\,\pi\,a^2 \tag{2.10}$$

where γ_s is the energy to break atomic bonds per unit surface area, σ is the applied stress, a is crack length, E is Elastic Modulus, t is the specimen thickness and V is specimen volume. While Griffith's initial work dealt with glass, as mentioned above, the fracture energy approach initially could not account for more ductile materials; partially corrected by Irwin and Orowan, proposing the majority of the strain energy in a ductile material was not utilized to make new surfaces, but instead to plastically deform the material directly adjacent to the crack tip [1, 36]. Equation 2.10 can be simplified by differentiating with

respect to crack length, a, and setting the derivative equal to zero,

$$\sigma_f = \sqrt{\frac{G_c E}{\pi\, a}} \tag{2.11}$$

where G_c is the Critical Energy Release Rate [48]. Equation 2.11 can be used to determine approximate failure stress, σ_f, for a given crack length. G_c is the strain energy release rate where the decrease in potential energy per fracture surface area is equal to the energy required to break the atomic bonds along the fracture surface. Developed by Irwin, and modifying work from Griffith and Orowan, Equation 2.11 relates the material properties (E), flaw size (a), failure stress (σ_f), and critical strain energy release rate [1, 30, 36].

2.2.3 Stress Intensity Factor

While the energy analysis provides useful insight into fracture processes, another method has proven itself more useful in engineering practice. Originally developed by Westergaard in 1939, the stress intensity approach to fracture analysis relates stress to distance from the crack tip. Westergaard used complex numbers to represent the real and imaginary components of the stress function [71]. Westergaard developed a solution for a crack in an infinite plate in equi-biaxial tension to arrive at

$$\sigma_{xx} \;=\; \sigma_{yy} \;=\; \frac{\sigma_\infty}{\sqrt{1-\left(\frac{a}{x}\right)^2}} \tag{2.12}$$

where a is the crack length and x is the distance from the crack tip. Figure 2.5 shows a plot of Equation 2.12 with distance from the crack tip on the x-axis and stress on the y-axis. The closer the observer is to the crack tip, the higher the stress, shown by the asymptotic behavior.

In his 1957 paper, Irwin applied theory from Griffith and Westergaard to develop the method used today, the Stress Intensity Factor (SIF) [35]. SIF is determined by analyzing

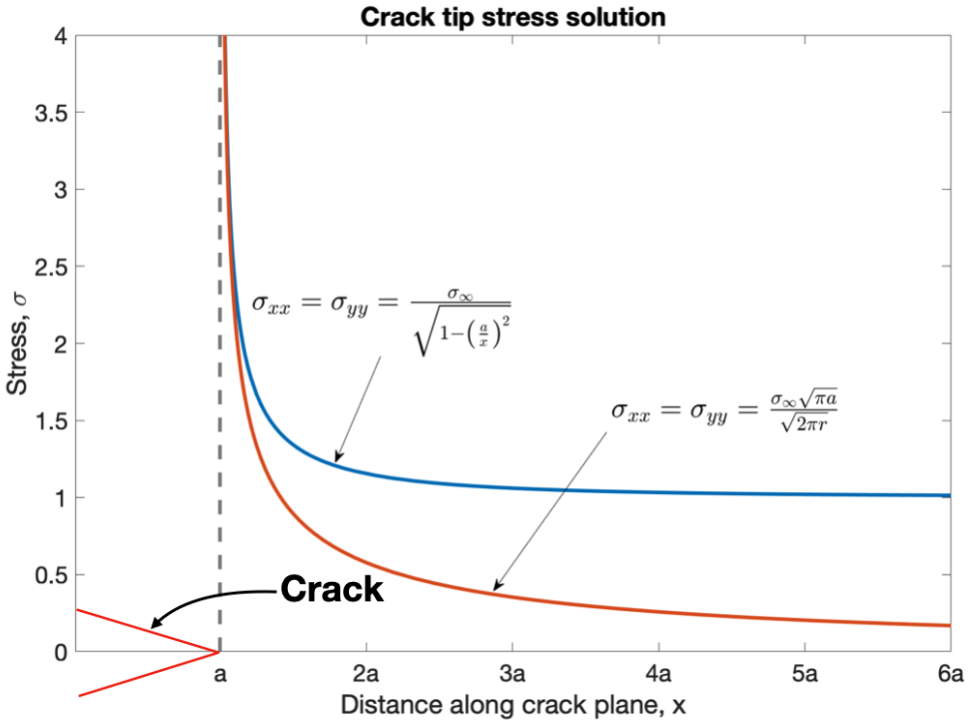


Figure 2.5: The blue line shows the crack tip stress solution from Westergaard's 1939 paper while the red line shows Irwin's 1957 approximation of the crack tip stress solution [35]. Distance from the crack tip (x or r in each equation) is shown on the x-axis and stress on the y-axis. The closer the observer is to the crack tip, the higher the stress, shown by the asymptotic behavior.

the stress field surrounding the crack tip and has units of stress $\cdot\sqrt{length}$. Irwin developed

$$\sigma_{xx} = \frac{K_I}{\sqrt{2\pi r}} \cos\frac{\theta}{2}\left(1 - \sin\frac{\theta}{2}\sin\frac{3\theta}{2}\right) + ... \tag{2.13}$$

$$\sigma_{yy} = \frac{K_I}{\sqrt{2\pi r}} \cos\frac{\theta}{2}\left(1 + \sin\frac{\theta}{2}\sin\frac{3\theta}{2}\right) + ... \tag{2.14}$$

$$\tau_{xy} = \frac{K_I}{\sqrt{2\pi r}} \cos\frac{\theta}{2}\sin\frac{\theta}{2}\cos\frac{3\theta}{2}... \tag{2.15}$$

from the Westergaard solution for the crack tip where K_I is the SIF for a Mode I crack,

described in Section 2.6. $\sqrt{2\pi r}$ shows the reliance on distance from the crack tip, r, and how stress increases asymptotically as distance from the crack tip decreases. As the distance from the crack tip decreases, the stress increases infinitely, also shown in Figure 2.5. The higher order terms of Equations 2.13, 2.14 and 2.15, indicated by ellipses, are neglected when the observer is close to the crack tip, shown by the equations in Figure 2.5.

2.2.3.1 Fracture Modes While a material can be loaded in any direction with any crack orientation, it is helpful to break the system down into components. There are three modes of fracture typically considered, shown in Figure 2.6. Crevasses primarily propagate with Mode I fracture (the focus of this study) and as such, all references to stress intensity factor will take the form of K_1. K_2 and K_3 refer to fracture modes II (shearing) and III (tearing), respectively. Just as Equations 2.13, 2.14 and 2.15 relate stress and crack geometry to K_1, similar equations exist for K_2 and K_3.

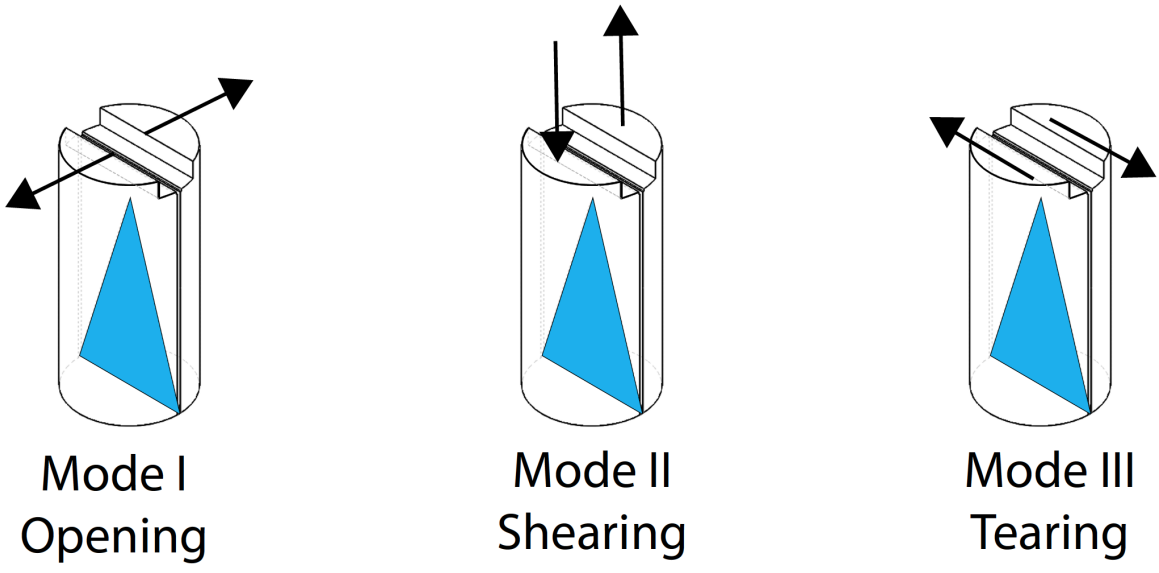


Figure 2.6: The three different modes of fracture in LEFM, shown with the geometry of a short-rod plane strain fracture toughness test. The area highlighted in blue shows the chevron shape where the force is applied during testing.

Mode I fracture occurs often and causes the most damage of the three failure modes,

and thus is studied most frequently [48]. The SIF, denoted by the letter K, comes in many forms. The most common form, K_c, the critical stress intensity factor or fracture toughness, describes the stress state for catastrophic failure of the material. Catastrophic failure occurs when the localized stress state around a flaw, typically a crack, exceeds the failure stress of the material even though the bulk stress in the material is lower than the failure stress. Other factors taken into account to calculate the SIF is the crack size and part geometry,

$$K_c = Y^* \sigma_f \sqrt{\pi\, a} \tag{2.16}$$

where a is the crack length and Y^* is a dimensionless coefficient dependent on the sample geometry, the crack geometry and the loading configuration of the sample; often found in a specific ASTM Standard. The increase in a localized stress state is caused by either a lengthening crack, or some geometry change surrounding the crack causing an increase in stress. The SIF at the crack tip eventually builds up until the material fractures at the critical SIF, K_c. Once the SIF exceeds K_c, the crack will become unstable and grow rapidly.

This study used the plane strain condition, defined by a two-dimensional strain state. It is assumed that only non-zero strain values are within the plane of interest. Given the plane strain condition, which holds true for thick components, a modified Elastic Modulus is required,

$$E' = \frac{E}{(1-\nu^2)} \tag{2.17}$$

where E is the elastic modulus and ν is Poisson's Ratio. Equation 2.17 applies for the Elastic Modulus if there are plane strain conditions due to the increase in stiffness experienced with the thickness of the material. Utilizing the plane strain assumption and critical strain energy

release rate, Ashby [2] found an approximation for K_{1c},

$$K_{1c,approx} = \sqrt{G_c\, E} = \sqrt{2\gamma_s\, E'} \approx E'\sqrt{\frac{a_1}{10}} \tag{2.18}$$

where γ_s is proportional to the elastic modulus and the interatomic spacing, a_1. In addition to the critical SIF, K_{1c}, some materials exhibit other stress intensity factors. Two stress intensity factors of interest that relate to crack growth are the crack initiation toughness, K_d, and the crack arrest fracture toughness, K_a, referred to specifically as K_{1d} and K_{1a} for Mode I fracture. The crack initiation toughness, K_d, describes the SIF at which a quasi-stable crack begins to propagate and is both temperature and loading rate dependent [51]. The temperature dependence on K_d is due to the increase in temperature at the crack tip due to plastic deformation and is accounted for as an increase in ductility [51]. The loading rate dependence is either due to the inertial effects of stress field development or the rate dependence on the plastic material response near the crack tip [51]. K_a describes the SIF at which a material can withstand quasi-stable crack growth. Quasi-stable crack growth is a type of crack growth that propagates incrementally over time. K_a can also be thought of as the ability of a material to stop a crack from propagating through the bulk of the material. Both K_d and K_a are calculated as a percentage of the fracture toughness, K_c.

2.2.4 Fracture Toughness Testing

2.2.4.1 Plane Strain Assumption There are two main conditions that are used when calculating fracture toughness, plane stress and plane strain. Plane stress occurs, in continuum mechanics cases, when the stress across a particular plane of interest is zero. The plane strain condition occurs when the non-zero components of the strain tensor act in only one plane, commonly observed in thick parts. For example, in cylindrical specimens, the length of the specimen is much greater than the other dimensions, the strains associated with the length are small when compared to the cross-sectional strains.

In general, the observed fracture toughness of a specimen decreases as sample thickness increases until the plane strain condition is reached. Specimens loaded in plane strain are constrained by the surrounding material and the strain through the thickness of the specimen is kept constant [20]. Additionally, in plane strain tests, the size of the plastic zone is small in comparison to the plastic zone size for plane stress. Keeping the plastic zone size small is important as LEFM is only applicable when the size of the plastic zone is small relative to the specimen and crack geometry [50].

To achieve valid measurements of K_{1c}, especially in polycrystalline ice, the critical stress intensity loading rate must be high enough such that strain energy stored in the material is only released to create new surfaces, and little energy is used to plastically deform the material [64]. Previous studies have found that lower critical stress intensity loading rates lead to more plastic deformation in the material, almost approaching creep [64]. As such, the critical stress intensity loading rate for Mode 1 fracture in polycrystalline ice, $\dot{K}_1^*$, should stay between 0.3 - 10 kPa $m^{1/2}$ s^{-1} at temperatures from -10°C to -20°C in order to ensure the strain energy released during fracture goes to creating new surfaces, determined by,

$$\dot{K}_1^* = \frac{K_{1c}}{t_f} \tag{2.19}$$

where t_f is the time when the sample failed, after starting the test [64]. $\dot{K}_1^*$ is calculated after each test using the K_{1c} and the time to fracture, t_f. If the $\dot{K}_1^*$ drops below the critical range, plastic work occurs and the test moves away from a pure brittle fracture.

2.2.4.2 Short-Rod Plane-Strain Fracture Toughness ASTM E 1304-97 describes the method to determine plane strain fracture toughness for a chevron notch fracture toughness test. During testing, a crack progresses incrementally through the material until the crack propagates through the whole specimen, causing catastrophic failure [4]. The crack is initiated at the tip of the chevron cut into the material due to the stress concentration

that develops at that point. ASTM E 1304-97 defines the geometry used for short-rod plane strain tests, shown below in Figures 2.7 and 2.8. Specimen geometry can be used to calculate K_{1c} as,

$$K_{1c} = \frac{P_c}{D\sqrt{W^*}} Y_m^* \tag{2.20}$$

where P_c is the peak load recorded, D and W^* are diameter and width of the samples shown in Figures 2.7 and 2.8. In addition to K_{1c}, K_{1d} and K_{1a} are calculated using Equation 2.20, where the load is the load at crack initiation or crack arrest, respectively. These values are

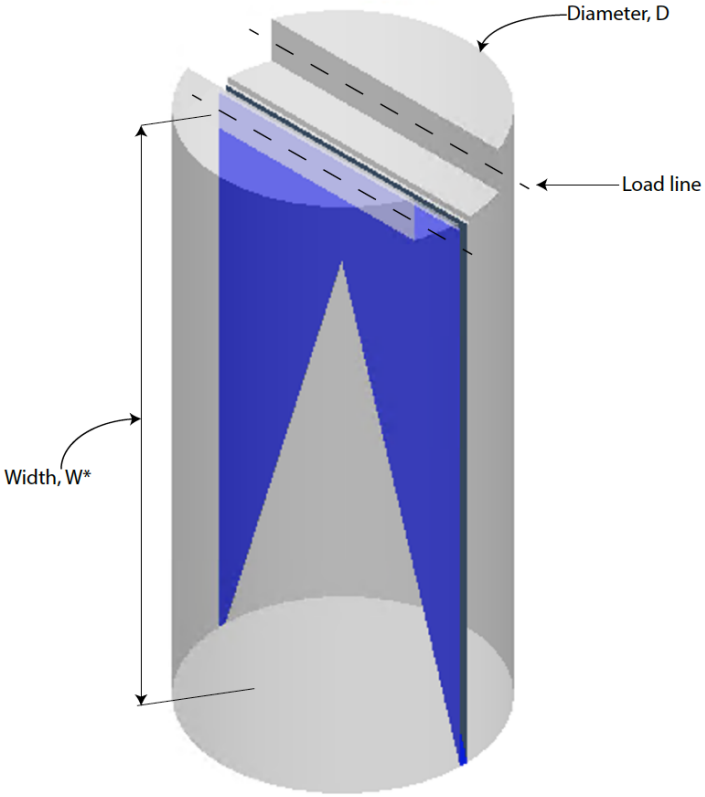


Figure 2.7: Geometry of the ice samples, defined by ASTM E1304-97 [4]. The planar feature highlighted in blue shows the area removed during sample preparation. The triangular feature, not highlighted in blue, remains at the interior of the sample. The tip of the chevron is where the stress concentration develops when the sample is loaded in tension.

compared to the calculated K_{1c} for each specimen as K_{1d} and K_{1a} are a percentage of K_{1c}. Y_m^* is a dimensionless stress intensity factor coefficient for a short rod test and allows us to calculate K_{1c} without using the crack length, taking the value of 36.25, given in ASTM E 1304-97 [4]. Y_m^* is determined by rearranging Equation 2.20, and solving for Y_m^* to get

$$Y_m^* = \frac{K_{1c} D \sqrt{W^*}}{P_c} \tag{2.21}$$

where all the variables in Equation 2.21 are the same from Equation 2.20. Using a known K_{1c} for a given material with the predetermined geometry, tests are performed, recording P_c for each test. Y_m^* is then calculated with Equation 2.21 and the minimum value is used for that geometry and applies to any material.

2.2.5 Fracture Behavior

Fracture behavior can be classified into two major groups, ductile and brittle fracture. While polycrystalline ice can undergo ductile fracture at high relative temperatures and very low strain rates, this study focused on brittle fracture. Brittle fracture occurs without appreciable plastic deformation, whereas ductile fracture occurs after significant plastic deformation [20].

Zooming in and looking at the microstructure of the material, the type of fracture can be further defined by looking at the grains along the crack surface. Intergranular fracture occurs when a crack travels along grain boundaries as shown in Figure 2.9 [20]. Generally speaking, intergranular fracture is the least common and typically occurs after the material has been subjected to a corrosive or other environment that weakens the material. The next type of fracture, and most common among engineering materials, is transgranular fracture, occurring when a crack propagates through the grains of the material, and is indicative of a ductile fracture event [20]. Finally, the last type of fracture is known as cleavage fracture. Cleavage fracture is defined by a combination of inter and transgranular fracture. Cleavage

type fracture is often found when analyzing the fracture surface of brittle materials. All three types of fracture behavior are shown in Figure 2.9. Due to the high relative strain rates tested in this study and the brittle nature of polycrystalline ice at high strain rates and temperatures, brittle cleavage type fracture is expected from all specimens.

Brittle fracture processes can be broken into three discrete stages, the first being the plastic deformation stage. While there is very little plastic deformation during brittle fracture, the plastic deformation that does occur causes dislocations to pile up at grain boundaries [20]. Next, shear stress rises in the same area where the dislocations are piled up and a microcrack is created. Finally, the stored elastic strain energy propagates the

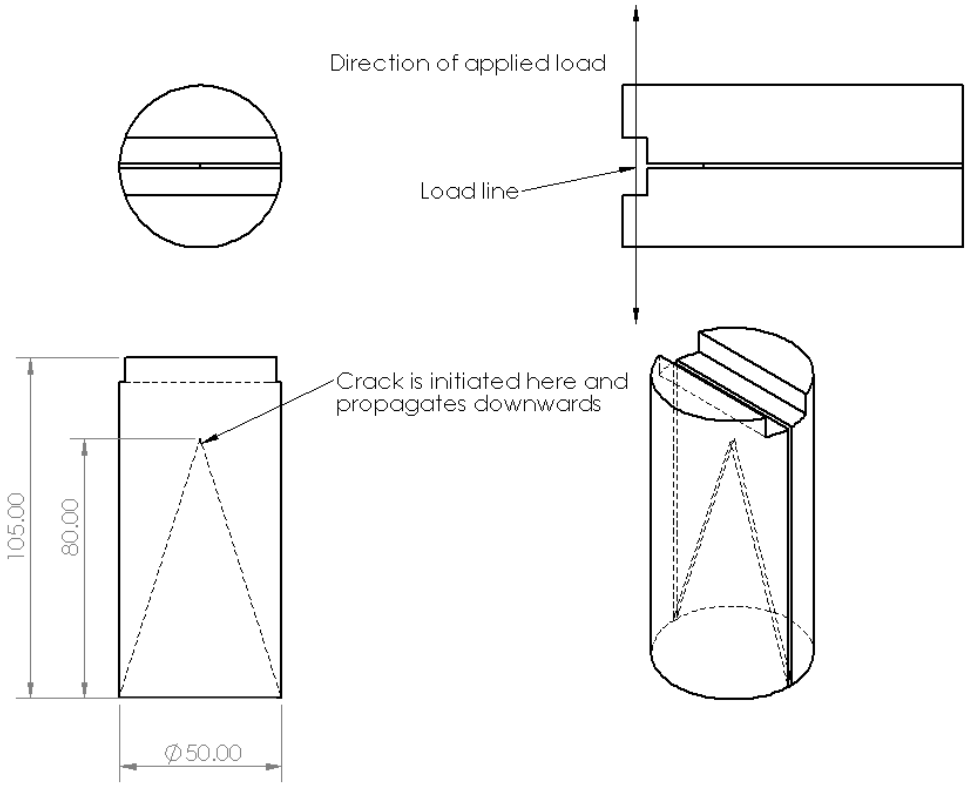


Figure 2.8: Front, top, side and perspective views of a 50 mm diameter short-rod fracture toughness specimen per ASTM E 1304-97 showing the load line, direction of applied load and the crack tip location. The chevron that is cut into the samples is a planar feature that ensures the starting location of the crack tip.

microcrack and causes brittle failure of the material [20].

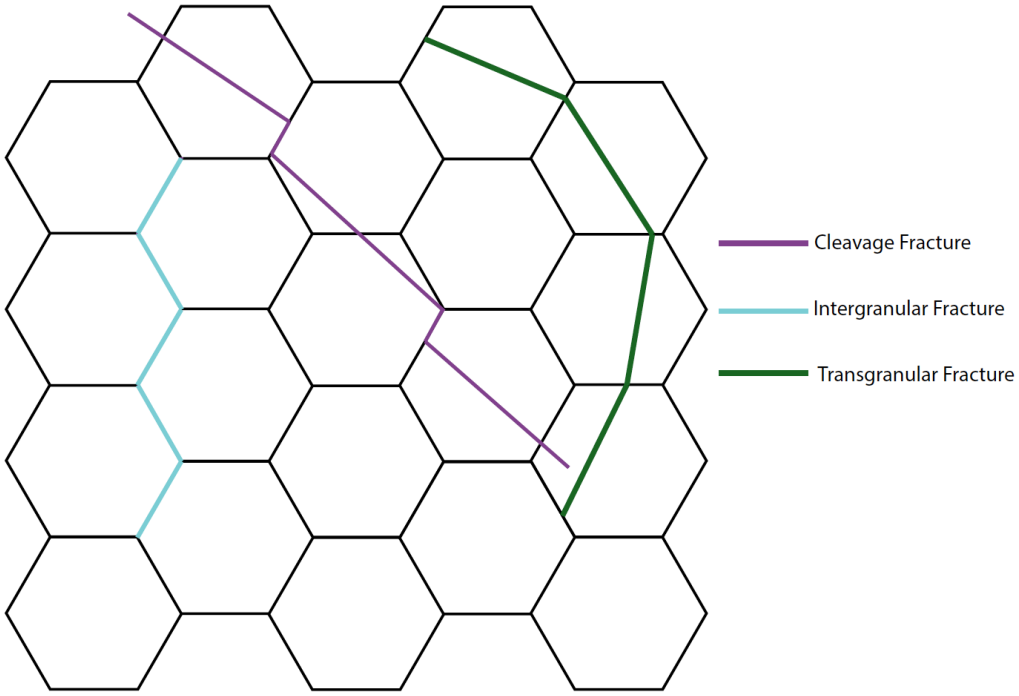


Figure 2.9: A look at a hypothetical microstructure of polycrystalline ice with oriented hexagonal grains. The three types of fracture behavior seen in both brittle and ductile fracture are shown as cleavage, intergranular and transgranular fracture.

2.3 Strengthening Mechanisms

There are many mechanisms that are used to strengthen metallic alloys, and given the crystalline structure of polycrystalline ice, some of the same mechanisms can be applied to this study. The primary strengthening mechanisms used to increase the strength of engineering alloys, that apply to polycrystalline ice, are grain boundary refinement, precipitation hardening and strain hardening. Summaries of each strengthening mechanism and the application to polycrystalline ice are presented here.

2.3.1 Grain Boundary Strengthening

First identified separately by E.O. Hall [31] and N.J. Petch [57], the Hall-Petch Relationship predicts an increase in yield strength with decreasing grain size. The relationship has come to be known as grain-boundary strengthening. Grain boundaries have been observed to be a permanent boundary that dislocations cannot cross. Additionally, piled up dislocations can impact the stress felt by adjacent grains which can cause deformation in surrounding grains. Therefore, by modifying the grain size, it is possible to change the dislocation density at grain boundaries, and by extension, yield strength, as shown here,

$$\sigma_t = \sigma_o + k_t d^{-0.5} \tag{2.22}$$

where σ_t is the yield stress, σ_o and k_t are material constants and d is the grain diameter. While the relationship was originally applied to just metallic alloys, research has been expanded to show the relationship applies to many materials. Further studies have shown the relationship holds true for hardness as well and yield stress [23, 53].

Orowan modified the Hall-Petch relationship slightly, proposing that in addition to smaller grain sizes, particles interspersed in the matrix could inhibit dislocation movement and strengthen a material in that way [1, 56]. Additionally, Orowan proposed another equation, to describe grain boundary strengthening,

$$\sigma_t = K d^{-0.5} \tag{2.23}$$

where K is a material constant (not a SIF), while σ_t and d remain the same as in Equation 2.22. Equations 2.22 and 2.23 are almost identical, the distinction that Orowan made is that the linear regression formed by the relationship between grain size and tensile strength must pass through the origin at (0,0).

Although grain boundary strengthening effects are apparent in many materials, there are conflicting results for polycrystalline ice. Reported in *Creep and Fracture of Ice* by Schulson and Duval [64], polycrystalline ice experiences an increase in tensile strength with decreasing grain size, following an Orowan or Hall-Petch relationship, depending on strain rate. Also reported by Schulson and Duval, at low strain rates, $10^{-7}s^{-1}$, polycrystalline ice exhibits an Orowan strengthening mechanism, described in Equation 2.23 where K = 0.052 MPa $m^{-1/2}$, whereas at higher strain rates, Hall-Petch strengthening occurs where σ_o and k_t are 0.52 MPa and 0.030 MPa $m^{-1/2}$, respectively at -10°C [64]. Schulson and Duval urge caution in using a Hall-Petch relationship given the dependence on the type of ice the relationship was obtained from; bubble-free, equiaxed, randomly oriented grains of freshwater ice without cracks [64].

Results from Schulson and Duval are refuted in a 2018 modeling study by Cao et al., where an inverse Hall-Petch relationship is reported for both tensile and compressive stresses with a decrease in failure stress as grain size decreases to nanometer-scale grains [15]. While the Cao et al., 2018 study was only a modeling study and included no experimental data, it does provide some insight into how polycrystalline ice may behave at minuscule grain sizes.

2.3.2 Strain Hardening

Strain hardening is performed in metallic alloys to increase strength in alloys that do not respond well to other forms of strengthening. While strain hardening is limited in materials with a hexagonal crystal structure, like polycrystalline ice, it is possible to increase strength [20]. Strain hardening is performed by plastic deformation at cold temperatures in both metal and ice, but the relative temperature for ice is higher than metals. Strain hardening causes an increase in strength from dislocation density resulting in an increase of internal energy for the system.

In materials with a crystal lattice structure, dislocations are the most common defects.

Dislocations are two-dimensional line defects that allow for the phenomena of plastic deformation to occur in all metals as described in *Mechanical Metallurgy* [20]. Defects caused by dislocations generate an elastic stress field that produces forces in other dislocations and lattice defects, increasing the overall energy of the body. Through elastic stress fields the material is strengthened by a larger dislocation density.

2.3.3 Precipitation Hardening

Precipitation hardening is a method of strengthening where atoms dissolved at high relative temperatures become insoluble at low relative temperatures and precipitate into the crystal lattice structure of a material. The precipitates do not replace an atom within the crystal structure, but instead are dispersed throughout the crystal lattice [20]. Just as dislocations are two-dimensional defects, precipitated particles act as three-dimensional defects that can either increase or decrease the strength of the material [32, 33]. Precipitated particles often act as pinning points at the grain interiors for dislocation movement [20]. Ca^{++} ions have been shown to increase the strength of polycrystalline ice by precipitating at the grain boundaries, whereas H_2SO_4 reduces the strength of polycrystalline ice [32, 33].

CHAPTER THREE

METHODS

3.1 Sample Creation

In order to determine the crack arrest fracture toughness of ice, samples were manufactured and tested in a controlled environment. The samples were created following the procedure from Cole (1979) and Hammonds and Baker (2016) [17, 32]. Two different size setups were fabricated; one that produced samples at 50 mm diameter and the other at 90 mm diameter, chosen because they are common ice core drill sizes, allowing for comparison to meteoric ice samples of the same diameter. Both molds produced samples long enough such that a 2:1 width:diameter ratio, geometry provided by ASTM E 1304-97, could be cut without imperfections at the ends of the samples [4]. The setups used a machined aluminum mold wrapped in an ethylene glycol chilled copper coil to control freezing rate. The copper coil created a constant temperature gradient that ensured a consistent freezing rate.

The end caps of the mold were made from machined Delrin with a port on top and bottom for both water and vacuum. The ports were connected with brass Swagelok quick connect fittings. The entire system was assembled using brass plumbing fittings to ensure it was both air- and water-tight. Deionized (DI) water was pre-chilled and degassed using a GEOKON deaerator with an in-line vacuum pump. Prior to entering the mold, the deaerated water flowed into a copper coil submerged in an ice bath in order to maintain the temperature as close to freezing as possible. An image of the setup is shown in Figure 3.1. A simplified flow diagram of the setup shown in Figure 3.1 is shown in Figure 3.2. The tank on top in Figure 3.1 is the GEOKON deaerator used to de-gas the DI water. From that tank, the DI water flows through a copper coil immersed in an ice bath used as secondary cooling for the DI prior to filling the mold. The DI water flows out of the coil inside the ice bath and into

the bottom of the mold, wrapped in insulation and an ethylene glycol chilled copper coil to maintain temperature inside the mold. The ethylene glycol is held at a constant temperature to control the freezing rate within the mold. The water flows through the mold and into the Buchner flask. The Buchner flask is also attached to the vacuum pump as the vacuum pump controls the pressure of the entire system.



Figure 3.1: The setup used to create the ice samples. The water flows from the top tank into the white bucket and then into the mold. During the freezing process, water is flowing constantly. Once the water leaves the top of the mold, it flows into a buchner flask that is tucked behind the mold. The inside temperature of the refrigerator was set to 1.0°C.

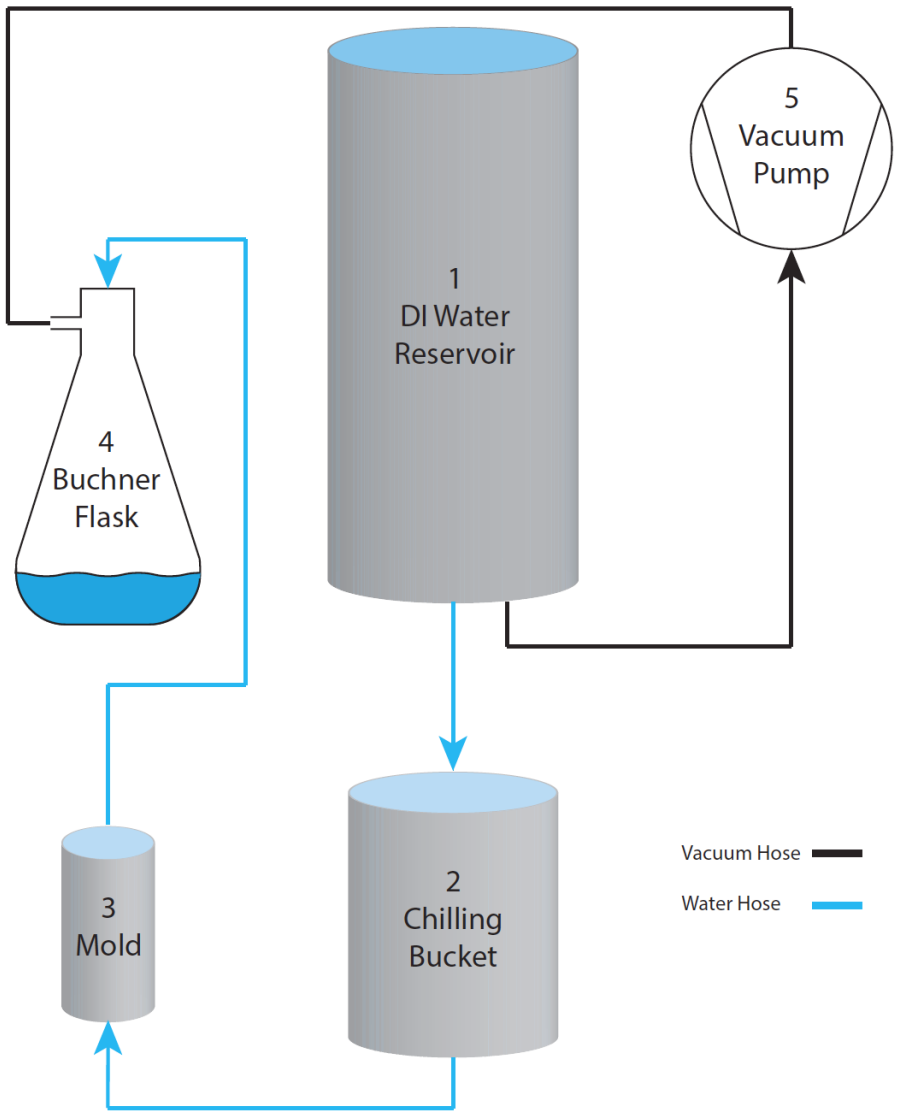


Figure 3.2: A simplified flow chart for the sample creation process.

3.2 Freezing Process

The mold is packed with seed grains of ice, obtained by blending DI water ice cubes, passing a 1.18 mm sieve, but not passing a 0.85 mm sieve. The packed mold was flooded with pre-chilled, degassed water below 2°C before freezing radially at an average rate of 2.8 μm/s, calculated based on the total freezing time [17]. Throughout the entire freezing process,

chilled, degassed water flowed through the mold to ensure a low concentration of dissolved gas, and therefore bubbles, at the freezing front and to accommodate volume changes in the sample with the advancing freezing front. The freezing process for the 50 mm diameter samples took approximately 2 hours, while the 90 mm diameter samples took approximately 5 hours.

The samples were removed from the mold by raising the temperature of the glycol to 3°C until the sample slid out of the mold. The samples were then held below -5°C for 24 hours before collecting density and grain size measurements. A photo of each sample size is shown in Figure 3.3; where the 50 mm diameter sample has been cut to the correct width, while the 90 mm diameter sample has just been removed from the mold.



Figure 3.3: Photo of both the 50 and 90 mm diameter samples in the Subzero Research Laboratory at MSU. The 50 mm diameter sample has been cut to the correct width while the 90 mm diameter sample has not been cut to width.

3.3 Sample Properties

The sample creation technique used for this study produced samples with 50 mm and 90 mm diameter, an average density of 892.3 kg/m^3 and average grain size of 0.96 mm. Bulk sample density was measured by determining sample diameter, sample width and sample weight, whereas grain size was determined by ASTM E 112-10 [3]. Mold vacuum time, DI water deaeration time, freezing temperature and mold flow rate were varied, in order to obtain the highest density and clearest ice samples, discussed in Section 3.6. Cutting a thin section sample, analyzed through cross polarized light, produced images similar to Figure 3.4, showing a random grain orientation.

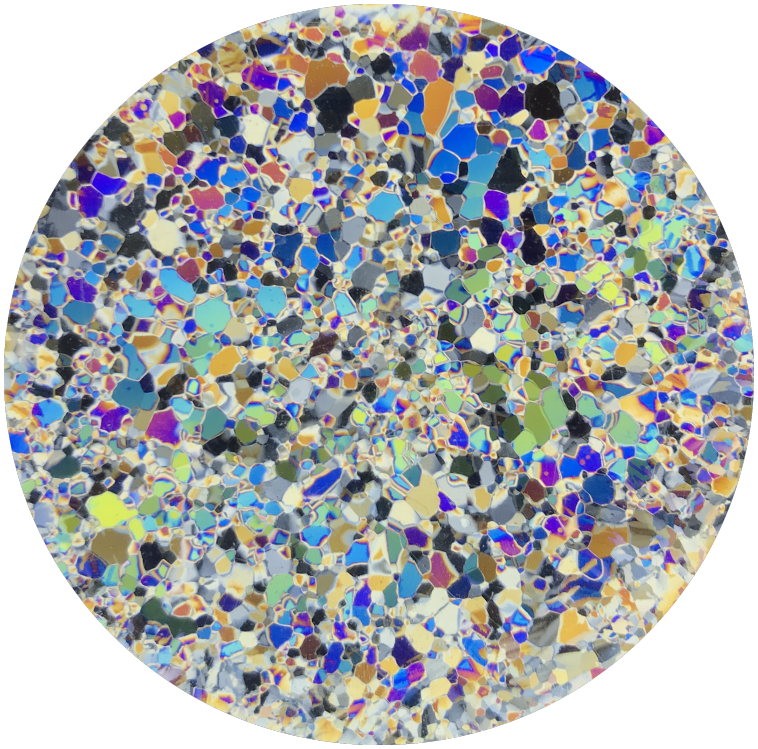


Figure 3.4: A thin section imaged under cross-polarized light. The different colors represent different c-axis orientations in the ice sample.

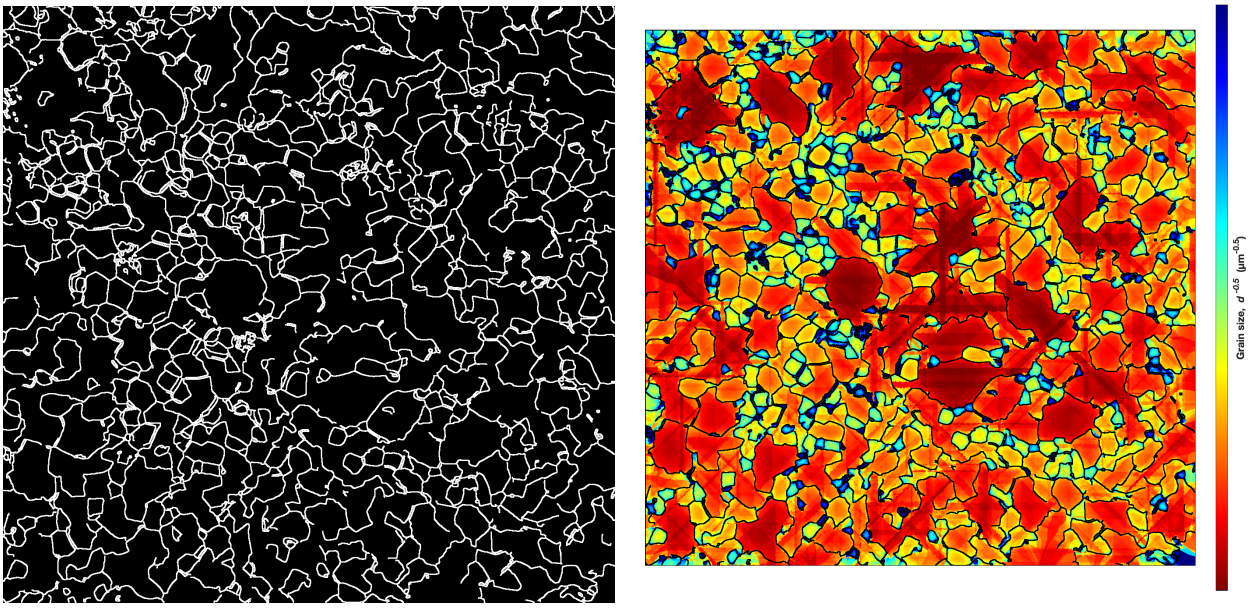
Thin sections cut from each sample were analyzed using cross-polarized light in the

Subzero Research Laboratory (SRL). Grain size for each sample was analyzed using two separate methods. The first method followed the intercept method defined in ASTM E 112-10 [3] while the other method was performed using a scripted grain size measurement code developed for measuring grain size in metallic alloys adapted to work with ice. The intercept method defined by ASTM E 112-10 involves drawing a test line on the thin section image and manually counting the number of grain boundaries that intercept that line [3]. With a known length of the line, the average grain size can be calculated. The scripted method was developed at Aalto University using a point-sampled intercept length method in MATLAB, hereafter referred to as the Lehto script. The grain size is measured for individual grains at random points in the sample interior repeatedly in four directions to get an accurate average grain size for each individual grain [42, 43].

The Lehto script expects a black and white input image with well-defined grain boundaries and interiors [42, 43]. In order to use the Lehto script, images produced from this study, such as Figure 3.4, had to be processed in order to remove all color. A MATLAB script was created to perform preliminary image processing such that the Lehto script could be used for thin section images. This script was modified from from Hammonds and Baker, 2016 and 2018 [32, 33]. The preliminary image process script took the input images, converted them to grayscale, binarized the images and increased the grain boundary contrast. An example of an input image and an image produced by the Lehto script are shown in Figure 3.5 [42, 43]. In combination, these two scripts produced thin section images that accurately estimate average grain size of polycrystalline ice. A comparison of both methods is shown in Table 3.1, showing the two methods produced similar results for the analyzed samples. The scripted method in MATLAB provided a larger range of grain sizes than the ASTM method with an average percent difference between the methods of 10%. The average grain size of all samples produced during this study was 0.95 ± 0.28 mm.

Table 3.1: Comparison of the minimum, maximum and average grain size provided by each grain size measurement method. Overall, the Lehto script calculates a larger average grain size than the average grain size calculated by the ASTM E 112-10 intercept method [3, 42, 43].

Method	**Minimum Grain Size, mm**	**Maximum Grain Size, mm**	**Average Grain Size, mm**
ASTM E112-10	0.66	1.23	0.95
MATLAB	0.71	1.38	0.99



(a) Output from the MATLAB image processing script to prepare images for the Lehto script.

(b) Output from the MATLAB grain size measurement code developed by Lehto [42, 43].

Figure 3.5: Image from the MATLAB image processing script to remove color from the thin section images and allow for grain boundary identification, shown on the left, this script was modified from Hammonds and Baker, 2016 and 2018 [32, 33]. Shown on the right is an image from the Lehto grain size measurement script [42, 43].

3.4 Sample Preparation

After the sample temperature equalized to -5 to -10°C, the samples were cut to a width:diameter ratio of 2:1, provided by ASTM E 1304-97 [4]. Diameter, width and weight were measured for each sample such that bulk density could be determined. Cutting fixtures were designed and fabricated for each sample size to keep the final dimensions consistent. All fixtures ensured the final dimensions of each sample to match geometry from ASTM E 1304-97 in order to perform short-rod plane-strain fracture toughness testing [4]. ASTM E 1304-97 describes the testing procedure for short-rod plane-strain fracture toughness testing of materials [4]. The final geometry of the sample is shown in Figures 2.7 and 2.8 in Chapter 2. The SolidWorks models for each ice sample were used to create the necessary fixtures and jigs used to cut the samples in the SRL at MSU. All fixtures were designed to cut the samples on the band saw in the SRL clean room. All fixtures were 3D printed at MSU in the Norm Asbjornson Mechanical and Industrial Engineering Machining Lab with assistance from Joe Eldring.

In order to make sure each cut was aligned with the previous cuts, a sled was designed to hold each saw fixture in place. The sled fit directly into a groove on the table of the band saw and maintained alignment with the blade and is shown in Figure 3.6. The first cut made on each sample removes a channel of ice through the top of the sample. The channel is used to locate the ice sample for all additional cuts. Figure 3.7 shows an image of the fixture used to cut the channel and what the ice sample looks like once the cut is complete. The red component in Figure 3.7 slides back and forth on the sled in order to cut the channel. After cutting the channel into the top of the sample, an additional, narrower notch is cut at the center of the channel to provide a place for the Crack Mouth Opening Displacement (CMOD) gauge to sit. An image of the fixture used to cut the channel for the CMOD gauge is shown in Figure 3.8. The only difference between the fixture used for the CMOD channel

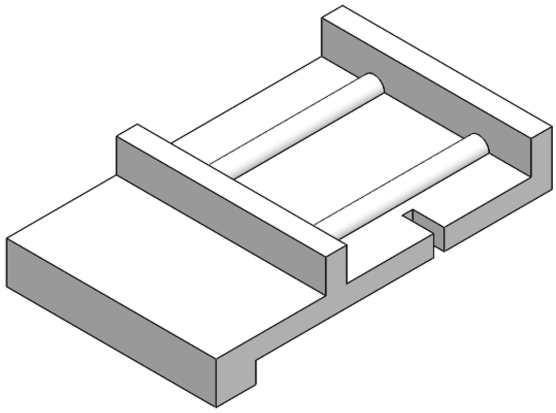
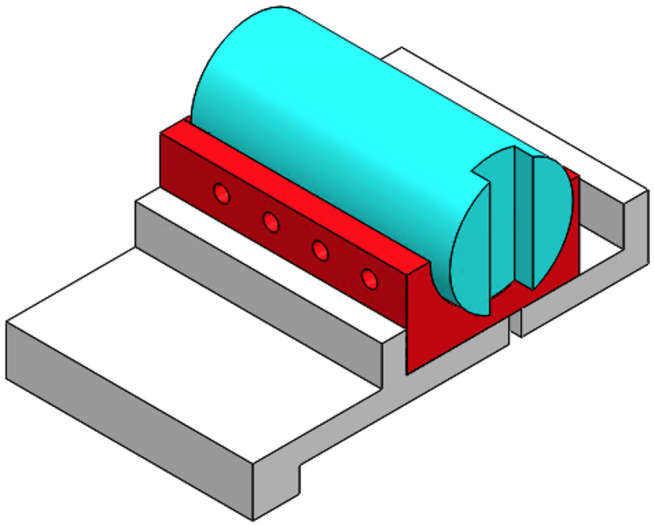
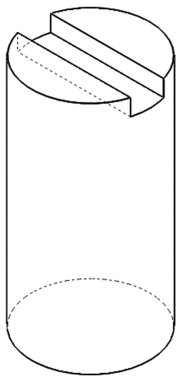


Figure 3.6: SolidWorks model of the sled designed and fabricated at MSU. The sled fit into a channel on the table of the band saw and kept all the cuts aligned during sample preparation.



(a) SolidWorks model of the saw fixture used to cut the top notch in the ice sample.



(b) SolidWorks model of an ice sample after the top notch has been cut on the band saw.

Figure 3.7: Models of the fixture used to hold the ice sample while cutting the top notch and the ice sample after the top notch has been cut. The fixture used to cut the top notch slides back and forth on the sled in order to cut out the channel shown on the right.

and the fixture shown in Figure 3.7 is that the CMOD fixture is wider, allowing for less side-to-side motion when cutting the narrower notch. In order to cut the chevron into the sample, a fixture was designed to hold the ice sample at a 17.35° angle with respect to the band saw blade. An additional fixture was designed and fabricated to locate the chevron fixture on the sled, called the sled insert. Figure 3.9 shows a perspective view of the fixture, designed and fabricated at MSU, to hold each ice sample in place while the chevron notch is cut into the center of the sample. The fixture used to cut the chevron is shown in brown, the sled is shown in gray, the sled insert is shown in green and the ice sample is shown in blue. Detailed, dimensioned drawings of all fixtures are available in Appendix A.

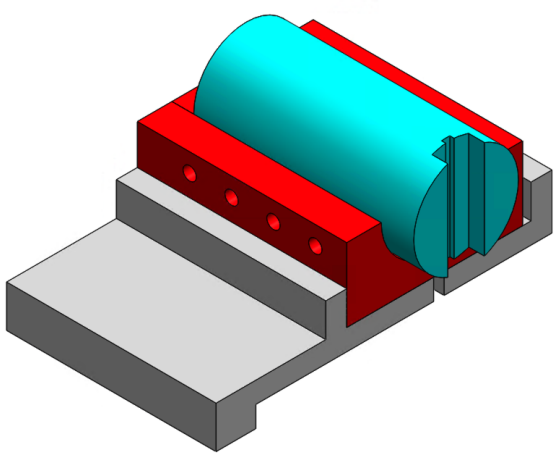


Figure 3.8: SolidWorks model of the CMOD fixture designed and fabricated at MSU. The fixture fits onto the sled and slides back and forth to cut the notch used to locate the CMOD gauge during testing. This fixture is functionally the same as the one displayed in Figure 3.7, but only allows for 4 mm of side-to-side movement.

3.5 Fracture Testing

Short-rod plane-strain fracture toughness testing of the samples was performed in accordance with ASTM E 1304-97 [4]. The samples were brought to the test temperature inside the test frame, a Materials Test Systems (MTS) electromechanical load frame,

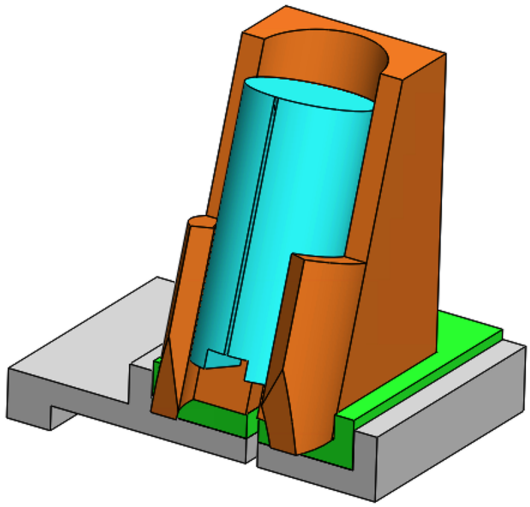


Figure 3.9: SolidWorks model of the chevron fixture, sled, sled insert and ice sample. The fixture used to cut the chevron is shown in orange, the sled is shown in gray, the sled insert is shown in green and the ice sample is shown in blue.

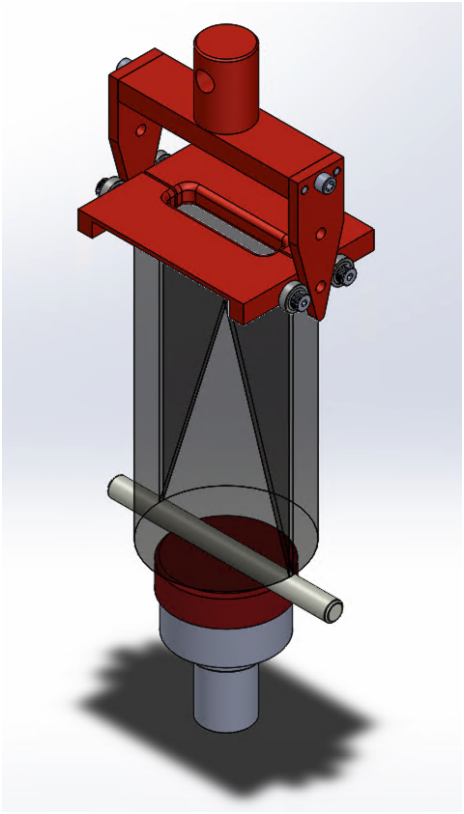
outfitted with an MTS Series 651 environmental chamber. The environmental chamber is temperature controlled using liquid nitrogen as a cooling agent and a Eurotherm 2408/2404 Process Controller. The load frame was controlled using MTS TestSuite Elite with a modified compression test template to detect fracture when the load drops. While the samples were all loaded and fractured in tension, due to the sample setup described above, the load frame crosshead was moving downward and thus was programmed using a compression test template. Samples were tested at -10°C and -20°C.

All tests were performed under a displacement rate controlled regime of $5e^{-6}$ m s^{-1} with a critical stress intensity loading rate, $\dot{K}_1^*$, ranging from 0.127 - 1.469 kPa $m^{1/2}$ s^{-1}. While the applied load during testing was applied in the same direction as a traditional short-rod plane strain fracture toughness test, due to size constraints within the environmental chamber, the samples needed to be oriented differently. Typically, a short-rod plane-strain fracture toughness test is carried out with the sample oriented as previously shown in Figure 2.8. Due to the size of the samples and the small interior dimensions of the environmental

chamber, the test setup was modified. Figure 3.10 shows the orientation of the test setup inside the environmental chamber. The modified test setup allowed for the rotation of the test geometry while still achieving quasi-stable incremental crack growth in the ice samples. In both test orientations, the crack surface is perpendicular to the applied load, similar to a double cantilever beam test. While the sample orientation changed for the test setup, the fracture mode and fracture behavior is the same as a standard short-rod plane-strain fracture toughness test.



(a) Test setup inside the environmental chamber. The small, black, rectangular component sitting on the top of the sample is the MTS CMOD gauge.



(b) Model of the test setup in SolidWorks. Each component was modeled individually and then added to a SolidWorks Assembly.

Figure 3.10: Picture and model of the test setup inside the environmental chamber

The fracture surface is rotated from the initial configuration and is now parallel to the load frame crosshead motion. The top plates, shown in Figure 3.10 in red on the right side

and in white on the left side are two separate pieces that fit into the top channel cut into the ice sample. As the crosshead moves downwards, the wedge shaped pieces engage with the two plates sitting on top of the sample. The two plates lock into place on the sample using the channel in the top of the sample shown in Figure 3.7b. The wedges directly interact with the bearings shown in Figure 3.10 and the wedges drive the sample to fracture in tension, i.e. Mode I opening fracture. The small gauge seen in Figure 3.10a is a MTS CMOD clip gauge. The clip gauge is attached directly to the ice sample and measures displacement as the ice sample is wedged apart by the load frame. While the test setup has been modified from the typical short-rod plane-strain fracture toughness test, the same results are achieved as previous studies. The MTS load frame outputs crosshead displacement, crosshead load and CMOD data into a text file. The displacements and loads are calculated using trigonometric relationships used when designing the wedge fixtures.

3.6 Troubleshooting

3.6.1 Ice Quality

Ice quality, particularly bubble concentration, was found to be dependent on controllable parameters during the freezing process. All efforts to improve the quality of the ice samples were to reduce the bubble concentration and the associated porosity. The identified factors below are known to impact bubble concentration.

It was observed that mold vacuum time had an impact on the bubble concentration in the final sample, shown by Pearson's correlation analysis in Tables 3.2 and 3.3. Freezing rate of the ice also impacted the final bubble concentration within the ice as longer freezing times allow the dissolved gasses to work their way out of the seed grain compact. While ice with a low concentration of bubbles was produced in this study, bubbles were not completely eliminated from the ice samples. For this investigation, freezing rate for the tested samples was held constant, although to further reduce bubble concentration, a much lower freezing

rate would be required, without impacting mean grain size. Ideally, the samples would be bubble-free, as bubbles can be a nucleation point for a microcrack that could have a smaller diameter than the chevron tip.

3.6.1.1 Deaeration Time Prior to filling the mold with water, the DI water is degassed, or deaerated, in a GEOKON deaerator. The deaerator has an impeller at the bottom that violently agitates the water causing nucleation, cavitation and expulsion of dissolved gasses. The deaerator is connected to a vacuum pump to draw off the dissolved gasses, leaving the user with deaerated water. The literature provided by GEOKON states that a deaeration time of 3 - 5 minutes should be sufficient, but it was found that longer deaeration time yielded slightly higher density depending on the sample size [24].

In order to determine the factors that influence bubble concentration, a Pearson correlation analysis was performed on the data. A correlation analysis is a statistical measurement of the quality of the relationship between two variables, where the covariance of each variable is divided by the product of their standard deviations [38]. The value ranges from -1 to 1, with the low-end indicating a perfectly negative relationship (increase in one variable means decrease in the another) and a value of 1 indicative of a perfectly positive relationship (increase in one variable means an increase in the other). The correlation analysis results for both 50 mm and 90 mm diameter sample set can be found in Tables 3.2 and 3.3, respectively.

3.6.1.2 Mold Vacuum Time While the DI water in the deaerator is being degassed, the mold filled with seed grains is also under vacuum, with the intent to remove any air from pore spaces in the seed grain compact. Tables 3.2 and 3.3 both show a positive correlation between increasing mold time under vacuum and increasing density. This suggests that more time with the packed mold under vacuum will yield a higher sample density. Deaeration times for this study range from 20 to 240 minutes and mold vacuum times range from 0 to 240

minutes, with Tables 3.2 and 3.3 showing a positive relationship between mold vacuum time and density.

Table 3.2: Pearson's correlation coefficient analysis between deaerator time and mold vacuum time with respect to final sample density for 50 mm samples. There is an observed positive correlation between both deaerator Time and Mold Vacuum Time with Sample Density with a stronger relationship between Mold Vacuum Time and Density.

	Deaerator Time	**Mold Vacuum Time**
Density	0.004	0.13

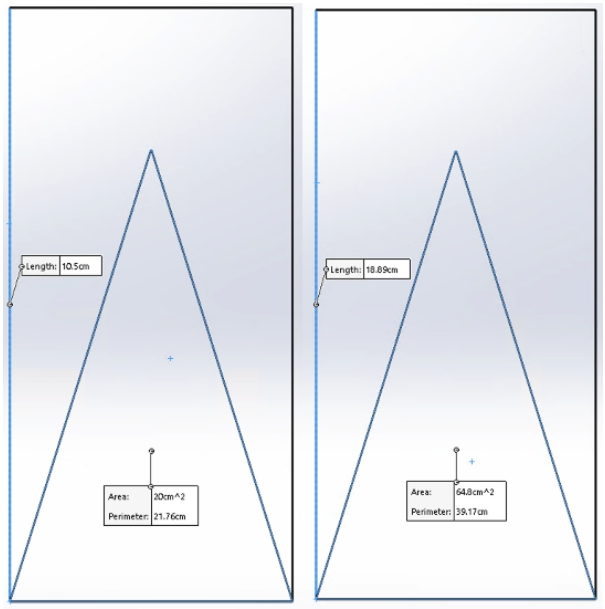
Table 3.3: Pearson's correlation coefficient analysis between deaerator time and mold vacuum time with respect to final sample density for 90 mm samples. There is an observed positive correlation between both deaerator Time and Mold Vacuum Time with Sample Density with a stronger relationship between Mold Vacuum Time and Density.

	Deaerator Time	**Mold Vacuum Time**
Density	0.15	0.35

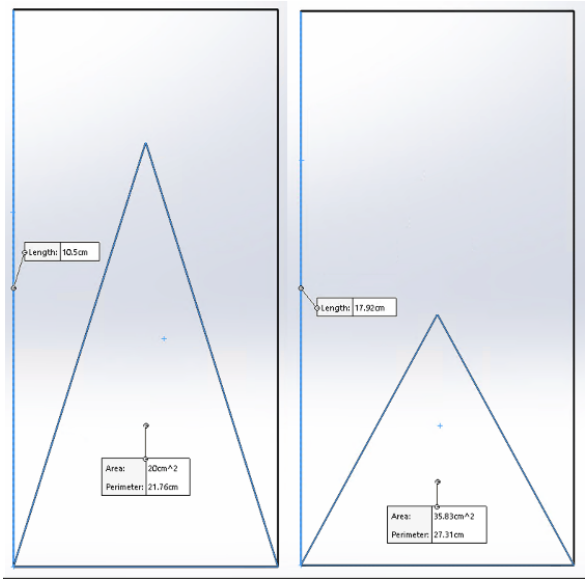
3.6.1.3 Freezing Time and Temperature Two closely correlated parameters analyzed were the freezing time and temperature. The freezing time was heavily influenced by the temperature gradient applied by the chiller on the exterior of the mold. Once the extent of the gradient was determined, the freeze time for each sample could be tightly controlled. A parameter that was initially taken for granted, was the temperature of the input water to the mold. Prior to filling the mold with the degassed water, the temperature was recorded to ensure it was close to 2°C. If the input water temperature was higher than 2°C, the temperature on the glycol chiller needed to be reduced in order to achieve the same freezing rate outlined by Cole [17]. With an input water temperature higher than 2.5°C, the samples did not freeze in the allotted time, 2.5 hours for 50 mm samples and 5 hours for 90 mm

samples. If the sample was removed after 2.5 or 5 hours, for 50 mm and 90 mm diameter samples respectively, when the input temperature is too high and the chiller temperature was not adjusted, the core of the sample was partially liquid and the sample was unusable.

3.6.1.4 Chevron Geometry of 90 mm Diameter Samples When testing began on the 90 mm diameter samples, it was difficult to achieve quasi-stable crack growth behavior. In an attempt to achieve quasi-stable crack growth, the chevron geometry was modified in order to match the ratio of sample width:chevron area in the 50 mm samples. Initially, this ratio was not held constant between the two sample sizes. Instead, the ratio of sample width:chevron height was held constant. The initial chevron geometry for each 50 mm and 90 mm samples can be seen in Figure 3.11a. In the 50 mm sample, the ratio of sample width:chevron area was 0.525, while the same ratio in the 90 mm samples was 0.292 prior to modifying the geometry. Figure 3.11 shows how the chevron area was modified to keep the ratio between the 50 mm and 90 mm samples consistent. While Figure 3.11a appears to show the same ratio of sample height to chevron area between the two sample sizes, due to the circular cross section, the correct ratio between the two sample sizes is shown in Figure 3.11b.



(a) On the left is the 50 mm sample chevron geometry and on the right is the 90 mm sample chevron geometry prior to modification. The geometric relationships between the chevron and sample match between the two sample sizes.



(b) The left shows the 50 mm sample chevron geometry with the 90 mm modified chevron geometry on the right. The modification was made on the 90 mm diameter sample to match the sample width:chevron area ratio in the 50 mm sample.

Figure 3.11: The left figure shows how the 50 mm and 90 mm samples have identical geometric relationships for the chevron. The right figure shows the adjusted chevron area relationship in order to keep the ratio of sample width to chevron area the same between sample sizes. Due to the circular cross section of the samples, the sample width:chevron area relationship is not consistent between the two sample sizes.

CHAPTER FOUR

RESULTS AND DISCUSSION

Presented herein are fracture test results from eleven 50 mm diameter and thirty-four 90 mm diameter laboratory-manufactured polycrystalline ice samples which fractured with unstable, stable and quasi-stable crack growth, shown in Table 4.1. The data presented is the first to show K_{1c}, K_{1d} and K_{1a} of laboratory-manufactured polycrystalline ice comparable to meteoric ice. This study tested samples with diameters of 50 and 90 mm and a width:diameter ratio of 2:1. The average bulk density and grain size of all samples was 892.33 $\pm$ 10.08 kg/m^3 and 0.96 $\pm$ 0.28 mm, respectively. All tests were performed in a displacement controlled regime in a temperature controlled environment using a short-rod plane-strain fracture toughness test. Displacement measurements were taken using a crack mouth opening displacement (CMOD) gauge that measured deflection at the notch mouth with an applied tensile load. Load and displacement data were recorded on the MTS load frame from 50 - 200 Hz. Table 4.1 shows data from each sample tested in this study and some of the calculated values discussed below.

Table 4.1: All calculated parameters for each sample, blanks in this table represent samples that did not exhibit stable or quasi-stable crack growth and thus do not have a K_{1d} or K_{1a}. All sample numbers with a * indicate the modified chevron geometry and have been excluded from portions of the analysis.

Sample Size, mm	Sample Number	Bulk Density, kg/m^3	Grain Size, mm	K_{1c}, kPa $m^{1/2}$, Eq. 2.20	K_{1d}, kPa $m^{1/2}$, Eq. 2.20	K_{1a}, kPa $m^{1/2}$, Eq. 2.20	U^*, J/m^3
50	13	888.92	0.82	28.24	28.19	6.66	12.35
50	14	891.47	0.84	23.71	23.71	4.28	8.16
50	20	875.79	0.72	45.17	13.43	1.65	15.22
50	21	890.31	0.66	27.17	19.35	8.66	6.97

Sample Size, mm	Sample Number	Bulk Density, kg/m^3	Grain Size, mm	K_{1c}, kPa $m^{1/2}$, Eq. 2.20	K_{1d}, kPa $m^{1/2}$, Eq. 2.20	K_{1a}, kPa $m^{1/2}$, Eq. 2.20	U^*, J/m^3
50	23	913.30	0.74	53.52	27.22	9.62	22.22
50	24	888.37	0.77	32.98	18.80	4.34	16.32
50	27	895.29	1.01	53.40	49.90	23.28	37.75
50	28	897.36	0.92	61.67			22.06
50	29	893.86	1.16	51.52	42.40	17.36	33.03
50	30	895.66	1.15	85.97	65.61	34.15	149.52
50	31	911.21	1.22	49.72	49.72	13.56	19.69
90	8	874.29	0.88	76.20			123.54
90	9	876.32	0.98	36.24			34.76
90	11	868.49	0.98	47.59			57.35
90	12	874.89	0.87	41.42			38.89
90	13	886.76	0.85	73.87			131.62
90	14	889.66	0.96	19.78			9.60
90	15	885.60	0.80	75.95			114.05
90	18	900.76	0.92	26.54			20.20
90	19	891.40	0.88	41.77			41.56
90	20	895.44	0.98	55.19			82.79
90	21	889.82	0.95	49.27			57.54
90	22	890.25	0.95	71.62			104.44
90	23	889.61	0.94	49.96			50.89
90	25	885.74	1.09	30.17			19.15
90	26	890.10	0.93	60.38	47.57	40.55	85.20
90	27	893.59	0.88	39.70			30.96
90	29	886.72	0.91	79.29			131.64

Sample Size, mm	Sample Number	Bulk Density, kg/m^3	Grain Size, mm	K_{1c}, kPa $m^{1/2}$, Eq. 2.20	K_{1d}, kPa $m^{1/2}$, Eq. 2.20	K_{1a}, kPa $m^{1/2}$, Eq. 2.20	U^*, J/m^3
90	31	892.79	0.93	41.70			40.82
90	32	883.00	0.92	102.97	14.40	13.87	243.67
90	33	885.58	0.98	93.29	72.85	55.94	256.74
90	34	896.87	0.90	46.62			43.10
90	35	892.99	0.94	55.25			61.22
90	38*	895.49	1.10	16.22			2.50
90	40*	889.12	0.98	18.76			2.68
90	41*	898.68	1.16	20.72			3.72
90	42*	893.75	1.10	16.02			2.05
90	43*	878.71	1.09	69.37			37.43
90	44*	898.01	1.14	18.38			2.63
90	45*	885.08	1.01	43.02			17.89
90	46*	879.53	1.23	39.20			13.71
90	47	886.74	1.22	59.96			73.44
90	48	891.95	1.07	47.25	16.01	14.32	52.42
90	49	898.73	0.95	21.46			10.34
90	50	892.80	0.98	24.33	20.12	19.94	12.07

4.1 Stable and Quasi-Stable Crack Growth

Figure 4.1 shows sample behavior in response to loading for a 50 mm diameter sample with two increments of crack growth prior to catastrophic failure. A crack initiates at the load designated by F_o, progresses rapidly, indicated by decreasing load, and is arrested at the load A_o. The same sequence occurs at F_1 and A_1, but at F_2, the crack propagates catastrophically and the sample fractures. The curve does not start at (0,0) because a small pre-load was applied in order to hold

the sample in place. The behavior seen in Figure 4.1 matches behavior shown in Rist et al., 1999, 2002 which also used short-rod specimens but on meteoric ice cores from the Filchner-Ronne Ice Shelf in Antarctica [61, 62]. While only two samples in this study showed two increments of incremental crack growth prior to failure, all samples that fractured with stable or quasi-stable crack growth show similar 'sawtooth' behavior of crack growth and arrest.

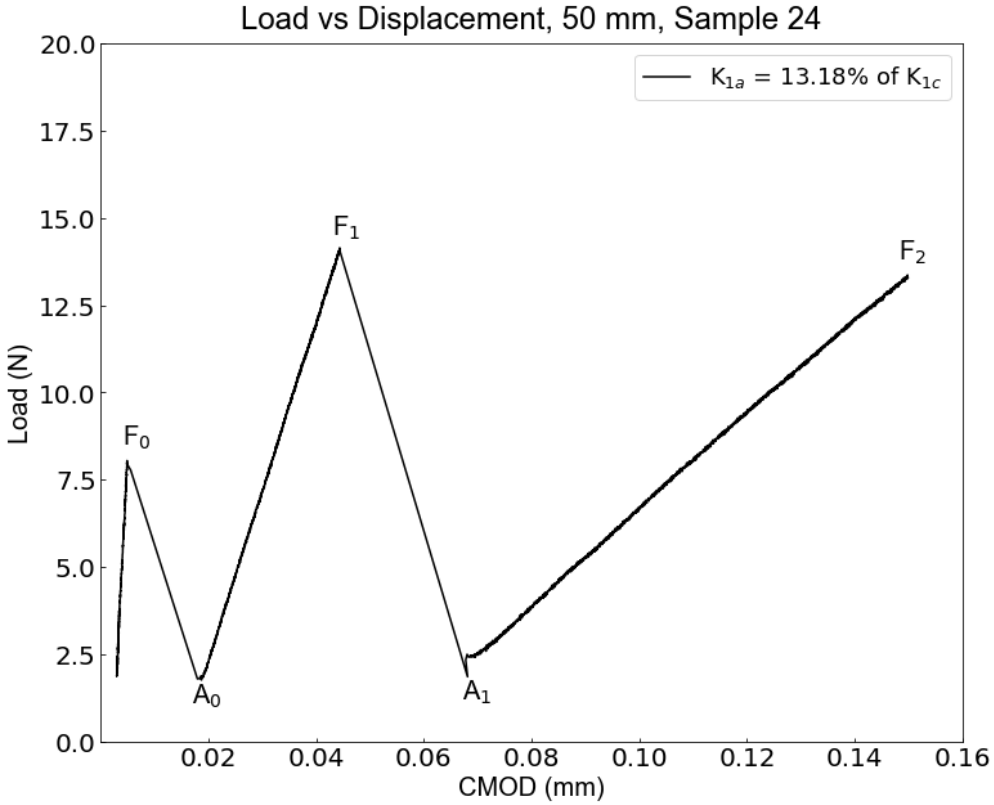


Figure 4.1: Load vs Displacement (CMOD) for 50 mm Sample 24. The 'sawtooth' behavior is indicative of crack initiation and arrest throughout the test. K_{1a} is calculated using Equation 2.20 at both A_0 and A_1 while K_{1d} is calculated using Equation 2.20 at both F_0 and F_1. This sample showed two increments of crack growth, so two values for K_{1d} and K_{1a} are calculated. K_{1c} is calculated using the load indicated by F_1. For this sample, the maximum load also occurred during a segment of crack growth and arrest, so K_{1d} and K_{1c} are both calculated using the point F_1. The curve does not start at (0,0) because a small pre-load was applied in order to hold the sample in place.

The results show that laboratory-manufactured polycrystalline ice is capable of fracturing with stable and quasi-stable crack growth. The type of data displayed in Figure 4.1 was used to calculate

the K_{1c}, K_{1a} and K_{1d} for each sample. The peak loads, denoted by F_x in Figure 4.1, show points of crack initiation and thus were used to calculate K_{1d} using Equation 2.20, whereas the valleys, denoted by A_x, show points of crack arrest and these points were used to calculate K_{1a}. K_{1c} was calculated using the highest load prior to catastrophic failure of each sample. Each calculation for K_{1c}, K_{1d} and K_{1a} are made using Equation 2.20. The load indicated by F_2 shows the load reached prior to catastrophic failure of the sample. Two samples, 50 mm Samples 14 and 24, displayed two increments of incremental crack growth before failure; all other samples had one increment of crack growth prior to failure. For samples with two crack growth increments, the largest K_{1d} and K_{1a} are used. In both Sample 14 and 24, the peak load reached by the sample was not achieved immediately before catastrophic failure, instead, the peak load was reached prior to an increment of crack growth. As on two samples displayed multiple increments of crack growth, it is unknown if this behavior is representative of all polycrystalline ice samples, or if this behavior was caused by another test parameter.

The slope of each increment of increasing load on the load vs displacement curve is the material stiffness, denoted by k. Shown below in Table 4.3, the stiffness of the sample decreases after the each crack growth increment. This investigation is the first to show that laboratory-manufactured polycrystalline ice is capable of fracturing with stable and quasi-stable crack growth in a short-rod plane strain fracture toughness test. Previous studies have tested meteoric ice cores from various ice shelves and from freshwater cores of columnar lake ice, with similar results to those presented in this study [64].

4.1.1 Fracture Behavior

Figure 4.2 shows photos of fracture surfaces of polycrystalline ice samples from this study. Shown on the left, 90 mm Sample 31, did not fracture with incremental crack growth, while 90 mm Sample 33, shown on the right, did fracture with incremental crack growth. These two fracture surfaces have different topography, shown by the shaded and brighter regions on Figure 4.2b. These fracture surfaces are indicative of cleavage-type fracture behavior due to their reflectance and granular nature. Ductile fracture surfaces are characterized by dull appearance and fibrous

Table 4.3: CMOD and stiffness (Slope) data for each sample that exhibited stable or quasi-stable crack growth behavior. Blanks in this table represent samples that only had one increment of crack growth prior to catastrophic failure.

Sample Size	**Sample Number**	**1st CMOD Jump, mm**	**2nd CMOD Jump, mm**	F_0 **Slope, N/mm**	F_1 **Slope, N/mm**	F_2 **Slope, N/mm**
50 mm	13	0.0257		1319.07	333.05	
	14	0.0182	0.0105	1611.38	456.43	188.31
	20	0.0142		2827.44	686.03	
	21	0.0276		3686.37	382.51	
	23	0.0166		3366.80	668.99	
	24	0.0138	0.0238	6063.89	899.22	262.52
	27	0.0139		2255.32	821.01	
	29	0.0277		2396.31	784.93	
	30	0.0251		2899.41	863.03	
	31	0.0321		3099.61	423.76	
90 mm	26	-0.0029		2788.27	3342.33	
	32	0.01079		4773.83	1790.50	
	33	-0.0084		3363.05	2910.66	
	48	0.036		2519.22	613.91	
	50	0.00091		6696.91	7647.15	

surface [20]. Figure 4.3 shows a thin-section of the fracture surface from a 90 mm diameter sample after a short-rod plane strain fracture toughness test where the fracture propagates through the grain interior and along grain boundaries.



(a) Photo of the fracture surfaces of 90 mm Sample 31 which did not fracture with incremental crack growth.



(b) Photo of the fracture surfaces of 90 mm Sample 33 which fractured with incremental crack growth.

Figure 4.2: The fracture surfaces are highly reflective on both Sample 31 and 33, indicative of brittle, cleavage fracture. The brown streaks seen on each sample were left by the band saw blade when cutting the chevron into the samples.

4.2 Comparison of Laboratory-Manufactured Ice to Meteoric Ice

This work found that this laboratory-manufactured polycrystalline ice will fracture with lower K_{1c} values when compared to similar tests of meteoric ice [61]. This investigation found average K_{1c} to be 36.61 $\pm$ 11.24 kPa $m^{1/2}$ and 64.38 $\pm$ 15.30 kPa $m^{1/2}$ for -10°C and -20°C, respectively. Data from samples presented in this study fractured with a K_{1c} approximately 30 - 50% lower than meteoric ice tested in previous studies [16, 61, 62, 64]. Differences in the chevron sharpness, higher stress intensity loading rate, or differences intrinsic to the ice samples themselves could cause the observed discrepancy. Figure 4.4 shows K_{1c} from this study alongside data from Figure 5 of Rist et al., 2002 [62]. Rist et al., 2002 defined "stable" crack growth as multiple increments of quasi-stable crack growth [61]. All samples that fractured with at least one increment of crack growth have been classified as "quasi-stable" for this study. Table 4.4 shows the mean K_{1c} with standard deviations for the data presented herein. The relatively high standard deviations shown in Table 4.4, while

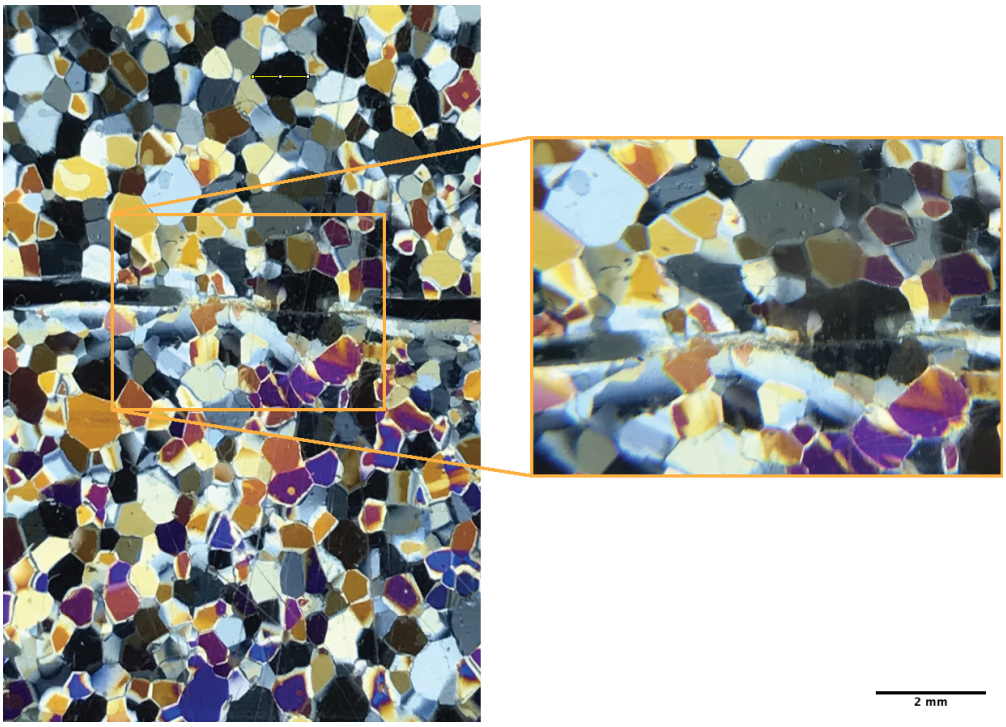


Figure 4.3: Cleavage type fracture imaged under cross-polarized light.

not insignificant, is comparable to values reported in the literature for K_{1c} of ice [16, 64].

Although the calculated values of K_{1c} are lower than reported from previous studies, the data at -20°C are close to the theoretical fracture toughness of ice, calculated from Equation 2.18. It is known that the toughness of a material is closely related to the energy required to create two new surfaces, and the K_{1c} of any material can be approximated with this method [64]. Surface energy, as described in Chapter 2, is proportional to the Elastic Modulus in plane-strain, E' (1.032e^7 kPa), and the interatomic spacing, a_1 (0.45 nm), with no apparent dependence on temperature [2]. From Equation 2.18, the approximate K_{1c} for polycrystalline ice is 69.24 kPa $m^{1/2}$. Comparing results presented in this study to the theoretical fracture toughness of ice, there is a difference of 47.13% at -10°C and 7.02% at -20°C. The small difference between theoretical K_{1c} and the measured K_{1c} in this work at -20°C shows that K_{1c} results from meteoric ice presented in previous studies could be experiencing strengthening mechanisms not present in the laboratory-manufactured polycrystalline ice tested in this study.

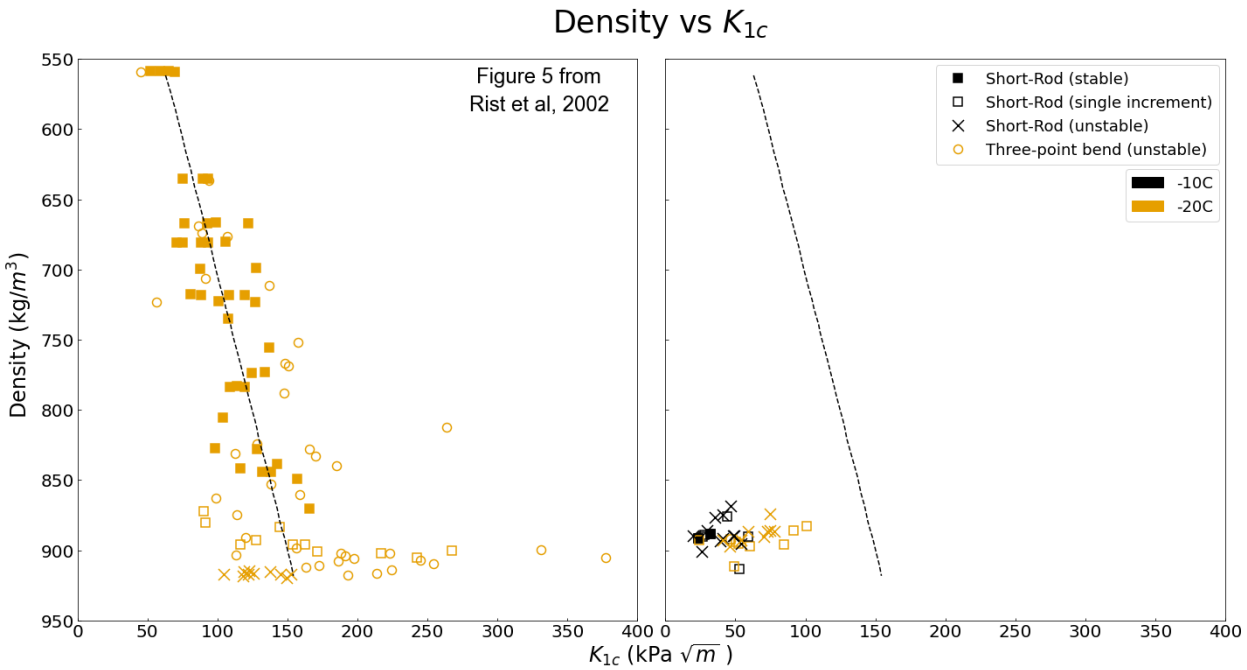


Figure 4.4: Data from Figure 5 of Rist et al., 2002 is on the left, data presented in this study is shown on the right [62]. The linear regression shown on the left is also displayed on the right to better show the quantitative similarities. Rist et al., 2002 defined "stable" crack growth as multiple increments of quasi-stable crack growth [61]. Solid squares in this plot represent short-rod samples that fractured with "stable" crack growth defined by Rist et al., 2002 [62]. Open squares represent short-rod samples that fractured with a single increment of crack growth prior to failure. Both the X and open circles represent unstable crack growth in short-rod and three-point bend tests, respectively. All tests from Rist et al., 2002 were performed at -20°C.

4.2.1 Strengthening Mechanisms

4.2.1.1 Grain Boundary Strengthening As discussed in Chapter 2, previous studies have different findings in support or rejection of grain boundary strengthening mechanisms in polycrystalline ice. The data presented here display a weak relationship between grain size and failure stress, σ_f. Figure 4.5 shows mean grain size$^{-1/2}$ vs σ_f for 50 mm and 90 mm samples at -10°C and -20°C. The low R^2 values shown in Figure 4.5 demonstrate that there is little evidence of grain boundary strengthening mechanisms in short-rod plane strain tests for polycrystalline ice. Rist et al., 2002 found no relationship between grain size and fracture toughness with grain sizes ranging from 1 - 9

Table 4.4: K_{1c}, K_{1d} and K_{1a} with standard deviations for 50 and 90 mm samples at -10°C and -20°C. For samples that showed two increments of crack growth, the higher load was used when calculating K_{1d} and K_{1a}.

Test Temp, °C	**Sample Size**	K_{1c}, **kPa m**$^{1/2}$	K_{1d}, **kPa m**$^{1/2}$	K_{1a}, **kPa m**$^{1/2}$
-10	50 mm	34.51 ± 10.49	21.40 ± 5.05	5.77 ± 2.69
	90 mm	38.71 ± 11.98	27.41 ± 13.76	24.50 ± 11.08
-20	50 mm	59.39 ± 13.16	50.99 ± 8.32	21.69 ± 7.64
	90 mm	69.37 ± 17.45	42.86 ± 28.71	34.29 ± 20.66

mm [62, 64]. While the grain size range for this work is smaller than the grain size range tested in Rist et al., 1999, 2002, a stronger relationship may exist for laboratory-manufactured polycrystalline ice over a larger range of grain sizes [61, 62].

4.2.1.2 Chemical Impurities Just as in metallic alloys, soluble and insoluble impurities can strengthen or weaken polycrystalline ice [14, 32, 33]. Hammonds et al., 2016 found that Ca^{++} ions increased the strength of polycrystalline ice at high strain rates and low temperatures. This study carried out tests at -10°C and -20°C and strain rates from 1x10^{-4} s^{-1} to 1x10^{-6} s^{-1} [32]. Additionally, Hammonds et al., 2018 found that H_2SO_4 ions caused faster creep rates in tension and lower peak stress values when compared to pure ice [33]. The strengthening mechanisms mentioned above will not be present in data from this study as the ice manufactured for this study was made with DI water, but these mechanisms are present when testing meteoric ice samples with those ions.

4.2.1.3 Elastic Anisotropy As glaciers and ice streams flow downhill, a preferred crystallographic orientation develops within the ice [64]. At higher strains, the textures within the ice become more pronounced and the ice becomes more anisotropic, giving the ice different material properties in different crystallographic directions [20]. If the fracture direction is aligned parallel to the preferred grain orientation of meteoric ice, it would result in higher fracture stresses than the

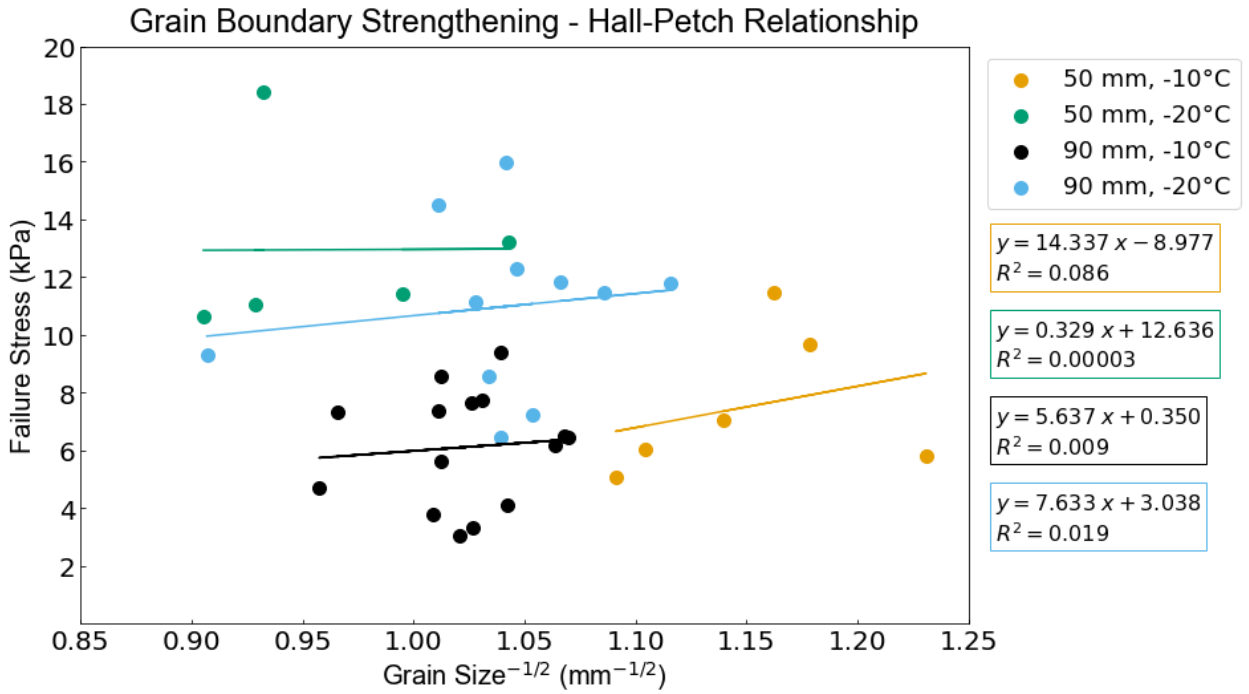


Figure 4.5: Failure stress of laboratory-manufactured polycrystalline ice vs grain size$^{-1/2}$ for 50 and 90 mm diameter samples at -10°C and -20°C.

other crystallographic directions [12]. By creating polycrystalline ice in the lab with equiaxed grains, this variable is not present in this study as no such anisotropy exists with equiaxed grains. Future work should test meteoric ice with a preferred grain orientation and compare those results to this study in order to quantify the anisotropy experienced by meteoric ice. Crevasses spread transversely across an ice sheet or glacier, so in order to truly constrain the K_{1d} and K_{1a} for large-scale ice sheet models, different tests with different crystalline orientations should be conducted.

4.2.1.4 Strain Hardening Discussed in Chapter 2, dislocations are the primary source of strain hardening in most materials, including polycrystalline ice [20, 64]. Dislocation density in ice is increased when the ice is subjected to a load, shown in Liu [45]. As reported by Sinha, the dislocation density in deformed polycrystalline ice ranges between 0.5 - 5 x10^7 cm^{-2}, measured by x-ray topography [66]. While the dislocation density of the laboratory-manufactured ice used in this study is not known, dislocation density of well-annealed ice has been measured at 10^2 cm^{-2}, 5

orders of magnitude lower than strained ice [64]. This large difference in dislocation density would cause a lower failure stress and by extension, a lower K_{1c}.

4.3 Crack Initiation and Crack Arrest Fracture Toughness

Crack arrest fracture toughness, K_{1a}, of laboratory-manufactured ice used in this investigation is approximately 25% of the K_{1c} for 50 mm samples and approximately 50% for 90 mm samples. Figure 4.6 shows the K_{1a} as a percentage of K_{1c} for a subset of four samples that showed stable and quasi-stable crack growth. This subset of samples were selected to display the different behavior seen from the samples. The top of Figure 4.6 shows Load vs Displacement for two of the ten 50 mm diameter samples that displayed quasi-stable crack growth behavior with their associated K_{1a} for each sample; the orange line shows a sample that displayed one increment of quasi-stable crack growth while the blue line shows two increments of stable crack growth prior to catastrophic failure. The ten 50 mm samples showed an average K_{1a} of 25.26% of K_{1c} with a standard deviation of $\pm$ 11.79% of K_{1c}. The bottom of Figure 4.6 shows Load vs Displacement for two of the five 90 mm samples that displayed quasi-stable crack growth behavior. The K_{1a} for these samples have a larger spread than the 50 mm samples, with an average of 50.60% of K_{1c} and a standard deviation of $\pm$ 24.94% of K_{1c}.

Seen in Figure 4.6, there is different behavior based on sample size. The 50 mm samples show the 'sawtooth' behavior where the displacement gauge measures crack opening as the crack propagates through the sample. The 90 mm samples show a decidedly different type of behavior where the displacement during crack growth is negative for a small interval, indicating crack closure.

In addition to calculating the K_{1c} and K_{1a}, the crack initiation fracture toughness, K_{1d}, was calculated for each sample. The 50 mm samples showed an average K_{1d} of 76.12% of K_{1c} while the average for 90 mm samples was 57.15%, shown in Table 4.6. One 50 mm sample catastrophically fractured at a load lower than the maximum crack initiation load, so the maximum K_{1d} found in this study is 101.3% of K_{1c} for one sample. Tables 4.5 and 4.6 show the maximum, minimum, and average K_{1a} and K_{1d} for each set of samples. Alongside these data are the number of samples tested

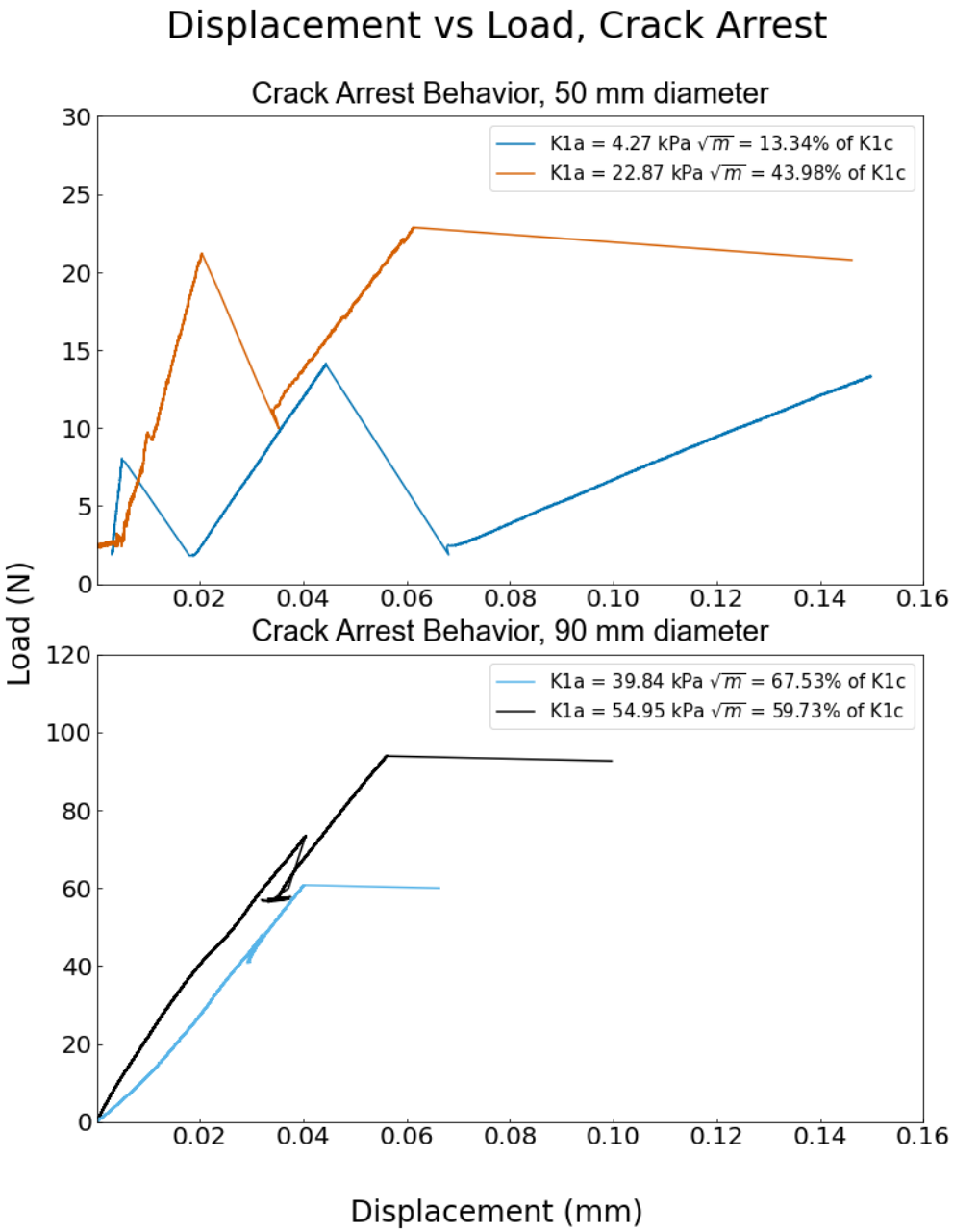


Figure 4.6: Load vs Displacement data with K_{1a} values for a subset of 50 mm and 90 mm diameter samples tested showing stable or quasi-stable crack growth behavior. Units for K_{1c} and K_{1a} are kPa $\sqrt{m}$. This subset was chosen as the two samples in each plot are representative of the different behavior seen during testing. On the top plot, for 50 mm samples, the orange line shows one increment of crack growth (quasi-stable) while the blue line shows two increments of crack growth (stable) prior to catastrophic failure. On the bottom plot, both the black and blue lines show one increment of crack growth behavior (quasi-stable).

and the Coefficient of Variation (CV) for each data set. The CV shows the variability of data in a sample in relation to the mean of the population. These tables show a high CV for each sample size, showing the large standard deviation in relation to the mean of the data.

Table 4.5: Crack Arrest Toughness, K_{1a}, as a percentage of K_{1c} for 50 and 90 mm samples that displayed either quasi-stable or stable crack growth behavior and Coefficient of Variation for these data.

Sample Size	**# of Samples**	**CV**	**Min** K_{1a} **%**	**Max** K_{1a} **%**	**Avg** K_{1a} **%**
50 mm	10	0.467	3.65%	43.60%	25.26%
90 mm	5	0.495	13.47%	81.97%	50.60%

Table 4.6: Crack Initiation Toughness, K_{1d}, as a percentage of K_{1c} for 50 and 90 mm samples that displayed either quasi-stable or stable crack growth behavior and Coefficient of Variation for these data.

Sample Size	**# of Samples**	**CV**	**Min** K_{1d} **%**	**Max** K_{1d} **%**	**Avg** K_{1d} **%**
50 mm	10	0.30	30.00%	101.3%	76.12%
90 mm	5	0.489	14.00%	82.38%	57.15%

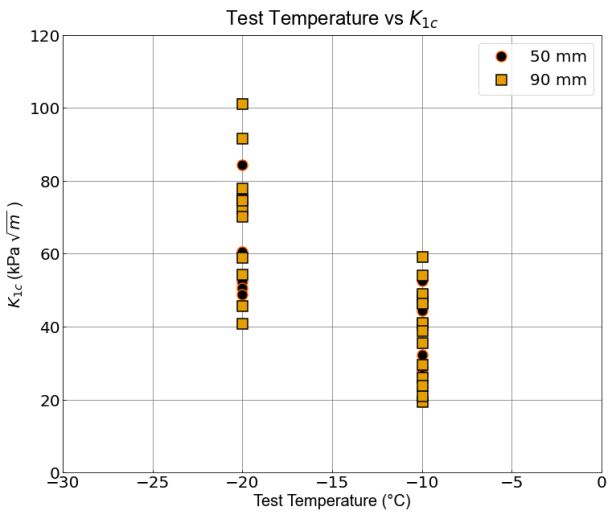
While Rist et al., 1999, 2002 were able to achieve "stable" crack growth, shown in Figure 4.4, all but six of the forty samples showing "stable" crack growth occurred within the firn cores. The samples showing single-increment or unstable crack growth for short rod tests are consolidated to the densities of ice (density higher than 840 $kg \cdot m^{-3}$), further showing the behavior of the results presented in this study match the behavior presented in previous work. The work performed by Rist et al, 2002 suggest that firn is capable of arresting cracks better than ice potentially due to the interconnected network of voids present in firn [62]. Firn has an average void size almost twice as large as the average void in ice [68]. Furthermore, it indicates that in order to accurately predict crevasse growth, a model would need to utilize a density-integrated model to predict how well the ice could arrest a propagating crevasse.

4.3.1 Dependence on Temperature and Density

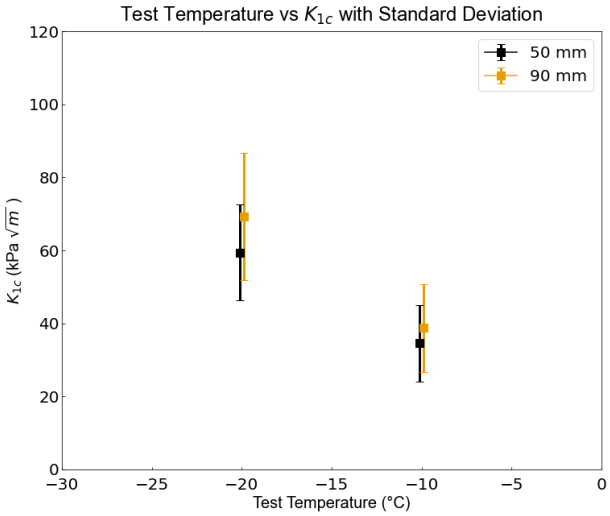
Earlier investigations have found the fracture toughness of polycrystalline ice to be dependent on both test temperature and density [64]. While there is considerable scatter in the data from previous studies, a linear relationship exists between temperature and K_{1c} between -2°C and -50°C with a regression coefficient, $r^2 = 0.22$ [64]. Although the relationship is weak, it does suggest that as temperature decreases, the K_{1c} should increase, if only slightly. A stronger relationship has been identified between fracture toughness and density. In studies that tested both firn and ice, such as Rist et al., 1999, the relationship is clearly identified, finding a 50 - 60% increase in K_{1c} as the porosity decreased from 40 to 0.05 % [61, 64].

4.3.1.1 Temperature As reported in many other studies, the results for K_{1c} from this study show a temperature dependence as displayed in Figure 4.7a. For the temperatures tested in this study, the mean K_{1c} at -20°C was 61% higher than the mean at -10°C. The temperature dependence seen in these data matches with data from meteoric ice cores, sea ice and columnar freshwater ice [64]. On a broader scale, a dependence of K_{1c} on test temperature means that as the Earth continues to warm, the fracture toughness of the remaining ice will decrease, potentially leading to increased crevasse propagation and calving rates. Additionally, a warmer Earth will also result in faster flowing ice, leading to increased fracture rates.

4.3.1.2 Density Figure 4.8 shows fracture toughness plotted against density for all data presented in this study. Figure 4.8 shows there is large scatter in the data, and little evidence of a trend between critical stress intensity factor and density. Shown in Figure 4.4, Rist et al., 2002 found a relationship between K_{1c} and density for short-rod samples, presented as a plotted linear regression [62]. A relationship between K_{1c} and density was not found in this investigation in part because the density was tightly controlled during the sample manufacturing process to to 898.43 ± 11.70 $kg \cdot m^{-3}$ for the 50 mm samples and 886.23 ± 8.48 $kg \cdot m^{-3}$ for the 90 mm samples. The range of densities in previous studies were much larger, from 550 $kg \cdot m^{-3}$ to 910 $kg \cdot m^{-3}$ from Rist et al., 1999, 2002 [61, 62]. With a larger range of densities, a relationship between density and K_{1c}



(a) This plot shows K_{1c} on the y-axis and test temperature on the x-axis for each individual sample.



(b) This plot shows the mean K_{1c} on the y-axis and test temperature on the x-axis with error bars indicating standard deviation.

Figure 4.7: Relationship between test temperature and the critical stress intensity factor. There is an increase in K_{1c} as the test temperature drops, consistent with other studies but not displayed here [61, 62, 64].

is expected.

In addition to plotting density, porosity is plotted on a second y-axis in Figure 4.8. Using the density values calculated for each sample and the the theoretical maximum density of polycrystalline ice, 916.8 kg/m^3, the porosity of each sample ranged from 0.38% to 5.27% with an average value of 2.96% with little impact on the K_{1c} as porosity increases. While this study did not find a relationship between density and K_{1c}, results from previous studies demonstrate a correlation between density and K_{1c}, especially when testing the fracture toughness of firn and ice [61, 62, 64]. As mentioned above, a robust crevasse model would incorporate a depth-integrated fracture toughness to account for the change in K_{1c} with depth as well as behavior that trends towards unstable crack growth with increasing depth.

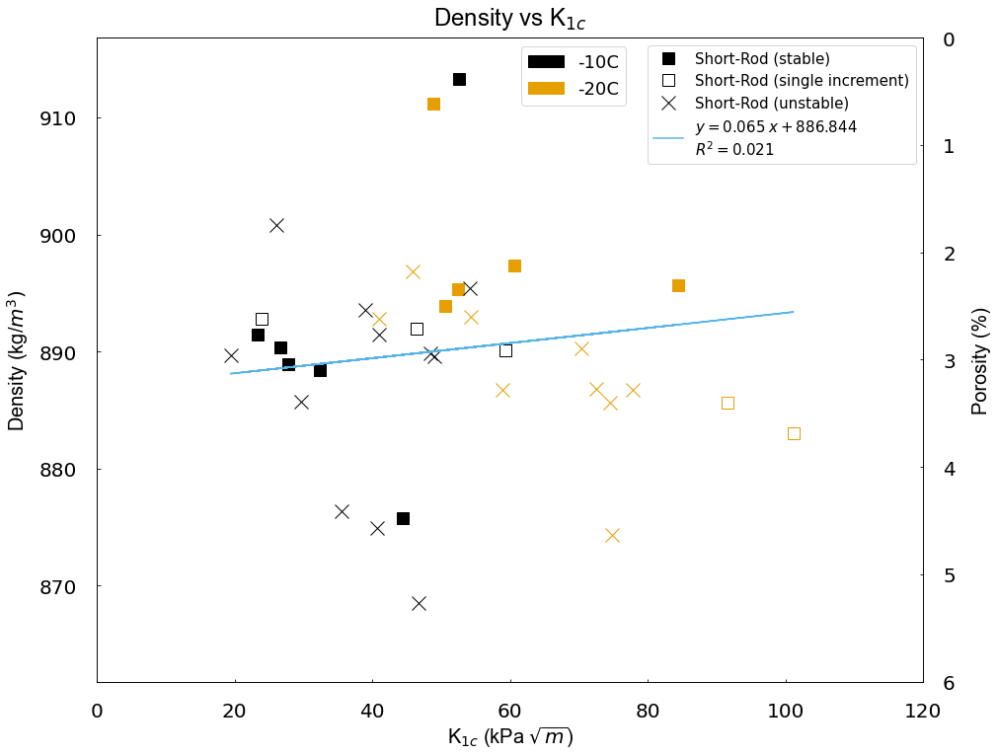


Figure 4.8: Critical stress intensity factor for laboratory-manufactured polycrystalline ice samples vs density for each sample. The linear regression shows a weak relationship between density and K_{1c}.

4.4 Critical Stress Intensity Loading Rate

As described in Chapter 2, the critical stress intensity loading rate, $\dot{K}_1^*$, should be between 0.3 - 10 kPa $m^{1/2}$ s^{-1} for test temperatures of -10 to -20°C in order to ensure that samples fracture in plane strain with no crack-tip creep during testing [65]. Critical stress intensity loading rates for this study range from 0.127 - 1.469 kPa $m^{1/2}$ s^{-1} with an average of 0.427 kPa $m^{1/2}$ s^{-1}. Comparing results from this study to the reported necessary values for $\dot{K}_1^*$ show that all of the tests for the 90 mm samples fall below the minimum $\dot{K}_1^*$ for plane-strain and could be experiencing crack-tip creep [54]. Figure 4.9 shows a histogram of $\dot{K}_1^*$ for each sample. All but two of the 50 mm samples showed a higher $\dot{K}_1^*$ than the minimum required to ensure plane-strain. Of the 50 mm samples tested, all but one sample, Sample 28, experienced stable or quasi-stable crack growth prior to

fracture. Sample 28 also had the lowest $\dot{K}_1^*$ of all 50 mm samples, indicating that $\dot{K}_1^*$ could also influence whether or not a sample will fracture with incremental crack growth. This study tested thirty-four 90 mm samples, only five of which broke with incremental crack growth. The $\dot{K}_1^*$ values for the five 90 mm diameter samples that fractured with incremental crack growth were in the top 50% of the $\dot{K}_1^*$ range for 90 mm samples. In order to apply these results to an ice sheet model, it is necessary to ensure the tests occur within plane-strain. As the 90 mm samples did not fracture in plane-strain, these results should be excluded from model application until data can be collected within the correct range for critical stress intensity loading rate. This investigation used a single displacement rate in order to eliminate variability from the MTS load frame. This resulted in the critical stress intensity loading rates for the 90 mm samples being below the threshold necessary to achieve plane strain fracture. In order to ensure plane strain fracture events in all samples, future work should perform fracture tests at higher displacement rates.

4.5 Strain Energy Density

This study also analyzed the total strain energy of laboratory-manufactured polycrystalline ice, described in Chapter 2. Strain energy density of each fracture test was determined by calculating the area under the Load vs Displacement curve for each sample and dividing the result of the integral by the sample volume. Figure 4.10 shows a strong relationship between strain energy density (U^*) in the body and σ_f^2. A linear relationship between these quantities is predicted by Equation 2.8 where strain energy, U, is linearly related to σ_f^2. Figure 4.10 shows that Griffith's equation for strain energy correlates well to laboratory-manufactured polycrystalline ice. Equation 2.8 is only valid when a brittle material fractures in the LEFM regime, showing conclusively that LEFM applies to the polycrystalline ice samples tested in this investigation.

4.6 Chevron Geometry

While nine out of ten 50 mm diameter samples broke in a stick-slip manner, incremental crack growth in 90 mm samples was difficult to achieve. Of the thirty-four 90 mm samples tested

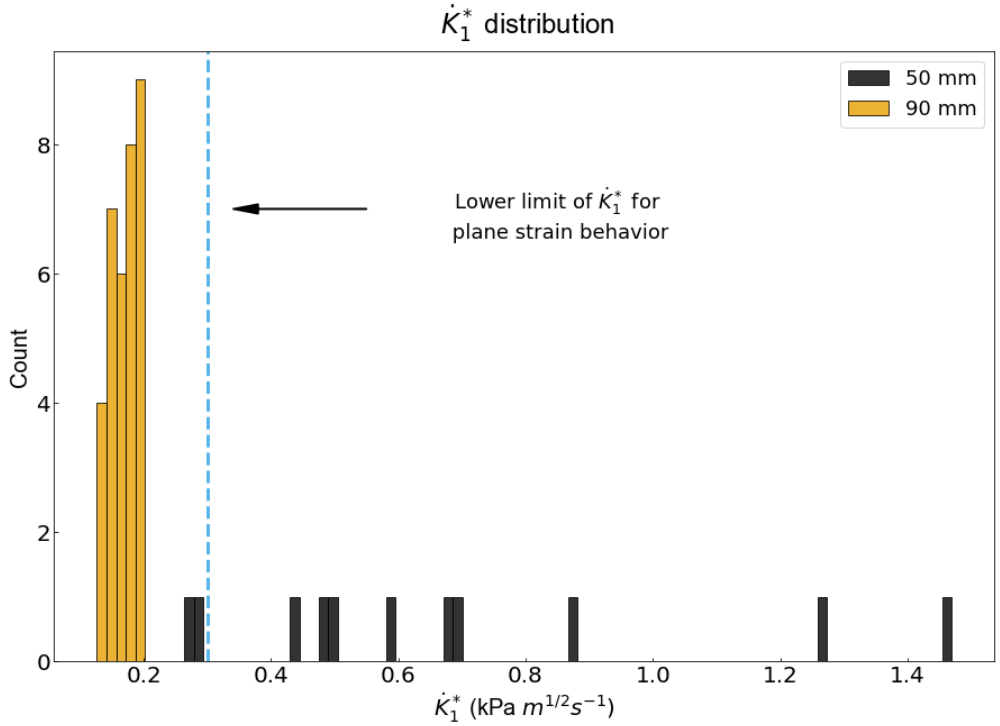


Figure 4.9: Distribution of the critical stress intensity loading rate, $\dot{K}_1^*$ for each sample. Each bin is 0.022 kPa $m^{1/2}s^{-1}$ wide. None of the 90 mm samples meet the minimum critical crack tip growth rate defined by Schulson and Duval [64].

in this study, twenty-nine failed catastrophically, with no incremental crack growth. One possible controlling function of incremental crack growth could be the relationship of the chevron area:sample width. As discussed in Chapter 3, the chevron geometry was modified in an attempt to get the 90 mm samples to fracture with incremental crack growth. After modifying the chevron saw fixture to hold the chevron area:sample width ratio constant, incremental crack growth in the 90 mm samples was not achieved. In fact, after modifying the chevron geometry, the samples began to fracture at much lower loads than with the previous sample geometry. This could be due to shorter crack path before catastrophic failure.

An unintended consequence of modifying the chevron geometry was that the data collected from those samples could not use the same value for Y_m^* to calculate K_{1c}. A new Y_m^* was determined for the new geometry by using the average value for K_{1c} from Equation 2.20 of all the samples at

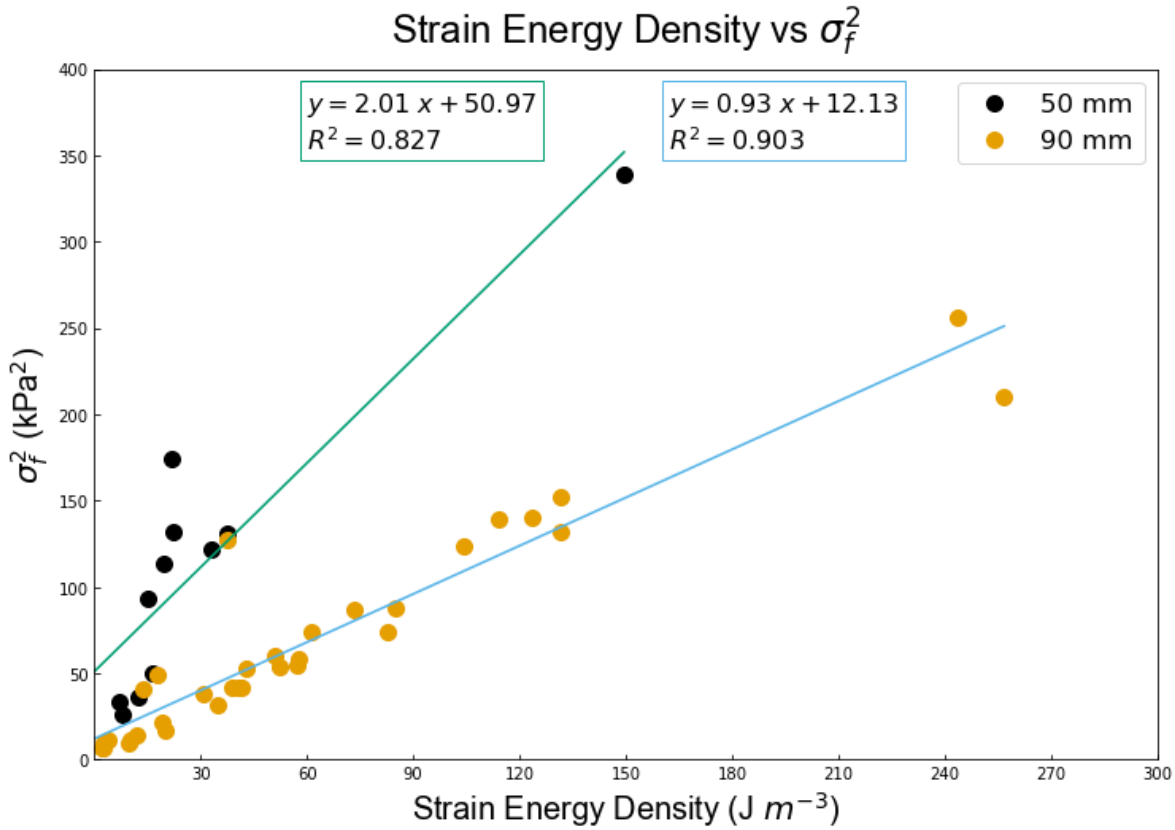


Figure 4.10: Equation 2.6 predicts a linear relationship between Strain Energy Density (U^*) and σ_f^2 [30]. A distinct relationship between U^* and σ_f^2 with the data presented in this study is seen here.

each temperature. Calculating a new Y_m^* for each of the samples with a modified chevron yielded value of 63.69 vs 36.25 from ASTM E 1304-97 [4]. This new Y_m^* value was then used to calculate K_{1c} for each sample with modified chevron geometry. While this is a different method to determine Y_m^* than described in Chapter 2, the method described above is a reasonable approximation in order to use the results from the samples with modified geometry. This method would be better performed on a material other than polycrystalline ice with a well-known K_{1c} value.

4.7 Sources of Error

There is appreciable spread in the data, which could be due a number of factors. When comparing data from this study to other studies of similar nature, it is necessary to identify the variations in K_{1c} from this study to those of meteoric ice. On average, data from this study show an average K_{1c} approximately 30% lower than from studies that used meteoric ice cores [61, 62, 64]. This discrepancy in fracture toughness results can be attributed to a variety of factors described below, including the critical stress intensity loading rate, ice porosity, chemical impurities, elastic anisotropy, and strain hardening of meteoric ice.

4.7.1 Critical Stress Intensity Loading Rate

The lower critical stress intensity loading rates experienced in this study could explain why many of the 90 mm diameter samples did not fracture with incremental crack growth. The low end of the range provided for the critical stress intensity loading rates by Schulson and Duval (0.3 - 10 kPa $m^{1/2}$ s^{-1}), falls slightly higher than the maximum of the critical stress intensity loading rate calculated for the 90 mm diameter samples, with a maximum of 0.206 kPa $m^{1/2}$ s^{-1}. Under these conditions, a portion of the strain energy is used to plastically deform the ice instead of all the energy being applied to the creation of new surfaces [64]. Additionally, none of the 90 mm samples fractured in true plane-strain as intended by the study. Finally, the low value for the critical stress intensity loading rate could explain why only five of thirty-four 90 mm samples fractured with incremental crack growth, whereas all but one of the 50 mm samples fractured with stable or quasi-stable crack growth. Only two 50 mm samples had a critical stress intensity loading rate below the low end of the acceptable range, one of which did not fracture with incremental crack growth. All other 50 mm samples had a critical crack-tip load rate higher than 0.3 kPa $m^{1/2}$ s^{-1} and achieved stable or quasi-stable crack growth.

4.7.2 Ice Porosity

Another factor that may explain why the samples showed a lower K_{1c} than meteoric ice could be from porosity-embrittlement. While the procedure from Cole, 1979 [17] was followed, bubble-free ice was never created in this study. As described in *Creep and Fracture of Ice*, porosity within the ice samples can cause reduced stiffness during fracture testing [64]. With the porosity in the ice samples tested in this study ranging from 0.4 - 5%, a decrease in strength and K_{1c} due to the bubble concentration within the ice is expected. Porosity-based embrittlement has been observed in other studies, although with a larger range of porosities than presented here [61, 64]. Previous studies have determined the average bubble radius in meteoric ice to be 100 μm [68]. Although the diameter of the crack tip from this study was not directly measured, it is reasonable to assume the crack tip diameter is larger than 100 μm when cutting with a band saw. While Figure 4.8 does not show a dependence on K_{1c} with increasing porosity, a bubble with a diameter smaller than the chevron tip in the direct vicinity of the crack tip would cause a higher stress concentration which would cause fracture at a lower load.

4.7.3 Test Alignment

Lining up the samples within the MTS load frame proved to be a non-trivial task, thus machine misalignment could introduce an unexpected source of error. If the samples were aligned off-parallel from the crosshead of the load frame, unintended shear stresses could be introduced and cause a mixed-mode loading scheme and thus the K_{1c} calculated for that sample would be incorrect. Alignment could be improved with a relatively simple addition, like a plumb line, however a better fix would be a diameter dependent fixture that holds the sample perfectly vertical until the crosshead has been lowered into place.

4.7.4 Chevron Sharpness

While the chevron in each sample was prepared using the same saw and the same technique, the sharpness of the chevron could be another variable. Samples from Rist et al., 1999 were machined on a lathe and the chevron was sharpened with a histological microtome style chisel blade, producing

a sharper chevron than a saw blade [61].

4.8 Proposed Improvements and Applications for Future Work

While this study presents some findings that have not been reported on previously, there are several things that could be done to improve the work shown here. Firstly, there are some improvements that could be implemented to the sample creation process that would reduce the porosity and cloudiness of the samples, while maintaining the polycrystalline nature of the samples with equiaxed grains and a random crystal orientation. Additionally, to increase the validity of the results presented in this study, additional data should be collected both at lower and higher temperatures and at higher crosshead displacement rates. Further analysis of three- and four-point bend tests should be completed in order to compare K_{1c} results between test types. Finally, testing meteoric ice cores alongside laboratory-manufactured ice samples would provide a good basis for comparison of the anisotropy present in meteoric ice due to glacier flow.

4.8.1 Sample Creation

Despite following the procedure for sample creation described in Cole (1979), sample quality in this study was poorer than described by Cole [17]. This could be due to several factors. First, the freezing rate could be too fast for the dissolved and entrained gasses to escape the seed grain compact prior to being frozen into place. Correcting this would require a reduced temperature gradient applied to the mold which would allow the slurry to take more time to freeze.

Finally, future work should test the impact that the seed grains have on the bubble concentration in a sample. As described in Chapter 3, prior to creating any sample, the mold is packed with sieved seed grains in order to ensure a random grain orientation and a relative final grain size. Anecdotally, it was found that seed grain compaction and relative "freshness" impacted the final bubble concentration in the ice sample. By compacting the seed grains more, the pore spaces between the seed grains shrinks, making it more difficult for the air occupying those pore spaces to escape when the mold is flooded with de-gassed water at the start of the freezing process.

4.8.2 Test Types

By conducting fracture toughness testing using a test type that lends itself to determining the K_{1d} and K_{1a}, it was possible to determine those values for the first time in laboratory-manufactured polycrystalline ice, however, this study was also limited in that there is no other data from laboratory-manufactured ice samples to compare results. Conducting additional tests using three- and four-point bend tests would not provide additional K_{1d} and K_{1a} results, but it would provide validation of the K_{1c} results. As it stands, the only comparison of these data can be made with results from meteoric and columnar ice.

CHAPTER FIVE

CONCLUSIONS

In part, this study aimed to identify the crack arrest fracture toughness of polycrystalline ice using a short-rod plane strain fracture toughness test on laboratory-manufactured ice in order to better inform crevasse depth estimates within ice-sheet models. Based on the analysis performed in Chapter 4, it is shown that laboratory-manufactured polycrystalline ice is capable of fracturing with stable and quasi-stable crack growth and these data can be used to calculate the crack arrest fracture toughness of polycrystalline ice. The results indicate that the crack arrest fracture toughness of polycrystalline ice is between 25 - 50% of K_{1c}. As found in other studies, there is a correlation of K_{1c} with temperature, although due a small range of densities tested in this study, there was not adequate data to establish whether or not a correlation exists between K_{1c} and sample density.

In addition to determining the crack arrest fracture toughness of polycrystalline ice, this investigation aimed to determine how the plane strain fracture toughness of laboratory-manufactured ice compared to that of meteoric ice. The calculated K_{1c} values of 38.32 $\pm$ 11.21 kPa $m^{1/2}$ and 61.29 $\pm$ 18.32 kPa $m^{1/2}$ for -10°C and -20°C, respectively, are lower than reported in past studies by approximately 50% at -10°C and 30% at -20°C [16, 62, 64]. As discussed in Chapter 4, the drop in K_{1c} seen in these data can be accounted for by factors present in meteoric ice, but not present herein due to the equiaxed microstructure of the laboratory-manufactured samples.

Incorporating the data presented in this study into ice sheet models would increase the estimated crevasse depths produced by these models. Current models estimate that crevasses will penetrate the ice sheet until the stress intensity factor at the crack tip drops below the crack initiation fracture toughness. While models currently overestimate crevasse depths, direct measurements of crevasse depths are difficult to acquire and are subject to systematic under-measurement [52]. With the data presented herein, it is shown that the crack initiation and crack arrest fracture toughness values for polycrystalline ice vary such that using the crack initiation toughness as the sole criteria for crack arrest in polycrystalline ice is an oversimplification when

modeling this phenomenon. In addition, a robust model of crevasse initiation and arrest needs to be integrated with respect to density in order to account for variations in crack arrest capabilities of firn and ice. Due to the low critical stress intensity loading rate, discussed in Chapter 4, the 90 mm diameter samples did not fracture in true plane-strain and should be excluded from further ice sheet model development until additional testing at higher critical stress intensity loading rates is completed. Finally, future work should also attempt to reconcile the differences in fracture toughness between meteoric ice and laboratory-manufactured ice due to strengthening mechanisms in meteoric ice.

This work shows that laboratory-manufactured polycrystalline ice follows the Griffith Theory of Brittle Fracture at high strain rates (10^{-6} s^{-1}). In addition, this study is the first to show laboratory-manufactured polycrystalline ice will fracture with stable and quasi-stable crack growth when loaded in plane-strain with short-rod geometry. Finally, this study quantifies the crack initiation and crack arrest fracture toughness for polycrystalline ice and suggests it should be added to ice sheet models to improve crevasse propagation predictions. Adding these two fracture toughness parameters to crevasse depth models will allow the models to more accurately represent the stress intensity at the crack tip during crack initiation and arrest. All of these results show that laboratory-manufactured polycrystalline ice is a viable alternative to collecting in-situ meteoric ice for studying crevasse initiation and propagation.

REFERENCES CITED

[1] *Symposium on Fatigue and Fracture of Metals at Massachusetts Institute of Technology*. John Wiley and Sons, Inc, 1952.

[2] M. F. Ashby. Materials selection in conceptual design. *Materials Science and Technology*, 5(6):517–525, 1989.

[3] ASTM International. Standard Test Methods for Determining Average Grain Size. *Astm E112-10*, pages 1–27, 2010.

[4] ASTM International. Standard Test Method for Plane-Strain (Chevron-Notch) Fracture Toughness of Metallic Materials. 2020.

[5] Zdeněk P. Bažant and J. Planas. *Fracture and Size Effect in Concrete and Other Quasibrittle Materials*. CRC Press, 1998.

[6] Douglas I. Benn, Tom Cowton, Joe Todd, and Adrian Luckman. Glacier calving in greenland. *Current Climate Change Reports*, 3(4):282–290, 2017.

[7] Douglas I. Benn, Charles R. Warren, and Ruth H. Mottram. Calving processes and the dynamics of calving glaciers. *Earth-Science Reviews*, 82(3-4):143–179, 2007.

[8] Heinz Blatter. Velocity and stress fields in grounded glaciers: a simple algorithm for including deviatoric stress gradients. *Journal of Glaciology*, 41(138):333–344, 1995.

[9] Chris Borstad, A. Khazendar, E. Larour, M. Morlighem, E. Rignot, M. P. Schodlok, and H. Seroussi. A damage mechanics assessment of the Larsen B ice shelf prior to collapse: Toward a physically-based calving law, 2012.

[10] Chris Borstad, A. Khazendar, Bernd Scheuchl, Mathieu Morlighem, Eric Larour, and Eric Rignot. A constitutive framework for predicting weakening and reduced buttressing of ice shelves based on observations of the progressive deterioration of the remnant Larsen B Ice Shelf. *Geophysical Research Letters*, 43(5):2027–2035, 2016.

[11] Chris Borstad, E. Rignot, J. Mouginot, and M. P. Schodlok. Creep deformation and buttressing capacity of damaged ice shelves: theory and application to Larsen C ice shelf. *The Cryosphere*, 7(6):1931–1947, dec 2013.

[12] David Broek. *Elementary Engineering Fracture Mechanics*. Springer Netherlands, 1982.

[13] Ed Bueler and Jed Brown. Shallow shelf approximation as a "sliding law" in a thermomechanically coupled ice sheet model. *Journal of Geophysical Research*, 114(F3):F03008, jul 2009.

[14] F C Campbell, editor. *Elements of Metallurgy and Engineering Alloys*. ASM International, Jun 2008.

[15] Pinqiang Cao, Jianyang Wu, Zhisen Zhang, Bin Fang, Li Peng, Tianshu Li, Thijs J.H. Vlugt, and Fulong Ning. Mechanical properties of bi- and poly-crystalline ice. *AIP Advances*, 8(12), 2018.

[16] J. Christmann, R. Müller, K. G. Webber, D. Isaia, F. H. Schader, S. Kipfstuhl, J. Freitag, and A. Humbert. Measurement of the fracture toughness of polycrystalline bubbly ice from an Antarctic ice core. *Earth System Science Data*, 7(1):87–92, 2015.

[17] David M. Cole. Preparation of polycrystalline ice specimens for laboratory experiments. *Cold Regions Science and Technology*, 1(2):153–159, 1979.

[18] Bethan Davies. A introduction to the hierarchy of ice-sheet models, 2015.

[19] M. A. Depoorter, J. L. Bamber, J. A. Griggs, J. T. M. Lenaerts, S. R. M. Ligtenberg, M. R. van den Broeke, and G. Moholdt. Calving fluxes and basal melt rates of antarctic ice shelves. *Nature*, 502(7469):89–92, 2013.

[20] George E. Dieter. *Mechanical Metallurgy*. McGraw-Hill Book Company, 1986.

[21] T Dunse, T Schellenberger, J O Hagen, A Kääb, T V Schuler, and C H Reijmer. Glacier-surge mechanisms promoted by a hydro-thermodynamic feedback to summer melt. *The Cryosphere*, 9:197–215, 2015.

[22] Veronika Emetc, Paul Tregoning, Mathieu Morlighem, Chris Borstad, and Malcolm Sambridge. A statistical fracture model for Antarctic ice shelves and glaciers. *The Cryosphere*, 12(10):3187–3213, oct 2018.

[23] Zhongyun Fan. The grain size dependence of ductile fracture toughness of polycrystalline metals and alloys. *Materials Science and Engineering A*, 191(1-2):73–83, 1995.

[24] GEOKON. *Nold DeAerator: Model 2100*. GEOKON, Lebanon, NH, USA, January 2019. [Online].

[25] Peter H. Gleick. *Water in Crisis: A Guide to the World's Fresh Water Resources*. New York: Oxford University Press, 1993.

[26] J.W. Glen. The creep of polycrystalline ice. *Cold Regions Science and Technology*, 11(3):285–300, 1955.

[27] D. L. Goldsby and D. L. Kohlstedt. Superplastic deformation of ice: Experimental observations. *Journal of Geophysical Research: Solid Earth*, 106(B6):11017–11030, 2001.

[28] Ralf Greve. A continuum–mechanical formulation for shallow polythermal ice sheets. *Philosophical Transactions of the Royal Society of London. Series A: Mathematical, Physical and Engineering Sciences*, 355(1726):921–974, may 1997.

[29] Ralf Greve and Kolumban Hutter. Polythermal three-dimensional modelling of the Greenland ice sheet with varied geothermal heat flux. *Annals of Glaciology*, 21:8–12, 1995.

[30] A.A. Griffith. The Phenomena of Rupture and Flow in Solids. *Philosophical Transactions of the Royal Society of London. Series A, Containing Papers of a Mathematical or Physical Character*, 221:163–198, 1920.

[31] E. O. Hall. The Deformation and Ageing of Mild Steel: III Discussion of Results. *Proceedings of the Physical Society B*, 64(9):747–753, sep 1951.

[32] Kevin Hammonds and Ian Baker. The effects of Ca++ on the strength of polycrystalline ice. *Journal of Glaciology*, 62(235):954–962, 2016.

[33] Kevin Hammonds and Ian Baker. The Effects of H2SO4 on the Mechanical Behavior and Microstructural Evolution of Polycrystalline Ice. *Journal of Geophysical Research: Earth Surface*, 123(3):535–556, 2018.

[34] K Hutter. *Theoretical Glaciology*. Springer Netherlands, 1983.

[35] G. R. Irwin. Analysis of stresses and strains near the end of a crack traversing a plate. *Journal of Applied Mechanics*, 24:361–364, 1957.

[36] George R. Irwin. *Fracture*. Springer Berlin Heidelberg, Berlin, Heidelberg, 1958.

[37] D. Jenssen. A three-dimensional polar ice-sheet model. *Journal of Glaciology*, 18(80):373–389, 1977.

[38] Wilhelm Kirch, editor. *Pearson's Correlation Coefficient*, pages 1090–1091. Springer Netherlands, Dordrecht, 2008.

[39] Robert M. Krimmel and Mark F. Meier. Glaciers and glaciology of alaska: Anchorage to juneau, alaska july 21–29, 1989, volume 301. *American Geophysical Union*, 301:1–61, 1989.

[40] J. Krug, J. Weiss, O. Gagliardini, and G. Durand. Combining damage and fracture mechanics to model calving. *The Cryosphere*, 8(6):2101–2117, nov 2014.

[41] E. Larour, H. Seroussi, M. Morlighem, and E. Rignot. Continental scale, high order, high spatial resolution, ice sheet modeling using the Ice Sheet System Model (ISSM). *Journal of Geophysical Research: Earth Surface*, 117(F1), mar 2012.

[42] Pauli Lehto, Jani Romanoff, Heikki Remes, and Teemu Sarikka. Characterisation of local grain size variation of welded structural steel. *Welding in the World*, 60(4):673–688, 2016.

[43] Puali Lehto, Heikki Remes, Tapio Saukkonen, Hannu Hänninen, and Jani Romanoff. Influence of grain size distribution on the hall–petch relationship of welded structural steel, 2014.

[44] William H. Lipscomb, Jeremy G. Fyke, Miren Vizcaíno, William J. Sacks, Jon Wolfe, Mariana Vertenstein, Anthony Craig, Erik Kluzek, and David M. Lawrence. Implementation and Initial Evaluation of the Glimmer Community Ice Sheet Model in the Community Earth System Model. *Journal of Climate*, 26(19):7352–7371, oct 2013.

[45] Fuping Liu, Ian Baker, and Michael Dudley. Dislocation-grain boundary interactions in ice crystals. *Philosophical Magazine A: Physics of Condensed Matter, Structure, Defects and Mechanical Properties*, 71(1):15–42, 1995.

[46] M. W. Mahaffy. A three-dimensional numerical model of ice sheets: Tests on the barnes ice cap, northwest territories. *Journal of Geophysical Research (1896-1977)*, 81(6):1059–1066, 1976.

[47] Shawn J. Marshall. *The Cryosphere*. Princeton University Press, 2011.

[48] Total Materia. Linear elastic fracture mechanics: Part one, 2018.

[49] J.C. Maxwell. On the Dynamical Theory of Gases. *Royal Society of London*, 157:49–88, 1867.

[50] Bob McGinty. Fracture mechanics, 2020.

[51] I. Milne, R.O. Ritchie, and B. Karihaloo. *2.05 Dynamic Fracture*. Elsevier, 2003.

[52] Ruth Mottram and Douglas Benn. Testing crevasse-depth models: a field study at breiðamerkurjökull, iceland. *Journal of Glaciology*, 55:746–752, 09 2009.

[53] Sneha N. Naik and Stephen M. Walley. The hall–petch and inverse hall–petch relations and the hardness of nanocrystalline metals. *Journal of Materials Science*, 55(7):2661–2681, 2020.

[54] W. A. Nixon and E. M. Schulson. A micromechanical view of the fracture toughness of ice. *J. Phys. Colloques*, 48(3), 1987.

[55] J.F. Nye. The flow of glaciers and ice-sheets as a problem in plasticity. *Proceedings of the Royal Society of London. Series A. Mathematical and Physical Sciences*, 207(1091):554–572, 1951.

[56] E. Orowan. *Dislocation and mechanical properties*. American Institute of Mining and Metallurgical Engineers, 1954.

[57] N.J. Petch. The cleavage strength of polycrystals. *Journal of the Iron and Steel Institute*, 174(5):25–28, 1953.

[58] Thomas Phillips, Harihar Rajaram, and Konrad Steffen. Cryo-hydrologic warming: A potential mechanism for rapid thermal response of ice sheets. *Geophysical Research Letters*, 37(20):1–5, 2010.

[59] Evgeny A. Podolskiy and Fabian Walter. Cryoseismology. *Reviews of Geophysics*, 54(4):708–758, 2016.

[60] K. Ravi-Chandar and W. G. Knauss. An experimental investigation into dynamic fracture: I. crack initiation and arrest. *International Journal of Fracture*, 25(4):247–262, 1984.

[61] M. A. Rist, P. R. Sammonds, S. A. F. Murrell, P. G. Meredith, C. S. M. Doake, H. Oerter, and K. Matsuki. Experimental and theoretical fracture mechanics applied to Antarctic ice fracture and surface crevassing. *Journal of Geophysical Research: Solid Earth*, 104(B2):2973–2987, feb 1999.

[62] M. A. Rist, P. R. Sammonds, H. Oerter, and C. S. M. Doake. Fracture of Antarctic shelf ice. *Journal of Geophysical Research: Solid Earth*, 107(B1):ECV 2–1–ECV 2–13, 2002.

[63] C. Schoof. Ice-sheet acceleration driven by melt supply variability. *Nature*, 468:803–806, 2010.

[64] E.M. Schulson and P. Duval. *Creep and Fracture of Ice*. Cambridge University Press, 2009.

[65] Erland M. Schulson. The Structure and Mechanical Behavior of Ice. *JOM*, 51(2):21–27, 1999.

[66] N. K. Sinha. Observation of basal dislocations in ice by etching and replicating. *Journal of Glaciology*, 21(85):385–395, 1978.

[67] S. Timoshenko and J.N. Goodier. *Theory of Elasticity*. McGraw-Hill Book Company, Inc, New York, 2nd edition, 1951.

[68] Kai J. Ueltzhöffer, Verena Bendel, Johannes Freitag, Sepp Kipfstuhl, Dietmar Wagenbach, Sérgio H. Faria, and Christoph S. Garbe. Distribution of air bubbles in the edml and edc (antarctica) ice cores, using a new method of automatic image analysis. *Journal of Glaciology*, 56(196):339–348, 2010.

[69] C.J. van der Veen. Fracture mechanics approach to penetration of surface crevasses on glaciers. *Cold Regions Science and Technology*, 27(1):31–47, 1998.

[70] Tom Watson, Mitchell Jolles, Paul Peyser, and Sheldon Mostovoy. An evaluation of the short rod technique to measure the fracture toughness of polymers. *Journal of Materials Science*, 22(4):1249–1258, 1987.

[71] H.M. Westergaard. Bearing Pressures and Cracks. *Journal of Applied Mechanics*, 49(1):4953, 1939.

[72] R Winkelmann, M A Martin, M Haseloff, T Albrecht, E Bueler, C Khroulev, and A Levermann. The Potsdam Parallel Ice Sheet Model (PISM-PIK)-Part 1: Model description. *The Cryosphere*, 5:715–726, 2011.

APPENDICES

APPENDIX A

DRAWINGS FOR SAW AND TEST FIXTURES

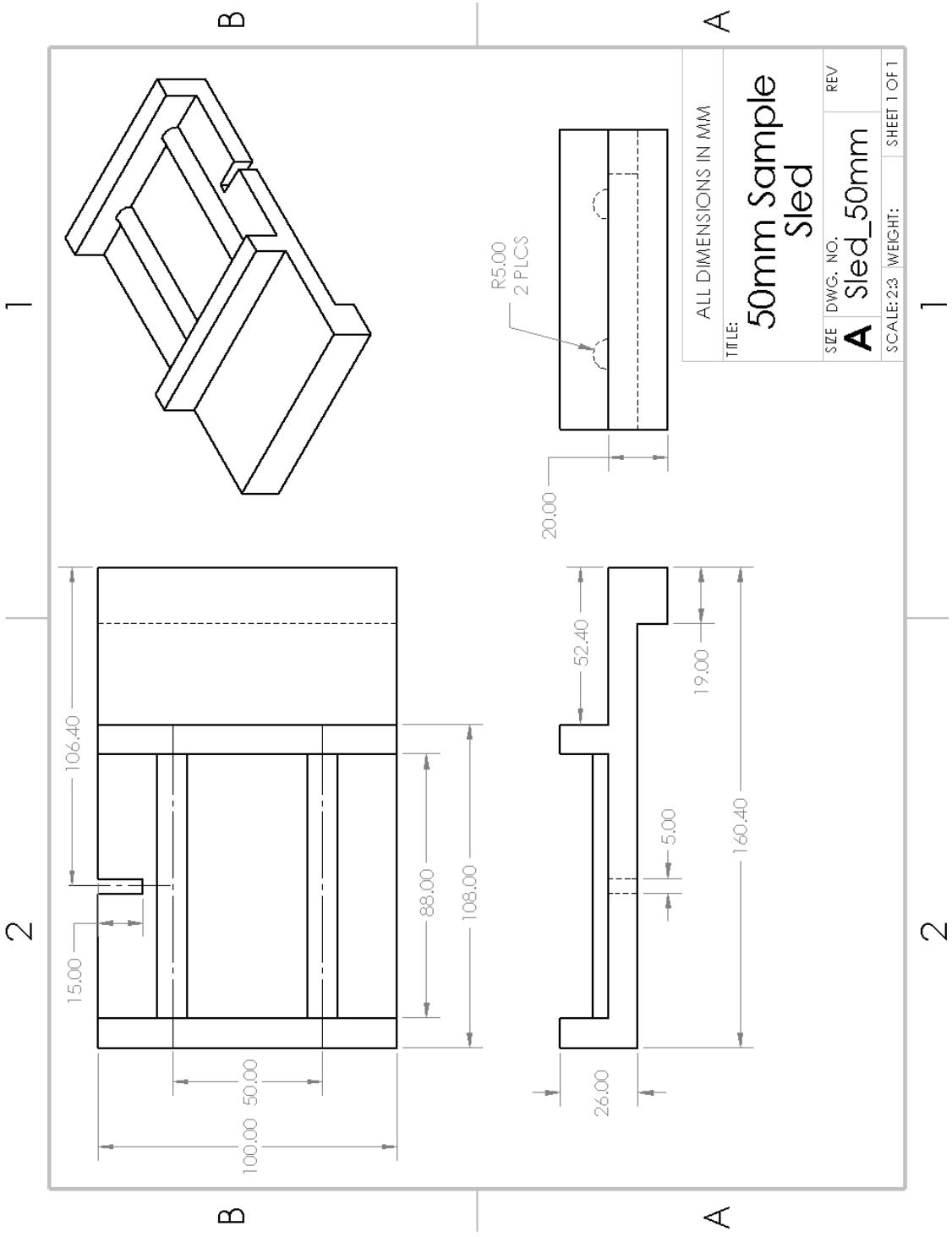


Figure A.1: SolidWorks drawing of the sled used to locate the 50 mm sample fixtures on the band saw table.

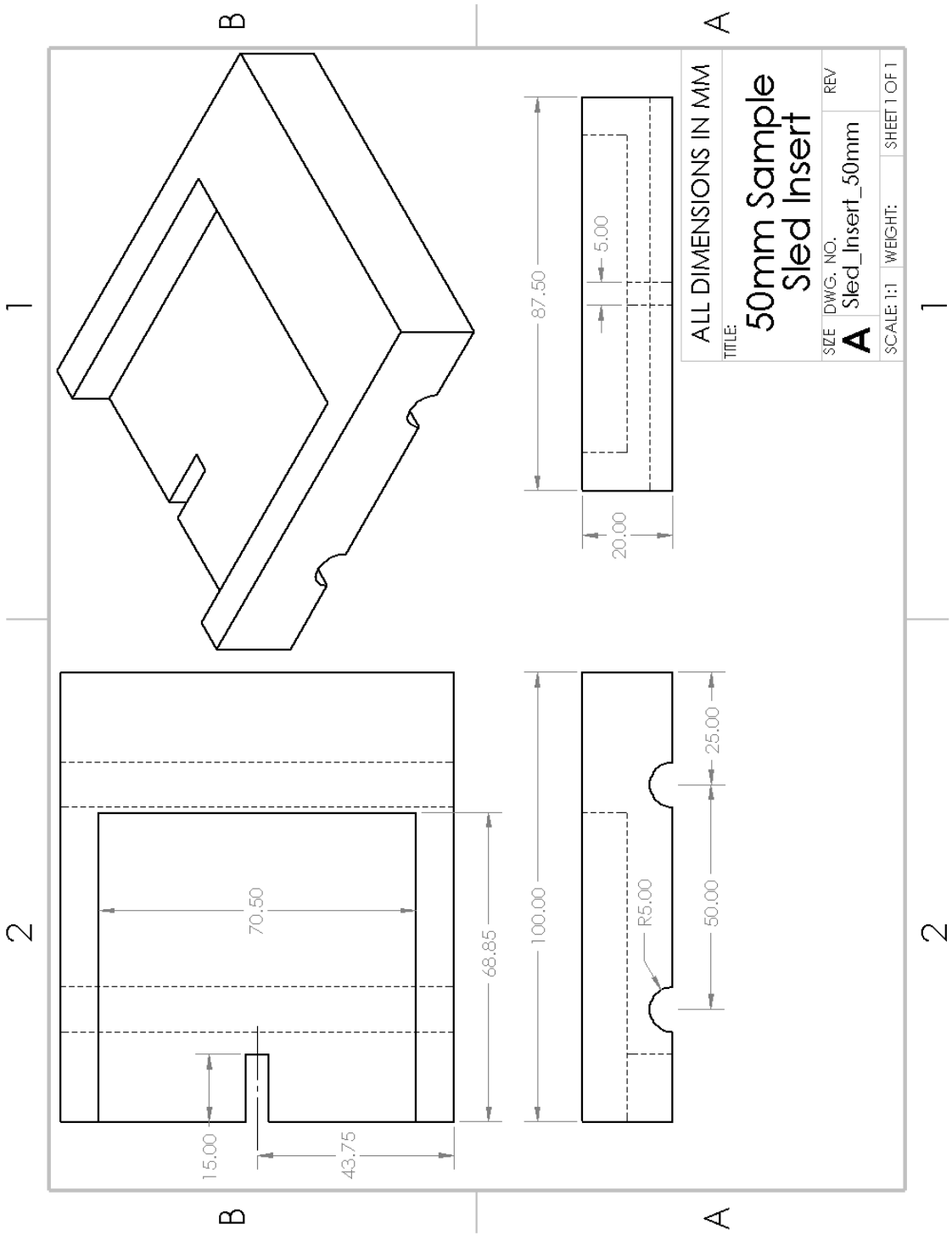


Figure A.2: SolidWorks drawing of the sled insert used to locate cuts made to prepare the 50 mm samples.

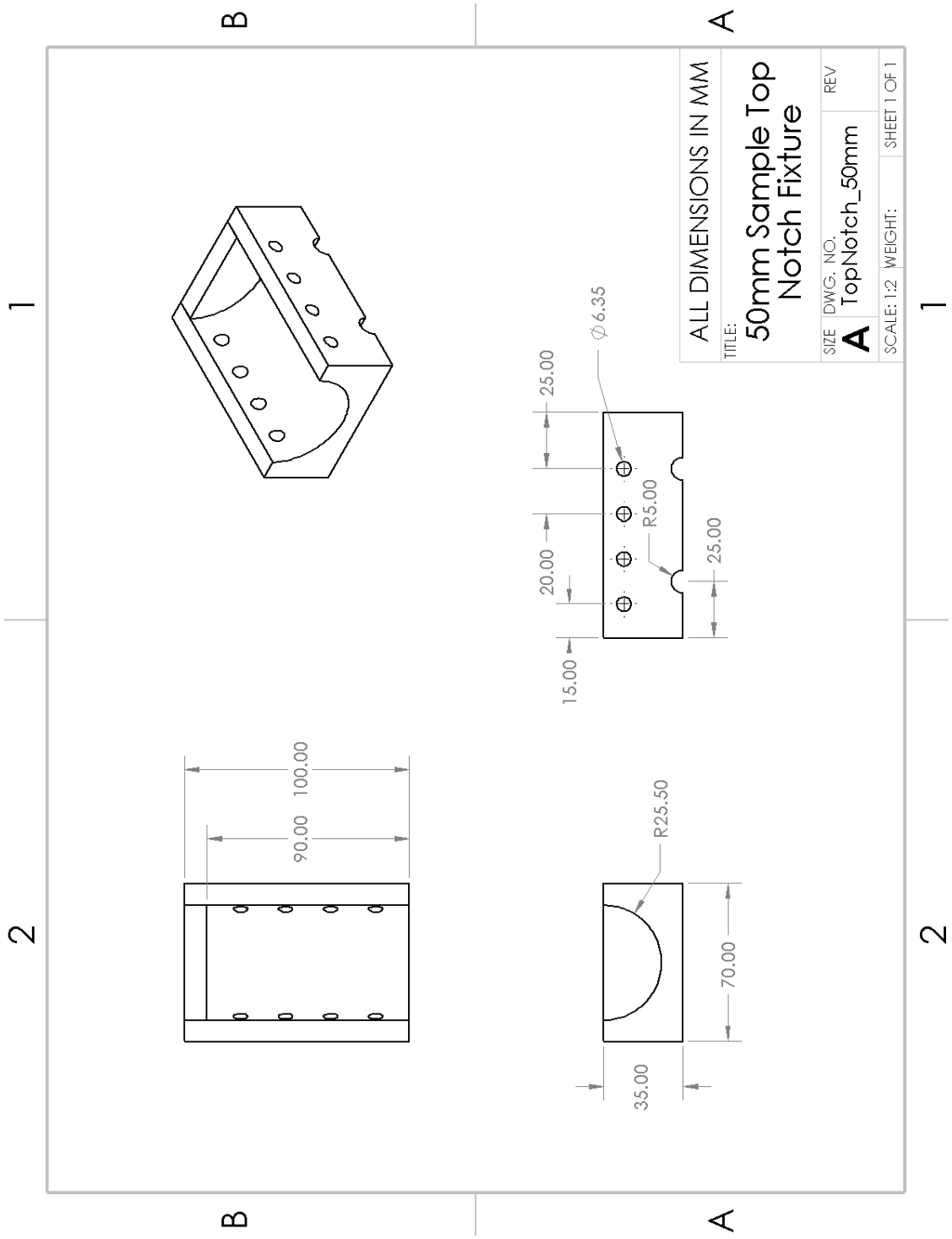


Figure A.3: SolidWorks drawing of the fixture used to cut the top notch in the 50 mm samples.

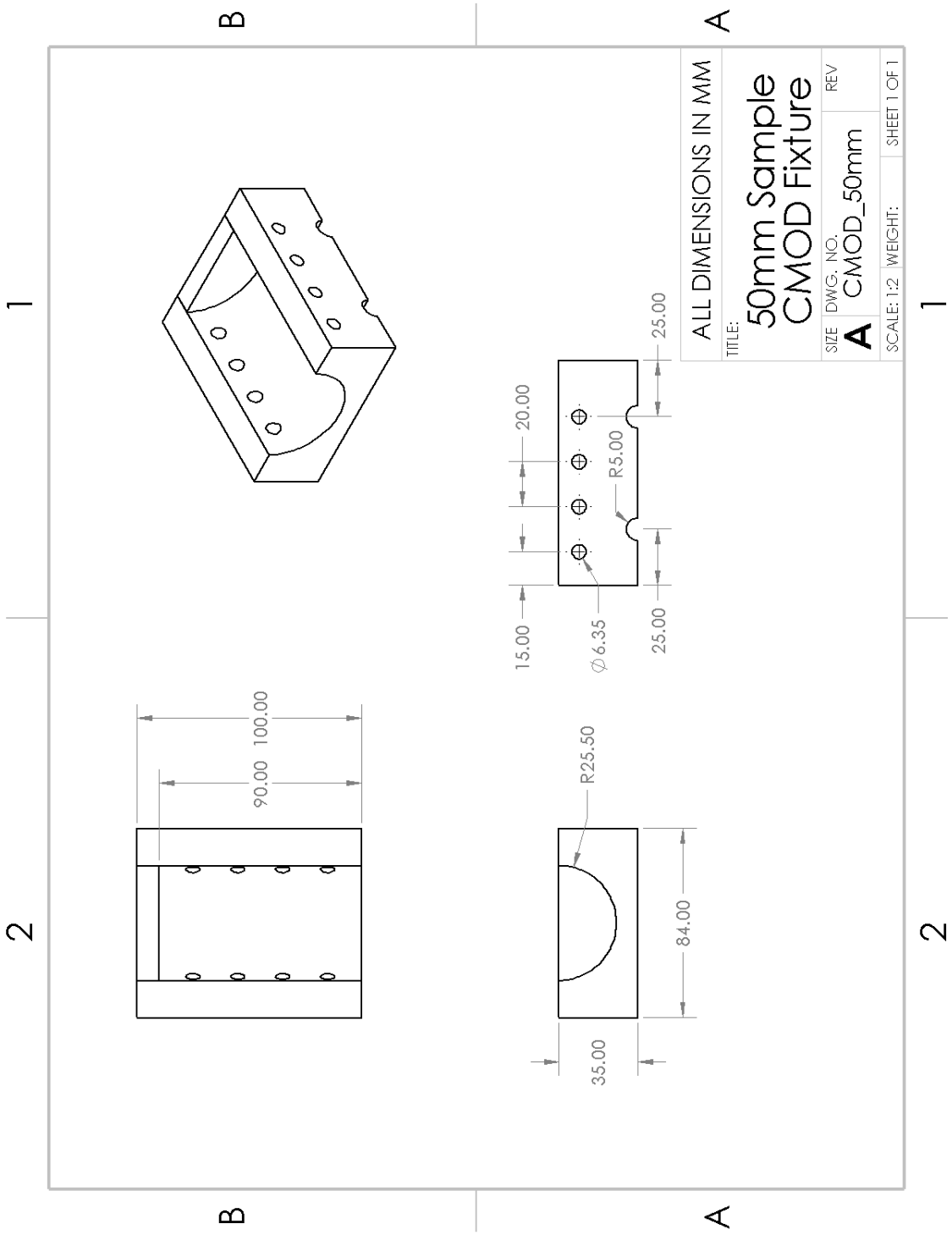


Figure A.4: SolidWorks drawing of the fixture used to cut the notch to locate the CMOD in the 50 mm samples.

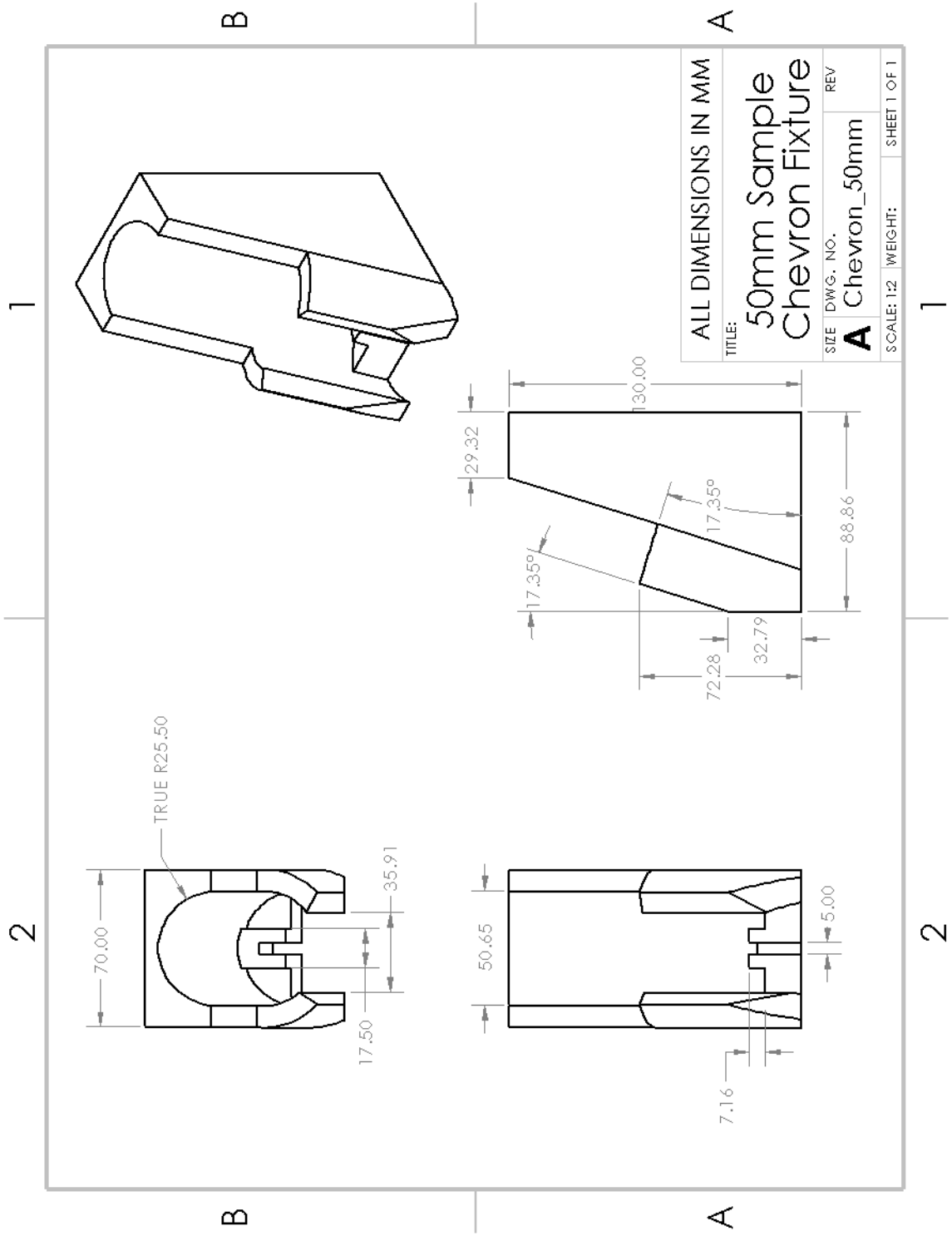


Figure A.5: SolidWorks drawing of the fixture used to cut the chevron in the 50 mm samples.

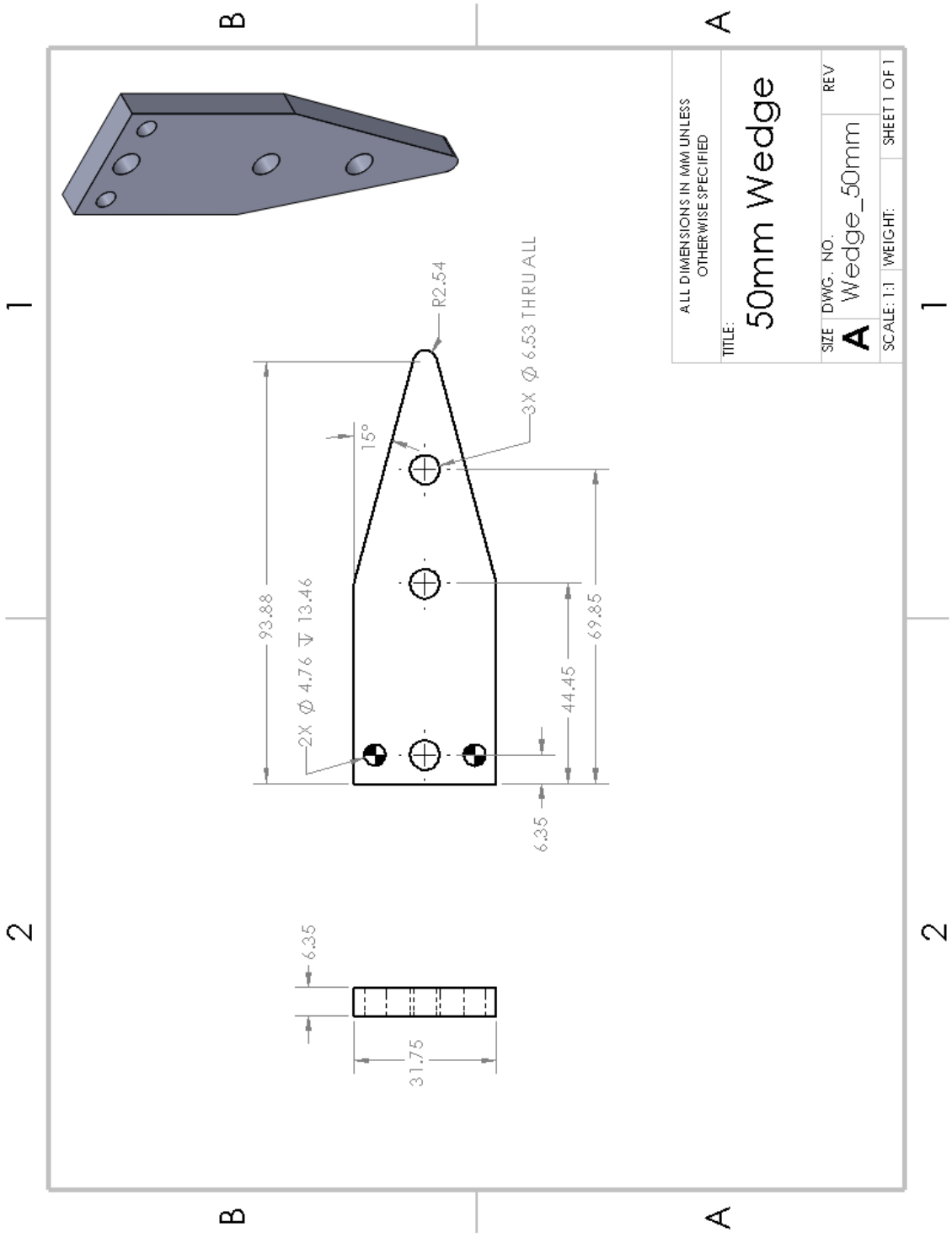


Figure A.6: SolidWorks drawing of the wedge plate that attaches to Drawings A.7 and A.8 to make up the test fixture used to break the 50 mm samples.

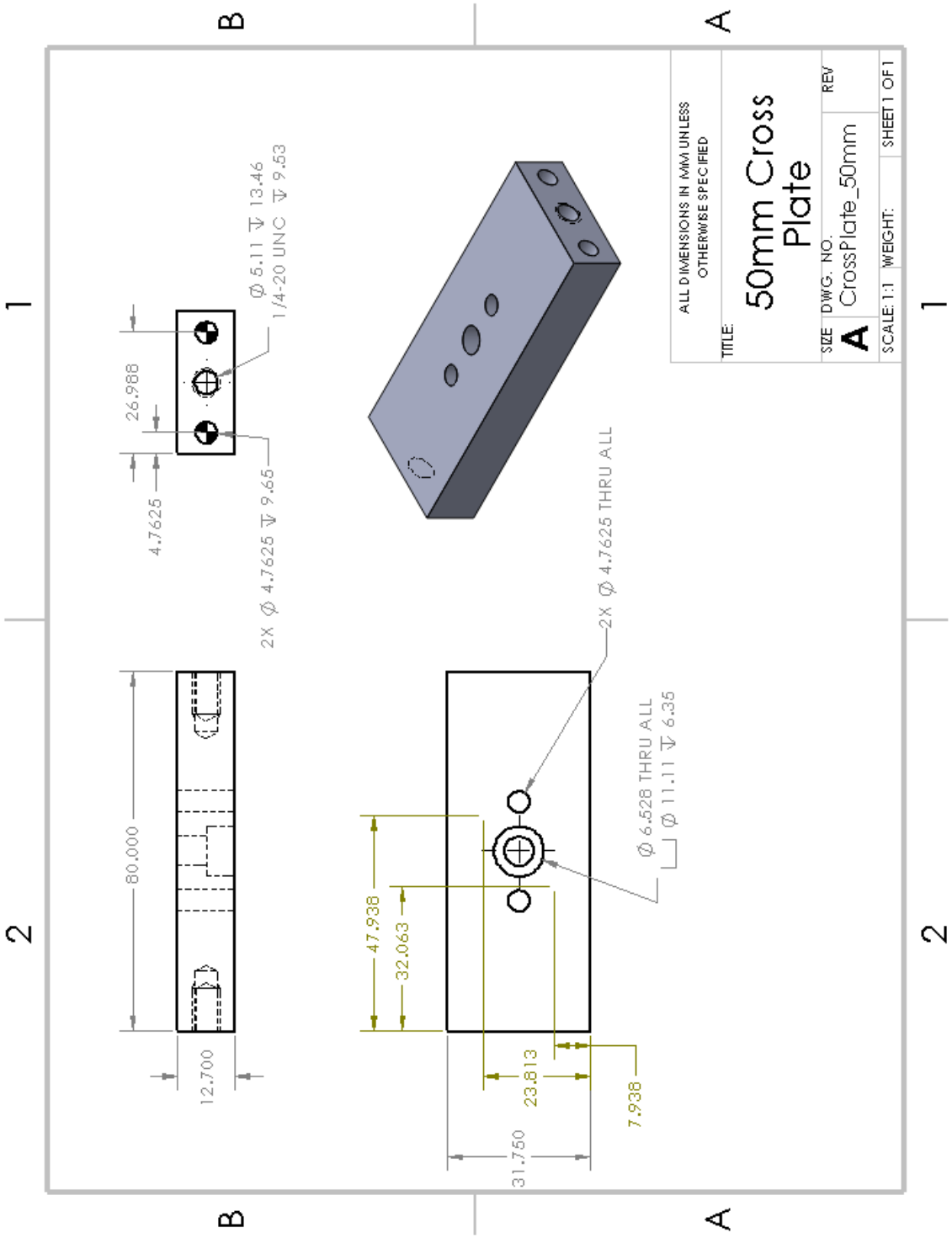


Figure A.7: SolidWorks drawing of the cross plate that attaches to Drawings A.8 and A.6 to make up the test fixture used to break the 50 mm samples.

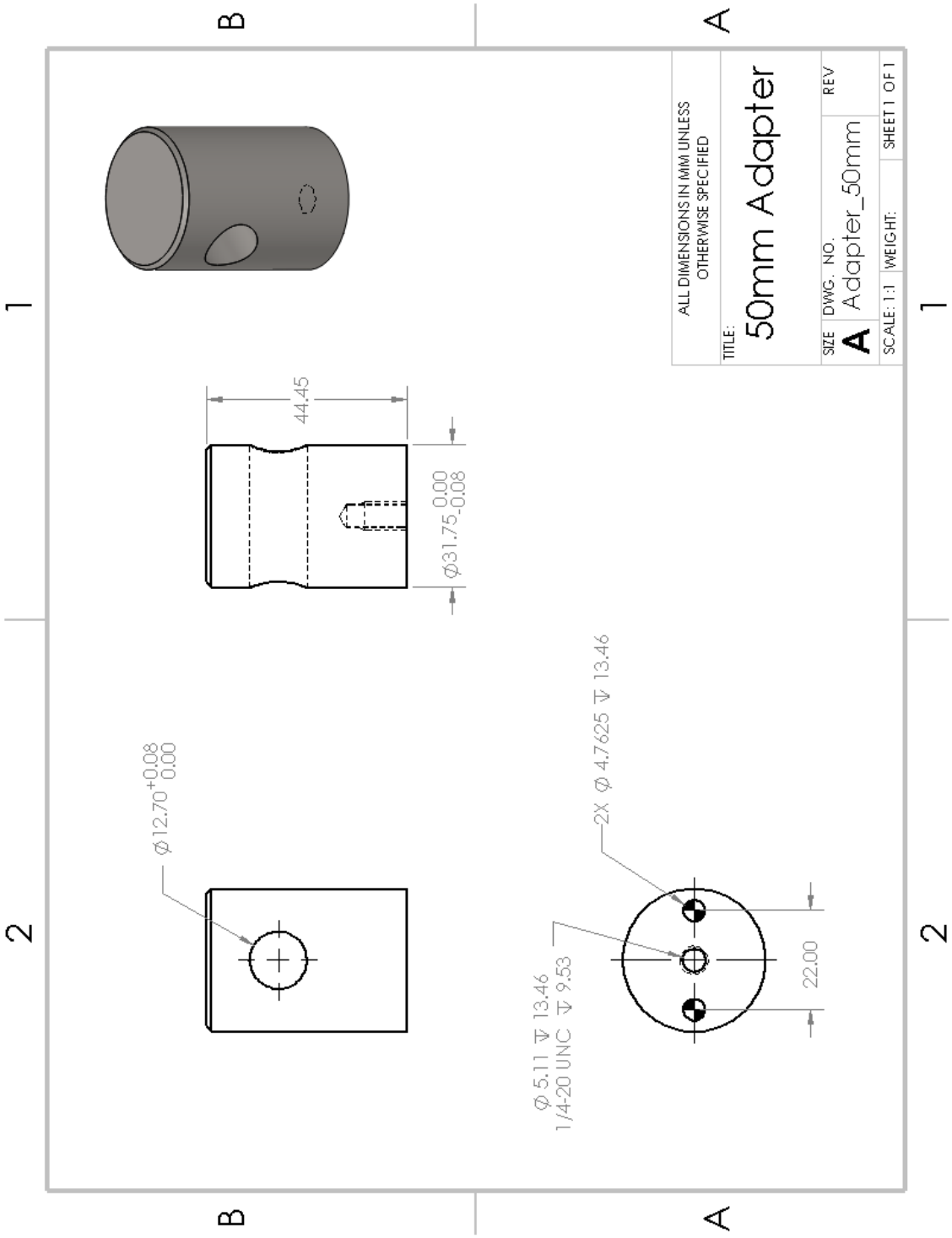


Figure A.8: SolidWorks drawing of the adapter that attaches to Drawings A.6 and A.7 to make up the test fixture used to break the 50 mm samples.

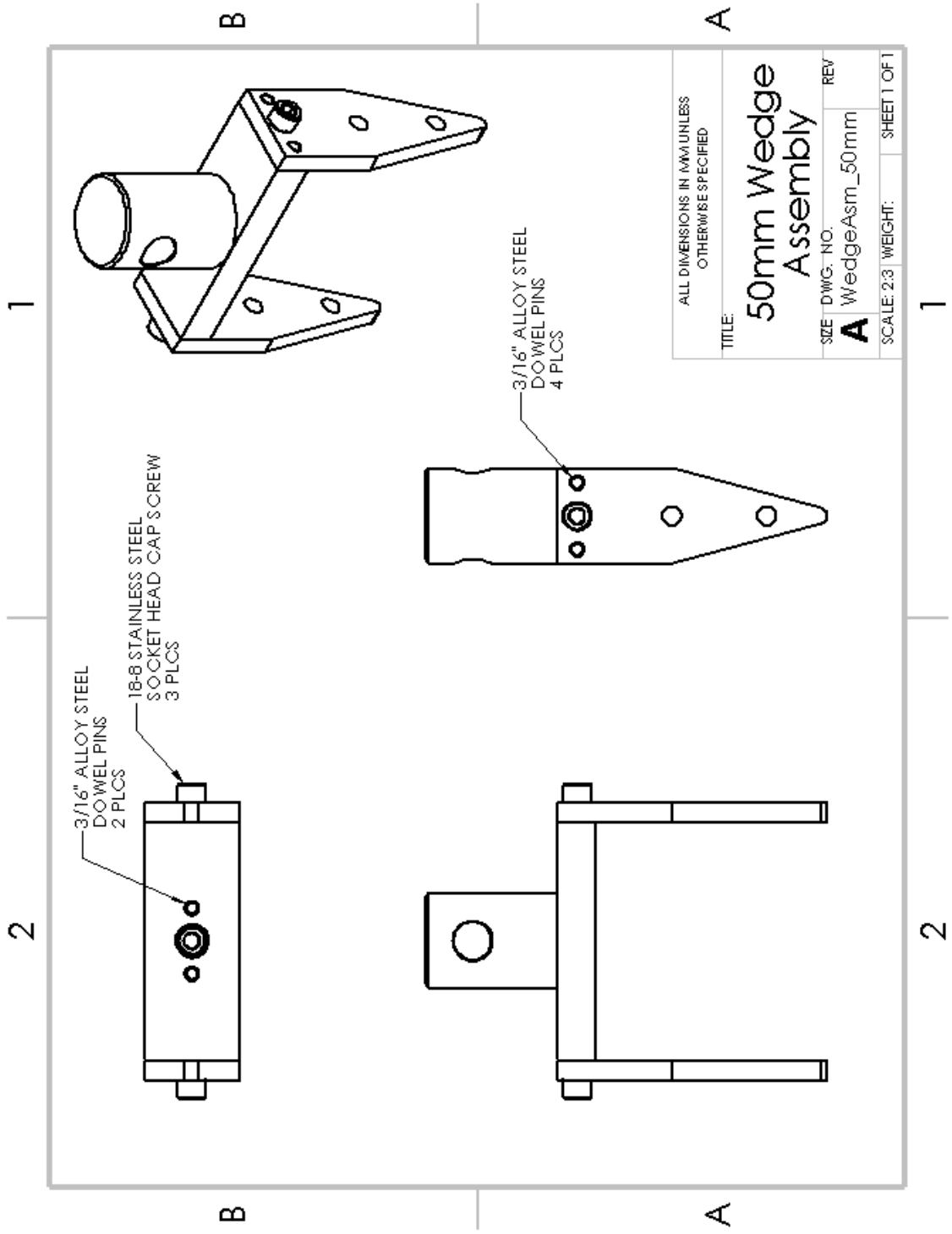


Figure A.9: SolidWorks drawing of the wedge assembly that attaches to the top crosshead of the MTS load frame to fracture the 50 mm samples.

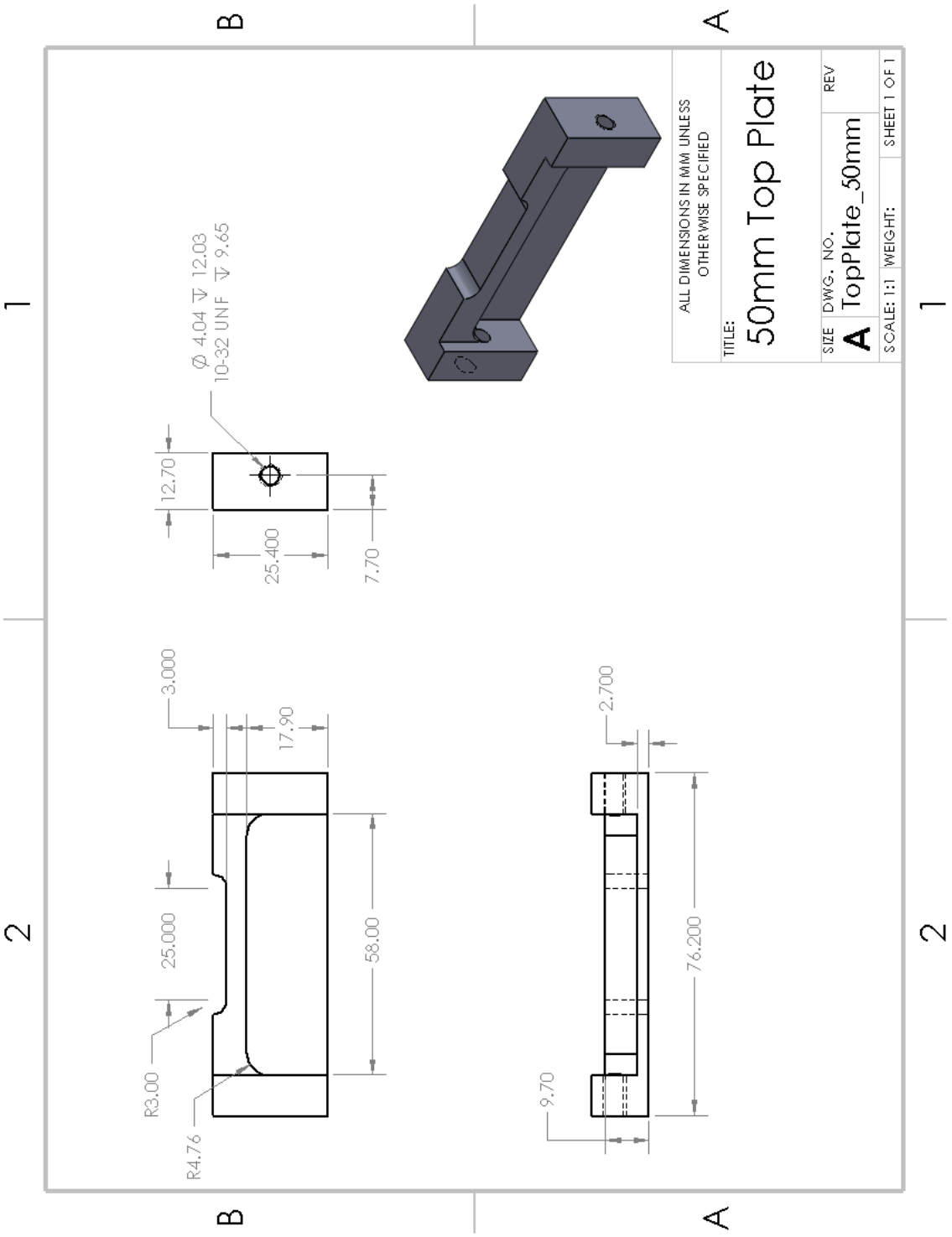


Figure A.10: SolidWorks drawing of the top plate that sits on top of the ice sample during fracture testing.

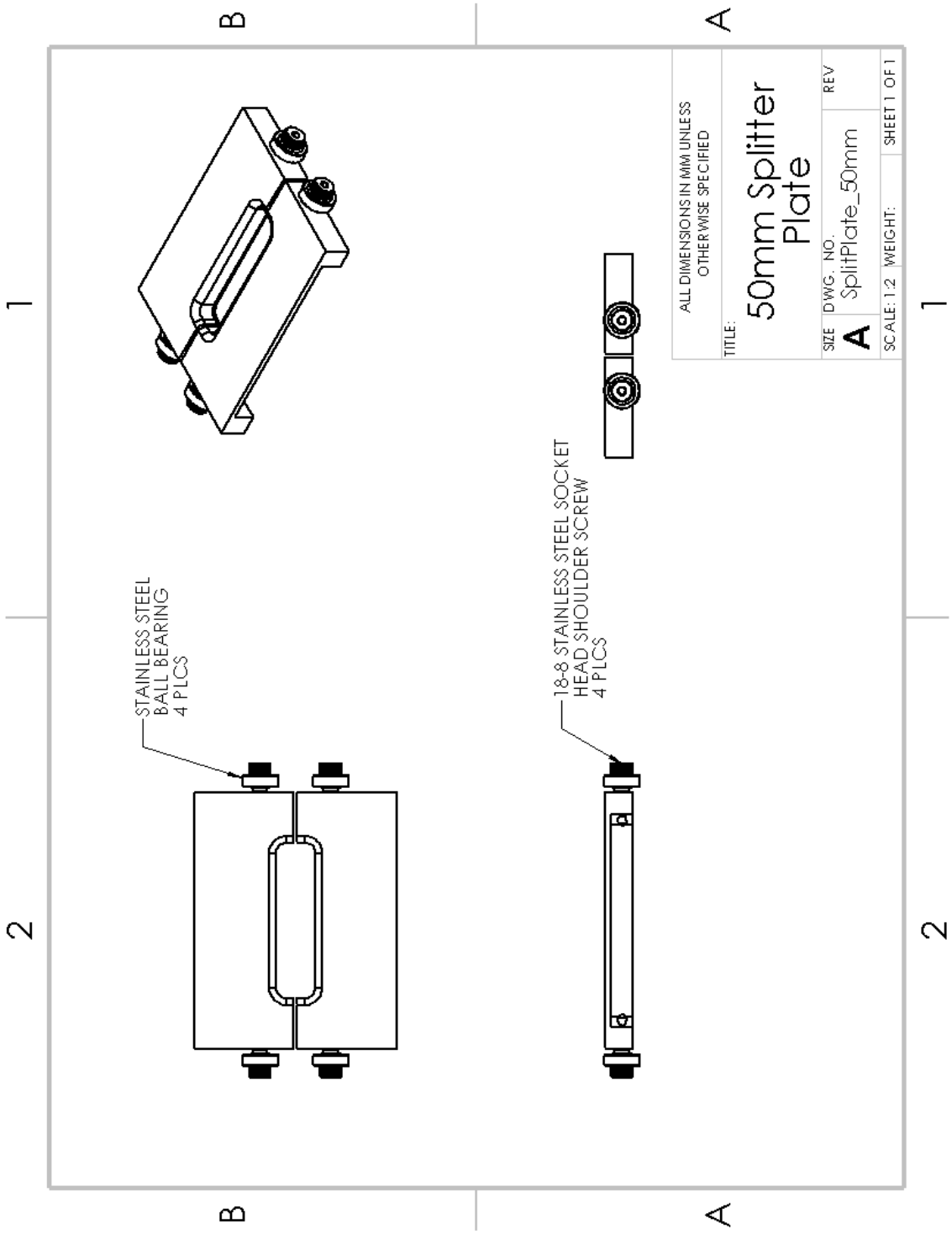


Figure A.11: SolidWorks drawing of two of the top plates with bearings and shoulder screws. These two parts sit on top of the ice samples and engage with the components in Drawing A.9 to break the 50 mm samples.

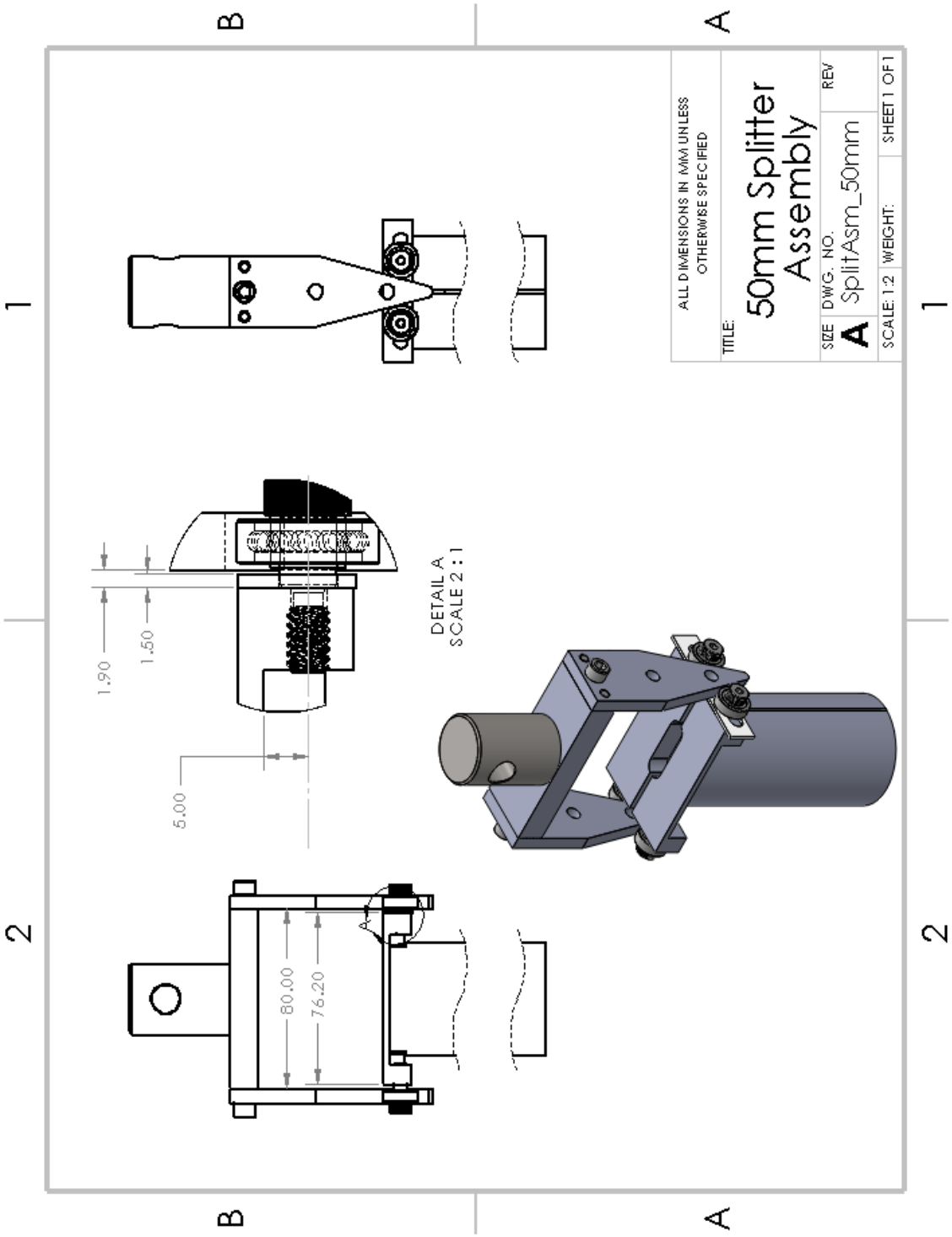


Figure A.12: SolidWorks drawing of Drawing A.9 engaging with Drawing A.11 used to fracture the 50 mm samples.

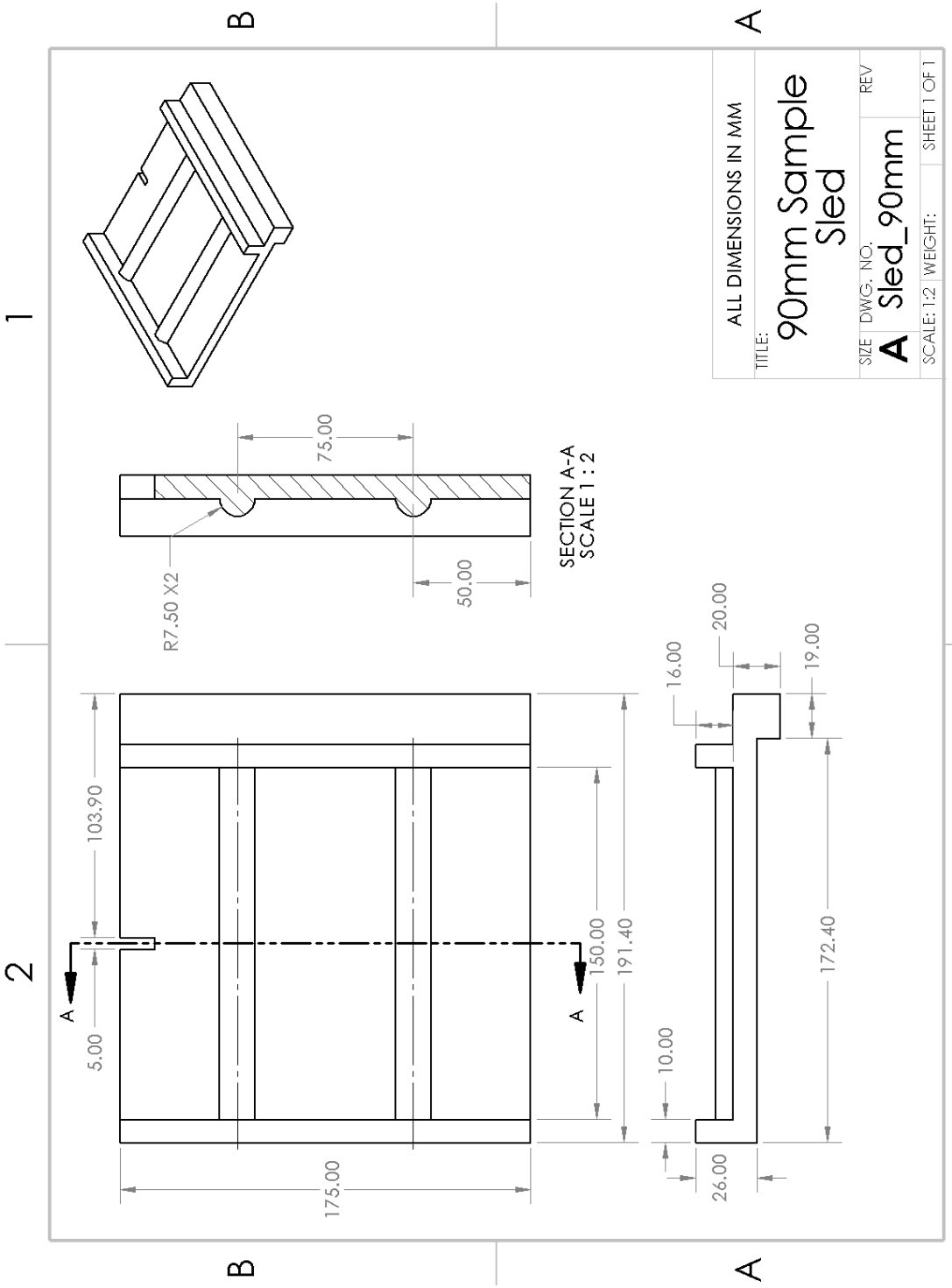


Figure A.13: SolidWorks drawing of the sled used to locate the 90 mm sample fixtures on the band saw table.

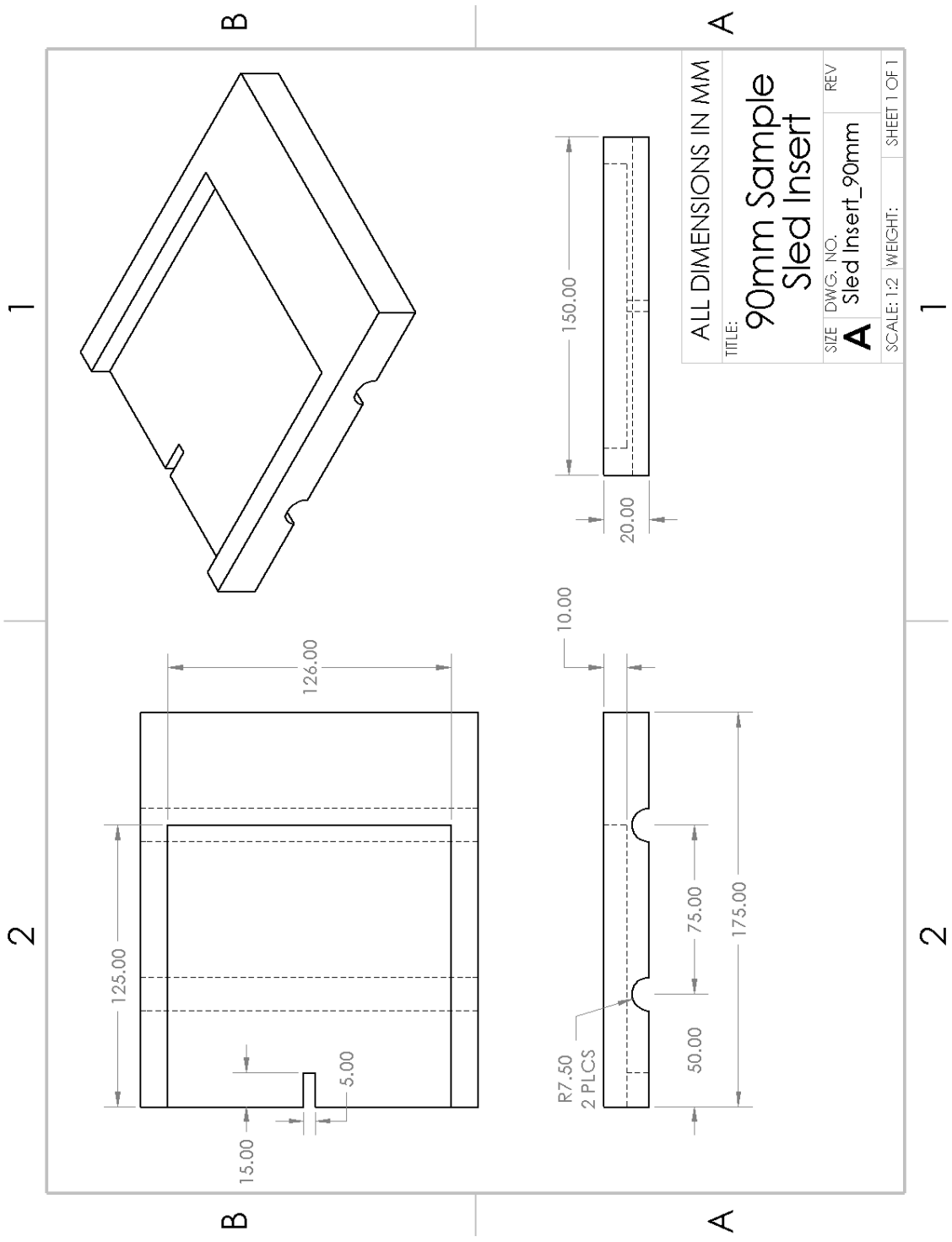


Figure A.14: SolidWorks drawing of the sled insert used to locate cuts made to prepare the 90 mm samples.

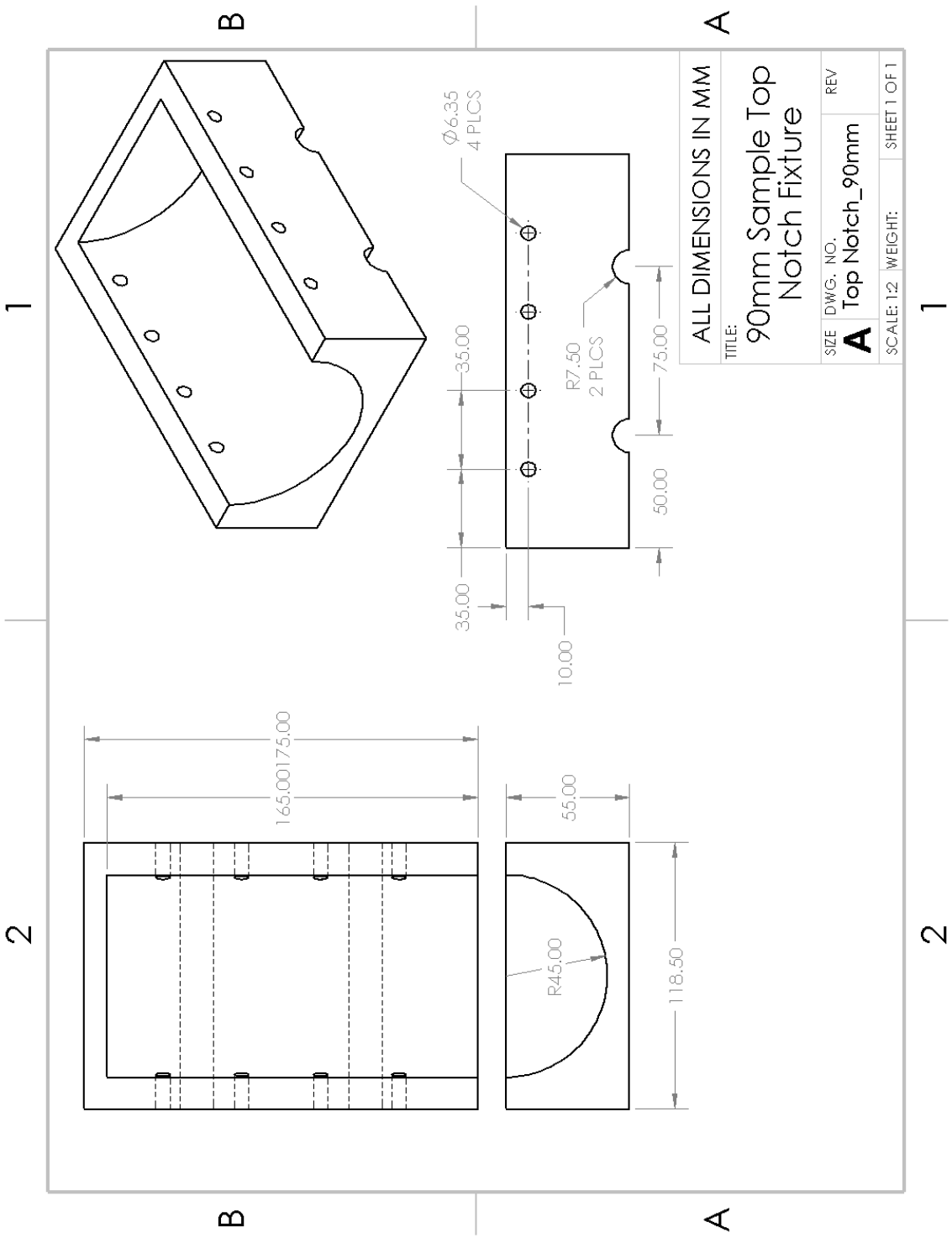


Figure A.15: SolidWorks drawing of the fixture used to cut the top notch in the 90 mm samples.

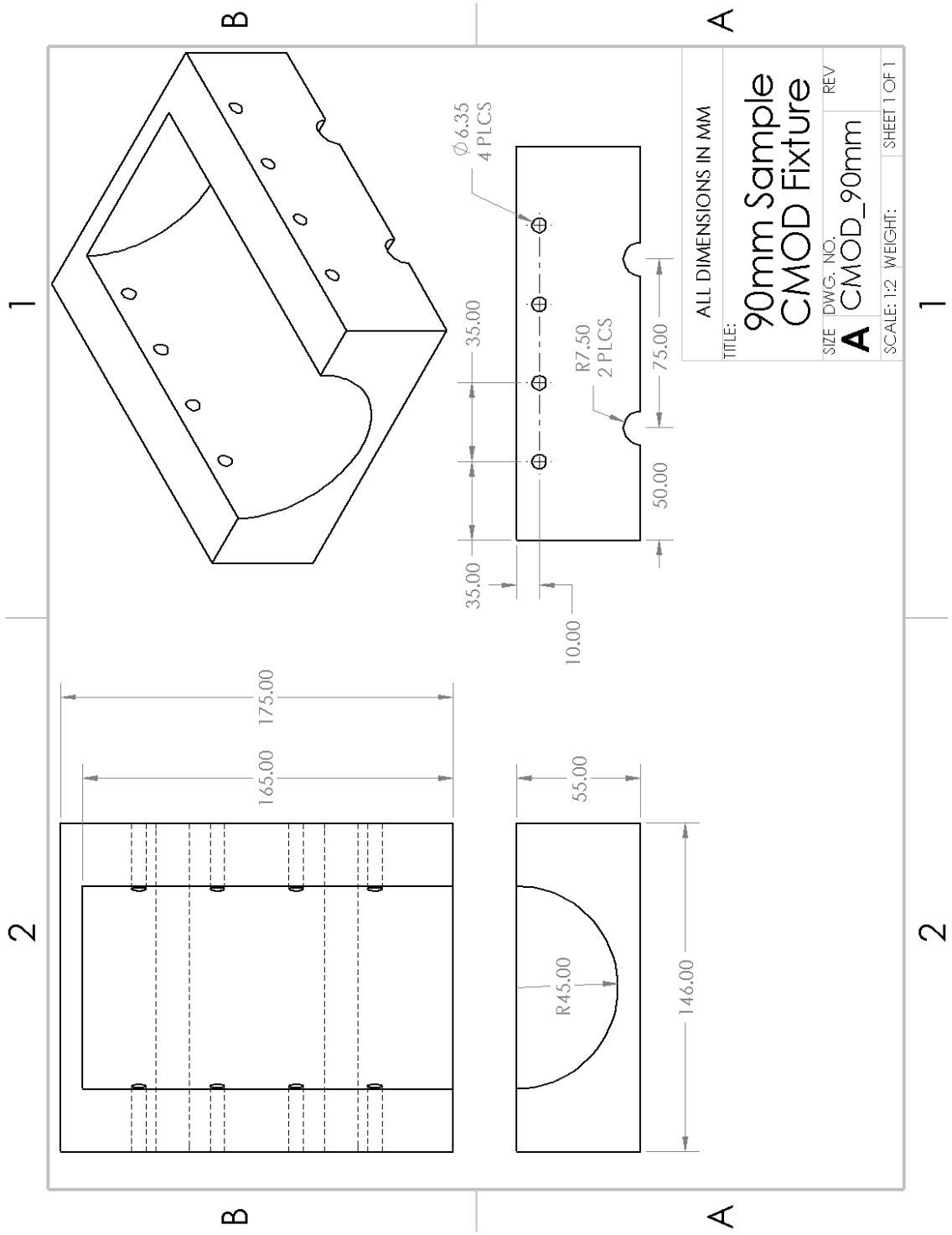


Figure A.16: SolidWorks drawing of the fixture used to cut the notch to locate the CMOD in the 90 mm samples.

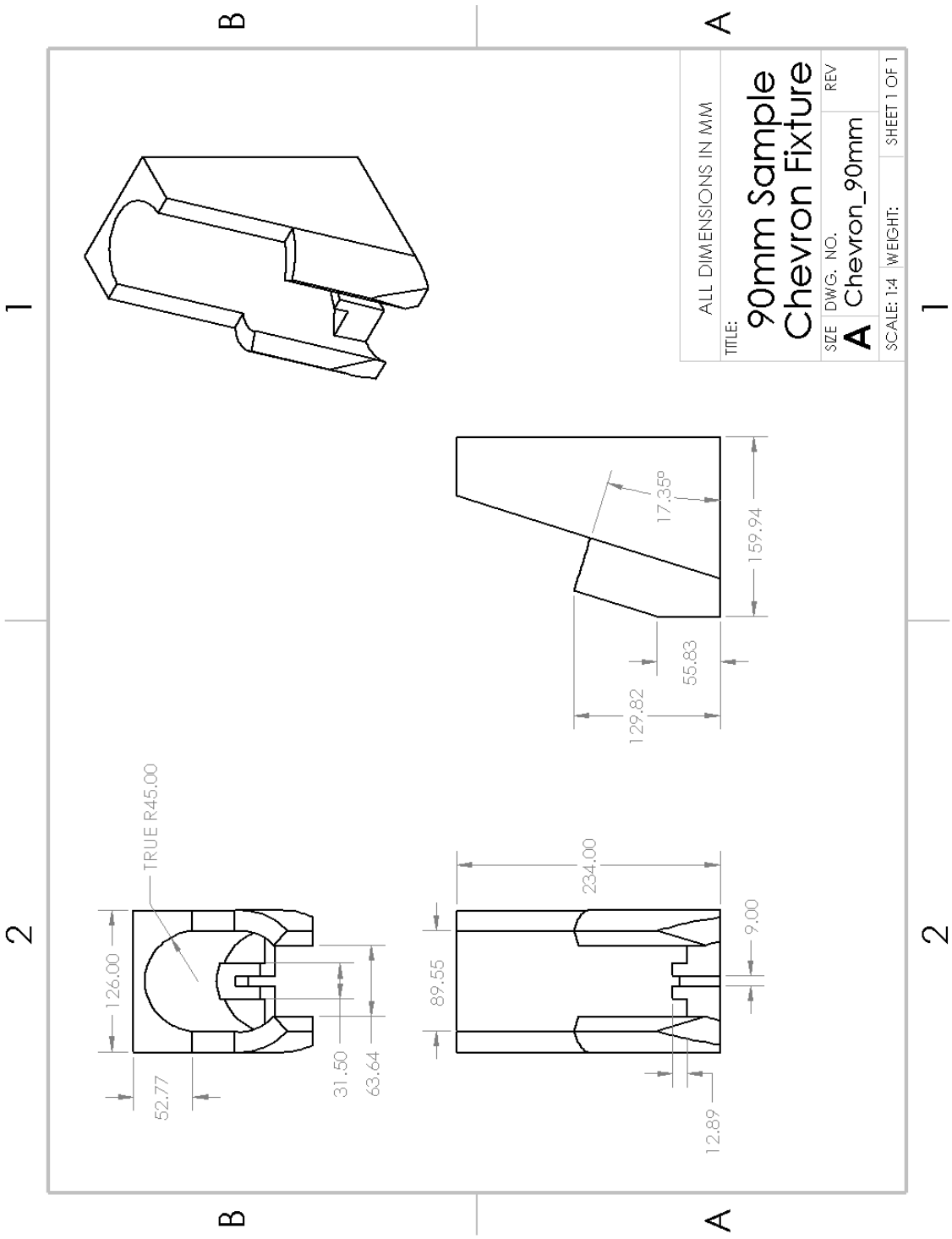


Figure A.17: SolidWorks drawing of the fixture used to cut the chevron in the 90 mm samples.

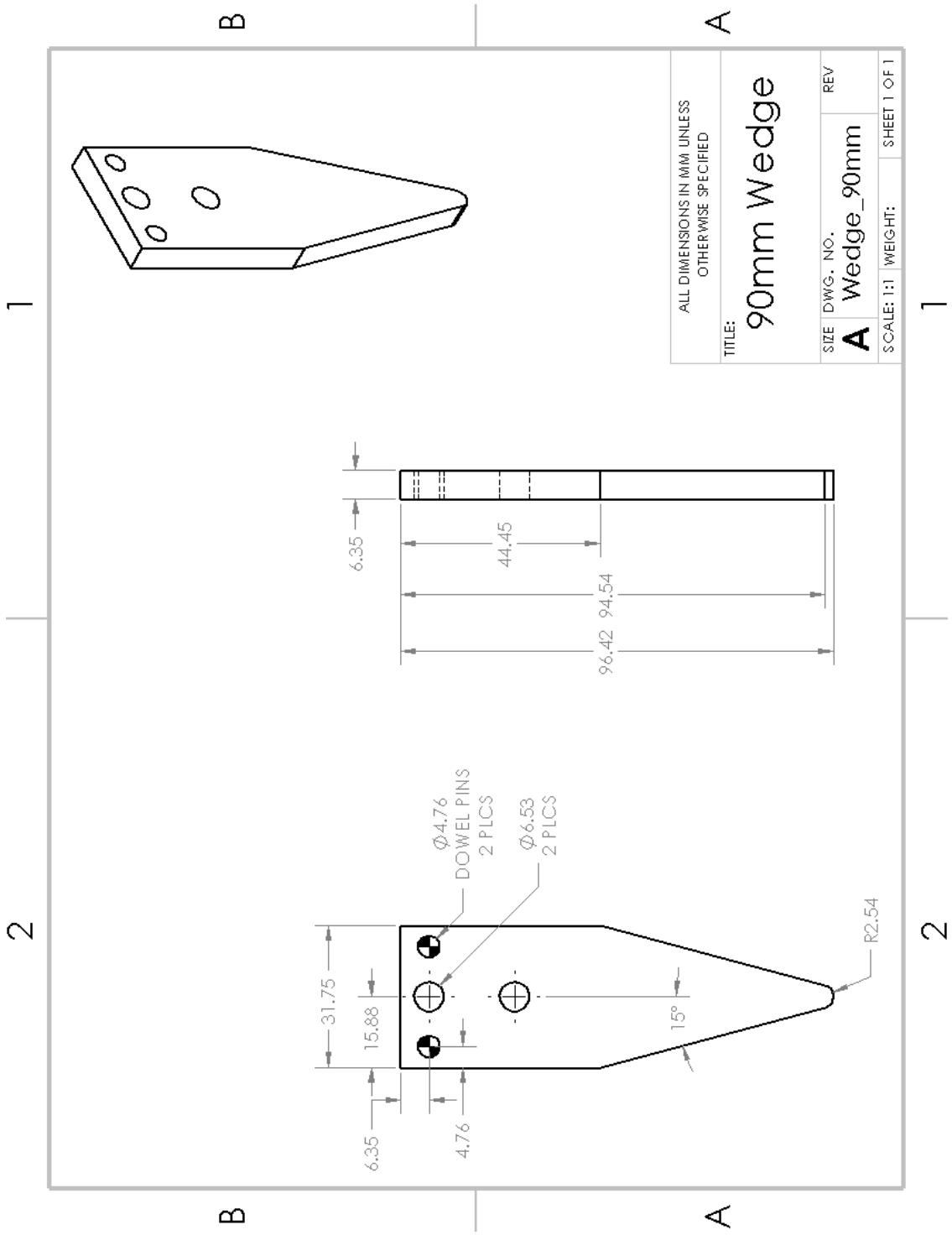


Figure A.18: SolidWorks drawing of the wedge plate that attaches to Drawings A.19 and A.20 to make up the test fixture used to break the 90 mm samples.

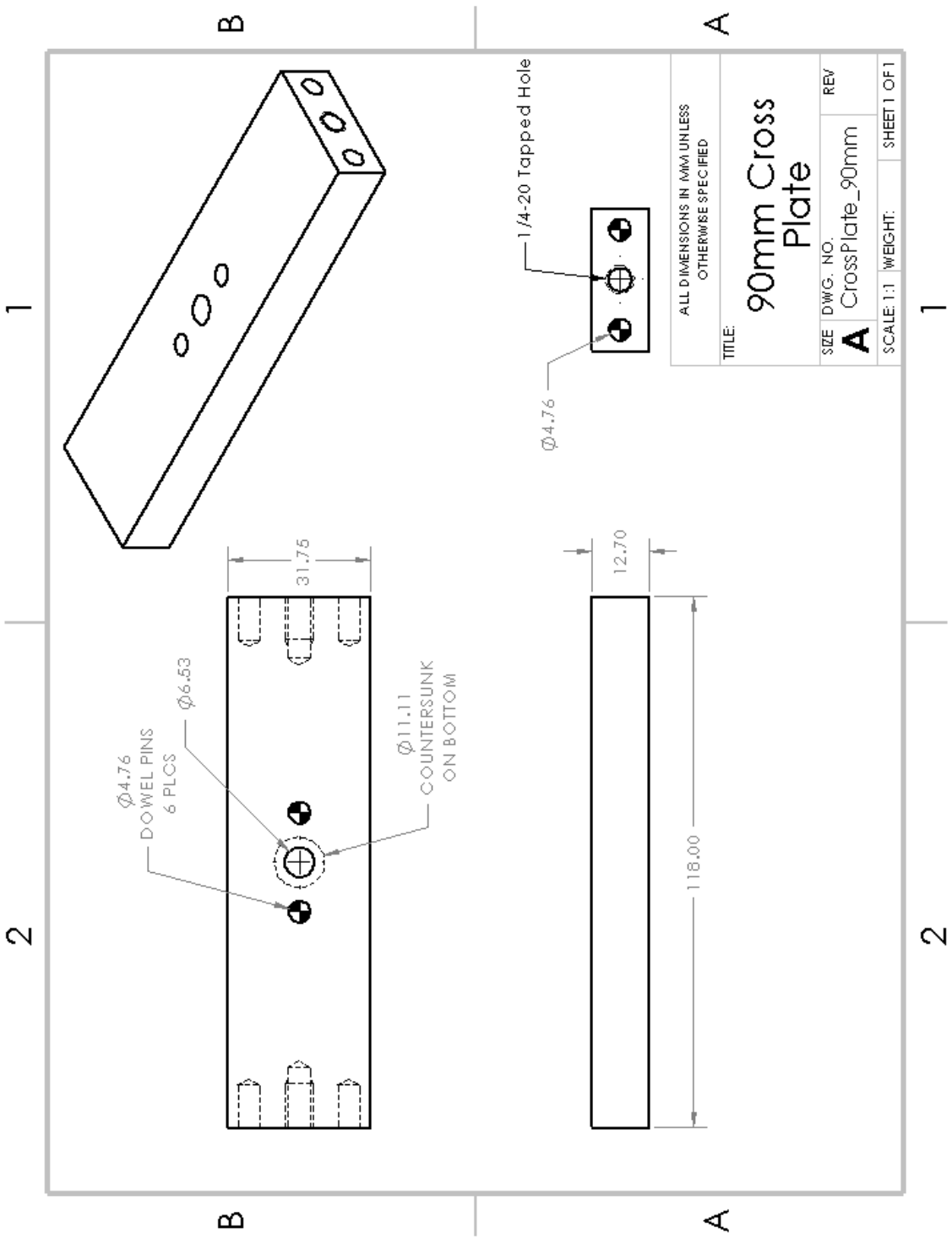


Figure A.19: SolidWorks drawing of the cross plate that attaches to Drawings A.18 and A.20 to make up the test fixture used to break the 90 mm samples.

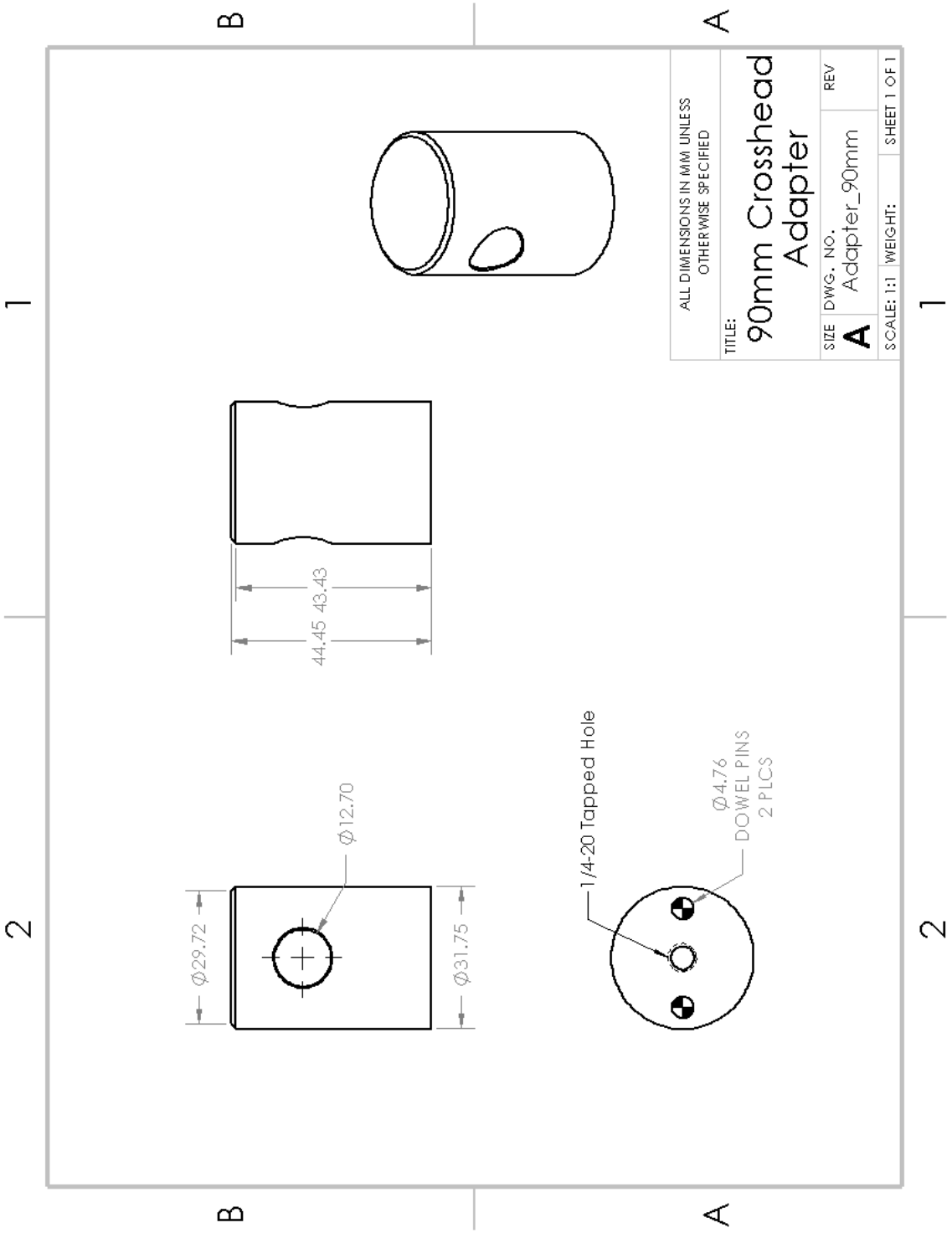


Figure A.20: SolidWorks drawing of the adapter that attaches to Drawings A.19 and A.18 to make up the test fixture used to break the 90 mm samples.

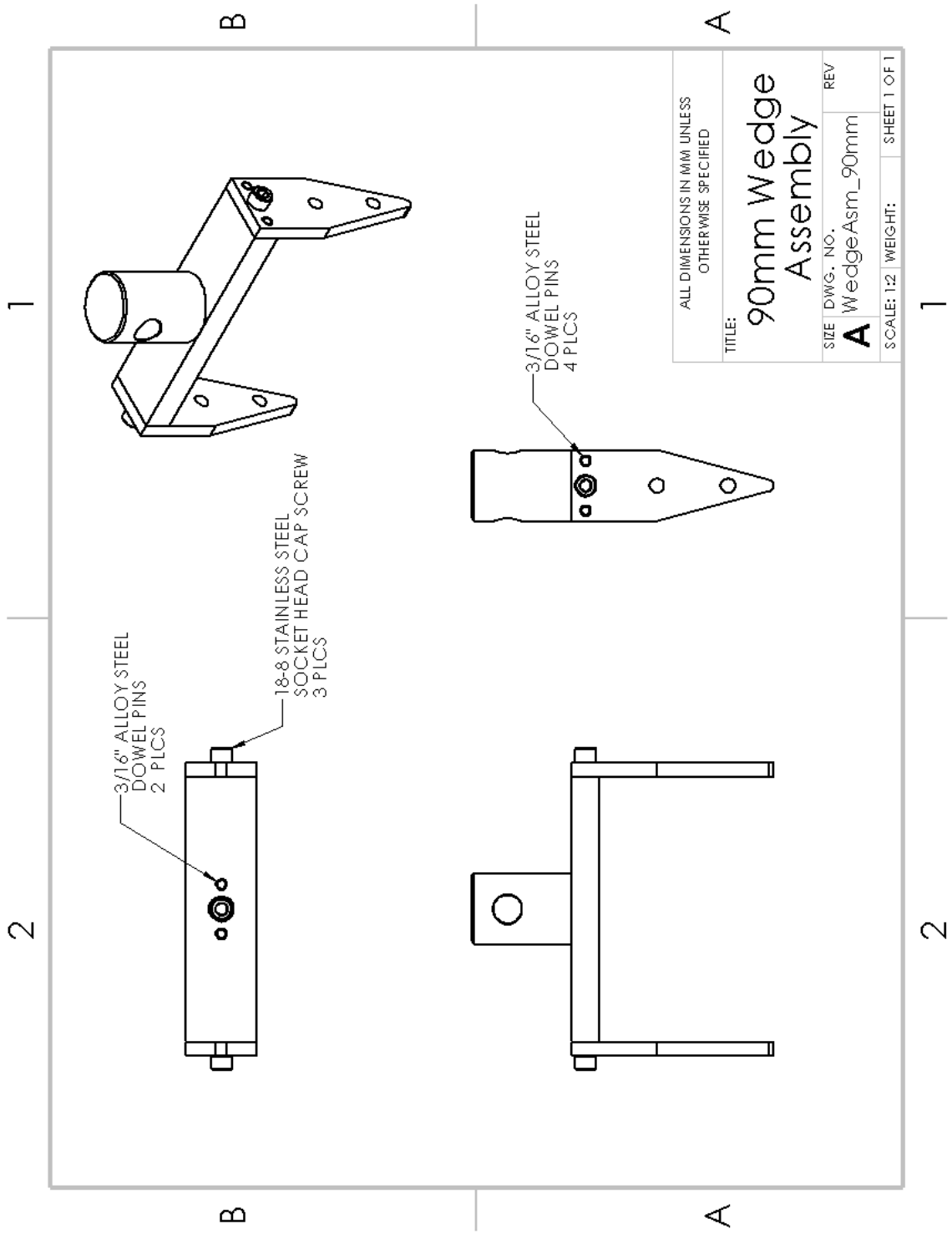


Figure A.21: SolidWorks drawing of the wedge assembly that attaches to the top crosshead of the MTS load frame to fracture the 90 mm samples.

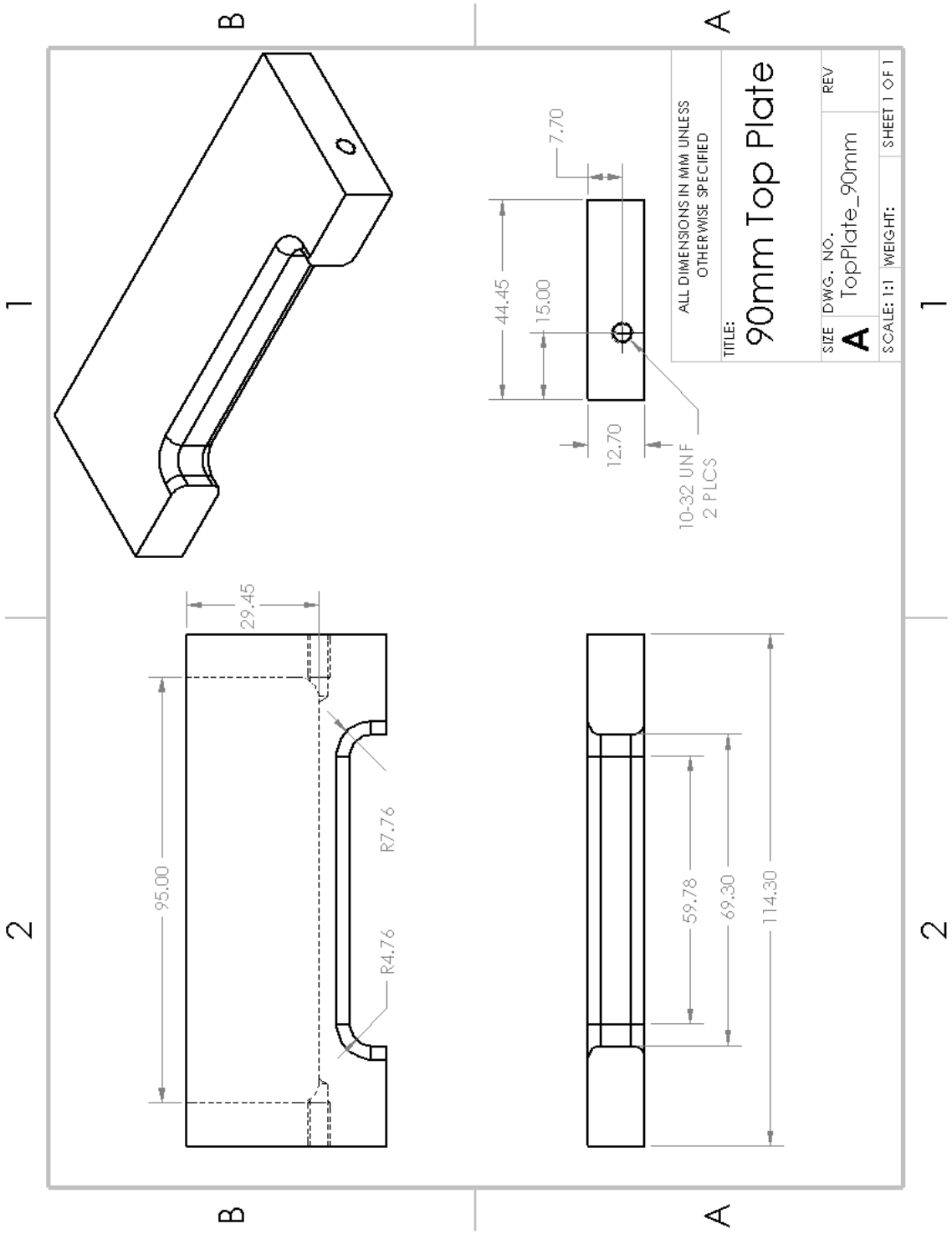


Figure A.22: SolidWorks drawing of the top plate that sits on top of the ice sample during fracture testing.

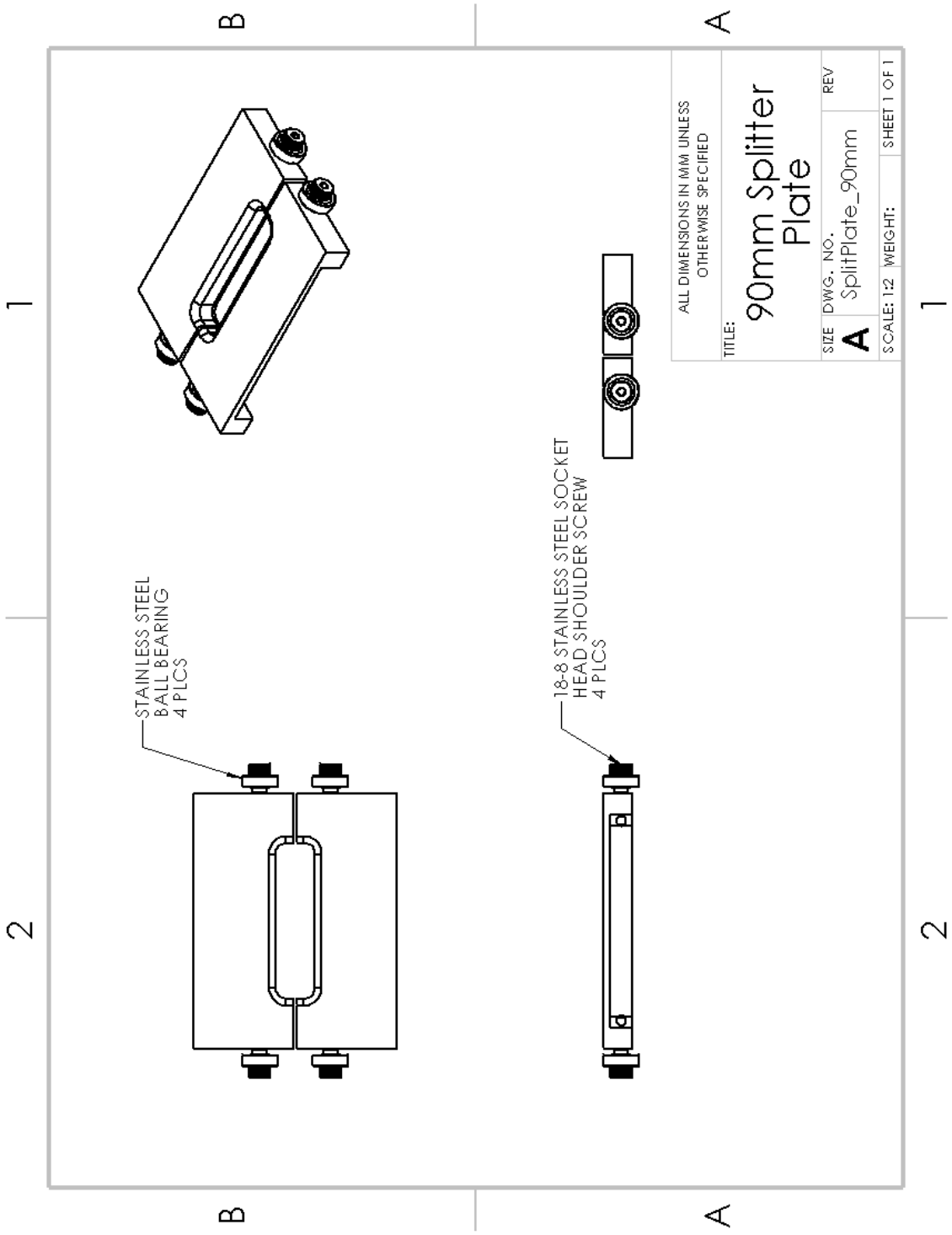


Figure A.23: SolidWorks drawing of two of the top plates with bearings and shoulder screws. These two parts sit on top of the ice samples and engage with the components in Drawing A.21 to break the 90 mm samples.

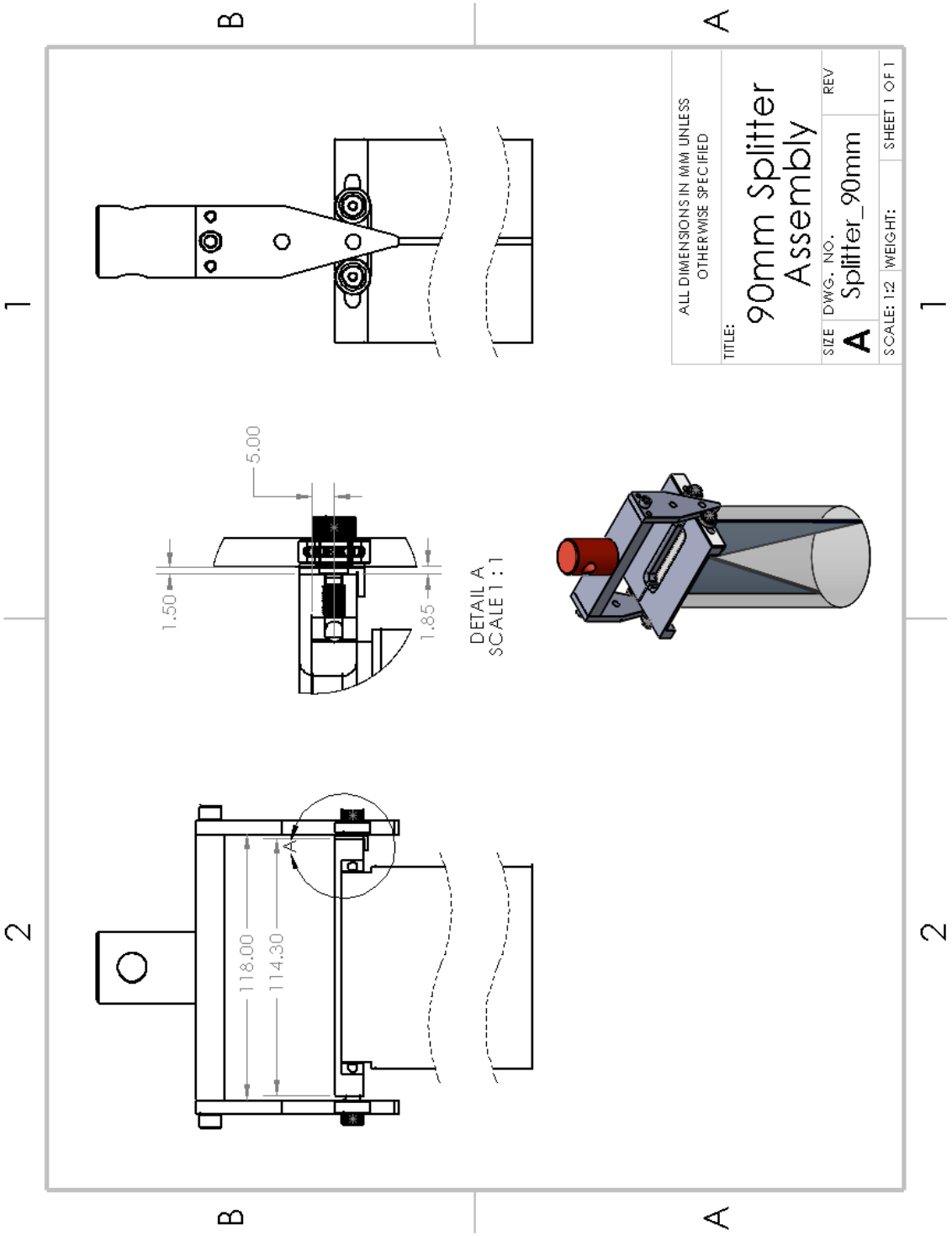


Figure A.24: SolidWorks drawing of Drawing A.21 engaging with Drawing A.23 used to fracture the 90 mm samples.

APPENDIX B

INSTRUCTIONS FOR SAMPLE CREATION AND MTS ENVIRONMENTAL CHAMBER

B.1 Sample Creation Setup

In order to make all polycrystalline ice samples, we used the setup shown in Figure B.2. Everything shown in Figure B.2 is located inside a temperature controlled freezer, set to 1°C, except the polyethylene glycol chiller. The tubing from the chiller runs inside the freezer, but the chiller itself sits outside at room temperature. All fittings used to connect various sections of hose together were brass compression plumbing fittings. These fittings have a cup/cone system at the interior that crimps a very tight seal without the need to braze the fittings to any piping. All of the vacuum tubing should be hard plastic tubing with a $\frac{1}{4}$ inch outer diameter. The plug at the top of the Buchner flask is a stopper outfitted with a ball valve. The inlet and outlet from the mold are quick-connect Swagelok fittings. These fittings have a tendency to freeze up once the sample is frozen and must be thawed before the next sample is created. A cross-section view of the mold with the end caps and quick-connect fittings can be seen in Figure B.1. The quick-connect fitting is threaded into the center hole of the end cap. This hole is tapered and gets tighter as the quick-connect fitting is threaded into the hole. One additional male quick-connect fitting is required with a short length of open tubing in order to test the water temperature coming out of the chilling bucket, prior to attaching the DI water hose to the bottom of the mold.

A drawing of the end caps of the mold is shown in Figure B.3. A Viton gasket is used between the Delrin end cap and the aluminum mold to prevent any air or water leaks. The gasket can be recessed into the cap or can be attached directly to the cap. We used a $\frac{1}{16}$ inch thick Viton gasket, but a thicker gasket could be used as well.

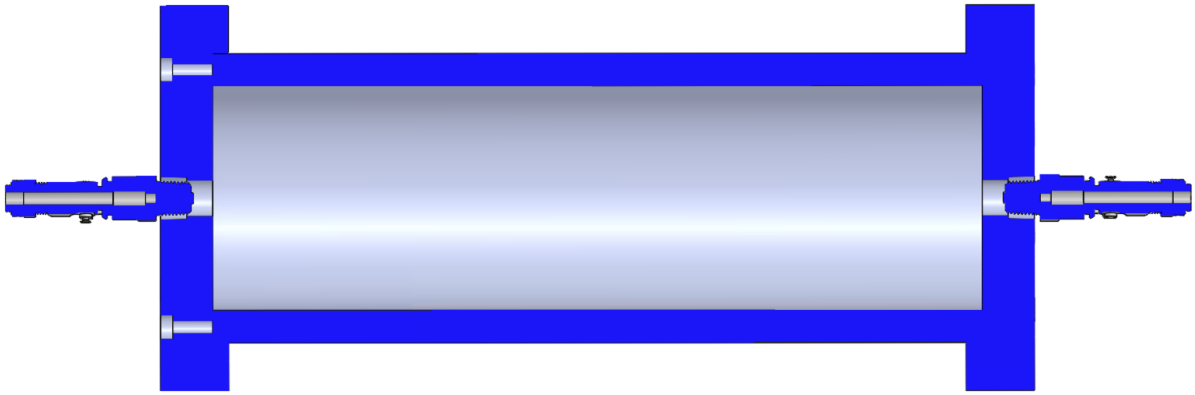


Figure B.1: A section view of the mold with both end caps and quick-connect fittings attached.

B.2 Procedure for Sample Creation

- Turn on the glycol chiller and set the temperature to -4.5°C. Let the glycol temperature reach the set point before proceeding.

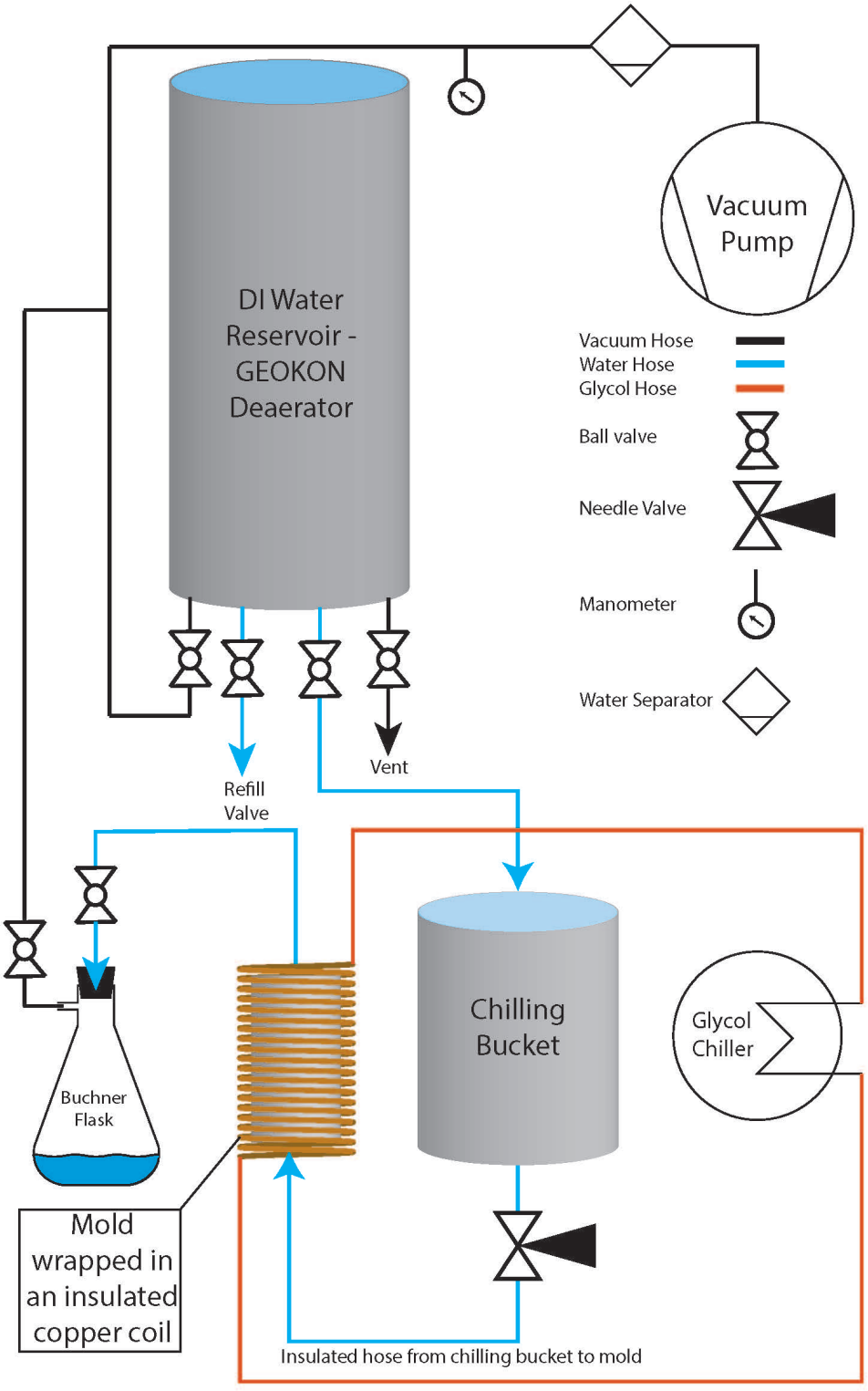


Figure B.2: Full diagram for the setup used to make all polycrystalline ice samples.

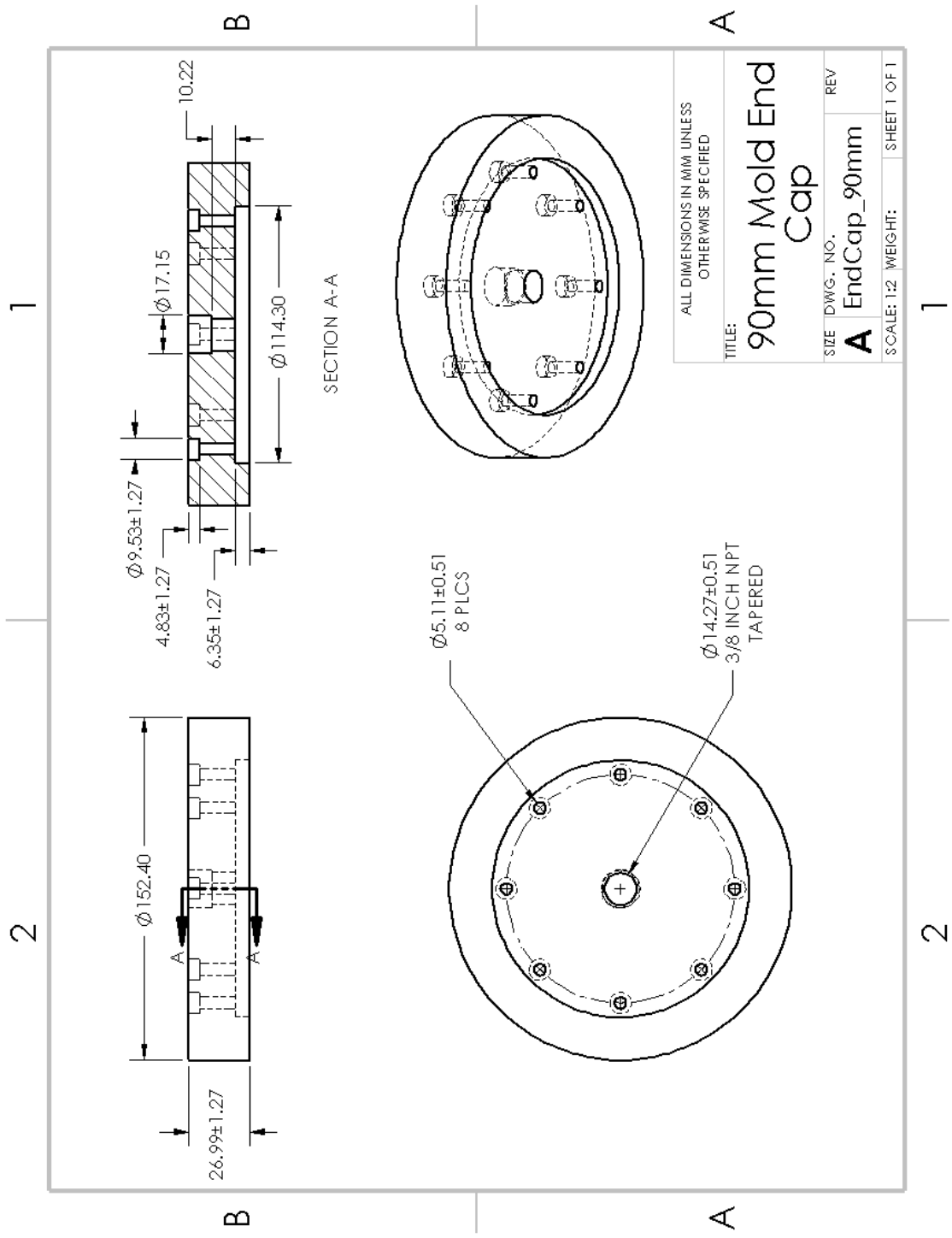


Figure B.3: Drawing of the Delrin end caps used for the sample creation process.

  - Setting the temperature this low drives the correct freezing rate.
  - For the first few samples, this temperature should be adjusted in order to achieve the correct freezing rate.

- Make sure the aluminum mold is colder than 0°C, with just one end cap attached.
- Fill the mold with sieved seed grains of ice. Pack down the grains periodically to eliminate large voids.
- Bring the mold, full of seed grains, into the freezer with the remaining equipment.
- Slide the glycol-filled copper coil onto the mold and attach the top end cap.
- Attach the top hose to the mold via the quick-connect fitting that runs to the Buchner flask.
- Open the valve from the Buchner flask to the vacuum pump and allow the mold to sit under vacuum for at least one hour.
- Prior to filling the mold with water, the DI water must be de-aerated.
  - The de-aerator used in this study was manufactured by GEOKON consisting of a reservoir with two long stainless steel tubes on the inside that were used for the vent and vacuum lines shown in Figure B.2 as well as two other ports used to fill and drain the de-aerator.
    * The filling port is attached to a longer section of tubing that is then attached to a container full of DI water.
    * The drain port is attached the hose that leads into the chilling bucket and then into the mold.
- Plug in the de-aerator and open the valve running to the vacuum pump to pull dissolved gasses from the DI water.
- When the water is de-aerated to your satisfaction, at least 15 minutes, turn off the de-aerator, but leave the valve to the vacuum open.
- When you are ready to begin creating your sample, close the valve from the de-aerator to the vacuum pump
- Open the vent valve on the de-aerator and allow the pressure inside the de-aerator to slowly reach atmospheric pressure.
- Open the drain valve on the de-aerator to allow the water to flow through the chilling bucket.
- Open the needle valve and attach the male quick-connect with the short, open section of tubing to purge the water inside the tubing that was not de-aerated.
  - At this point, check the temperature of the water exiting the chilling bucket and make sure it is below 2.5°C.

- Once the water has been purged from the tubing inside the chilling bucket, reduce the flow out of the chilling bucket with the needle valve until the water is dripping out at 1 drop every second.
- Taking care not to adjust the needle valve, remove the male quick-connect and short section of tubing and connect the female end of the quick-connect to the male quick-connect on the mold.
- Allow the mold to fill slowly, the mold will be full when water begins to fill the Buchner flask
- Let the Buchner flask accumulate at least 100 mls of water and ensure the tube leading from the mold to the Buchner flask has no air in it.
- Slowly close the ball valve at the top of the Buchner flask, then slowly close the ball valve from the Buchner flask to the vacuum pump.
  - At this point you should turn off the vacuum pump.
- Release the pressure inside the Buchner flask by removing the stopper. Reinstall the stopper and make sure there is a tight seal.
- Wait 5 - 10 minutes before re-opening the ball valve at the top of the Buchner flask.
- As you are slowly opening the ball valve at the top of the Buchner flask, make sure the water does NOT run backwards into the mold. If the water starts to run backwards, shut the ball valve immediately and wait a few more minutes for the pressure to equalize throughout the system.
- Once the ball valve at the top of the Buchner flask is open, adjust the needle valve until the flow into the Buchner flask is approximately 1 drop every 5 seconds.
- The system is now ready to freeze, leave the setup as is and return to check the sample after 2.5 hours for the 50 mm samples and 5 hours for the 90 mm samples.
- After the sample is frozen, increase the temperature of the glycol chiller, remove both end caps and wait for the sample to come loose from the mold.
- Once the sample is out of the mold, place it upright inside a cooler full of cold packs and bring to the freezer so the sample can equilibrate for 24 hours.

B.3 Refilling the De-aerator

- Attach the filling port hose to a container full of DI water.
- Open the filling port ball valve and the ball valve to the vacuum pump.
- Make sure the drain and vent ports are closed.
- Fill the de-aerator to the desired level, at least 10 inches from the top of the tank.
- Close the filling port valve and the vacuum valve, shut off the vacuum pump.

B.4 Operating the MTS Load Frame and Environmental Chamber

- Open TestSuite Elite on the computer connected to the MTS load frame.
- Turn on the MTS load frame.
- Make sure the door to the environmental chamber is closed and securely latch, it will not cool if the door is open.
- Turn on the Eurotherm 2408/2404 Process Controller, and adjust the set point to the desired temperature.
- Make sure the controller is set to Op2. This is the setting that tells the controller it needs to cool the environmental chamber.
- Open the valve to the liquid nitrogen tank until you can hear liquid nitrogen flowing through the hose.
- Let the system sit for a few minutes and make sure the temperature is dropping inside the environmental chamber.